Studies of $\Upsilon(1S)$ bottomonium state production at the Tevatron Collider Experiment DØ

Jundong Huang

Submitted to the faculty of the Graduate School
in partial fulfillment of the requirements
for the degree
Doctor of Philosophy
in the Department of Physics,
Indiana University

November, 2004

Accepted by the Graduate Faculty, Indiana University, in partial fulfillment of the requirements of the degree of Doctor of Philosophy.

Doctoral Committee

Andrzej Zieminski, Ph.D.
(Chairman)

Rick Van Kooten, Ph.D.

Daria Zieminska, Ph.D.

November 15, 2004

Mike Berger, Ph.D.

To my parents, my wife and lovely kids Michelle and Michael Huang.

Acknowledgements

First of all, I would like to thank my advisors, Prof. Andrzej Zieminski and Dr. Daria Zieminska for their guidance, support and attention to detail over the 5 years. Their knowlege and enthusiasm, unique way of approaching problems have been a continual source of inspiration for me.

I would like to thank Prof. Rick Van Kooten and Prof. Mike Berger for their expert comments and corrections on this thesis.

I would like to thank all DØ colleagues whose contributtions made the experiment a success. My special thanks go to Dr. Rick Jesik and Dr. Daniela Bauer for all their kind help and valuable suggestions on this analysis. I feel lucky to share the office with them. I also want to thank Dr. Al Ito and Prof. Darien Wood for their great help during my work on the muon detector alignment and calibration databases.

I thank all my friends at Fermilab: Drs. Chunhui Luo, Zhongmin Wang, Yuan Hu, Qichun Xu, Xiaojian Zhang, Junjie Zhu, Shaohua Fu, Mingchen Gao, Yi Jiang, Huishi Dong, Abaz Kryemadhi. Their friendship makes life at Fermilab more enjoyable.

Finally, I am so grateful to my wife, Feng Wang, for her love, support and encouragement throughout these years!

Abstract

The production of heavy quarkonium in hadronic collisions provides an ideal testing ground for our understanding of the production mechanisms for heavy quarks and the non-perturbative QCD effects that bind the quark pairs into quarkonium. In this analysis, the inclusive production cross section of the $\Upsilon(1S)$ bottomonium state is measured using the $\Upsilon(1S) \to \mu^+\mu^-$ decay mode. The data sample corresponds to an integrated luminosity of 159.1 ± 10.3 pb^{-1}. We determine differential cross sections as functions of the $\Upsilon(1S)$ transverse momentum, p_T^{Υ}, for three ranges of the $\Upsilon(1S)$ rapidity: $0 < |y^{\Upsilon}| < 0.6, 0.6 < |y^{\Upsilon}| < 1.2$ and $1.2 < |y^{\Upsilon}| < 1.8$. The shapes of $d\sigma/dp_T$ cross sections show little variation with rapidity and are consistent with the published Run I CDF measurement over the rapidity range $|y^{\Upsilon}| < 0.4$.

Contents

List of Tables

List of Figures

Chapter 1

Introduction

From the time human beings began to ask questions about themselves and the world around them, they have wondered what the world is made of and how it behaves. High-energy or Particle Physics is the fundamental science that pursues answers to these very ancient and modern questions. It has yielded extraordinary advances in knowledge that makes our universe more understandable—the Standard Model (SM).

In this thesis, Chapter 1 gives a brief review of the Standard Model and provides the physics motivation for the thesis topic: "$\Upsilon(1S)$ bottomonium production at the Fermilab Tevatron"; Chapter 2 reviews different quarkonium production models. The Fermilab Tevatron accelerator complex and the technical details of the DØ detector are described in Chapter 3. Chapter 4 presents the alignment and calibration database service work that the author has done for the DØ muon detector. The analysis of the $\Upsilon(1S)$ production cross section is covered in Chapters 5 through 9.

1.1 The Standard Model

The Standard Model [1] is a fundamental and well-tested theoretical framework that describes the interactions of elementary particles via four basic forces. It is

a *Quantum Field Theory* based on the idea of local gauge invariance. The gauge symmetry group of the SM is $SU(3)_C \times SU(2)_L \times U(1)_Y$, where "$C$" refers to the color charge, "L" to the weak isospin and "Y" to the weak hypercharge. $\mathrm{SU}(3)_C$ is the symmetry group describing the strong interactions, whereas $\mathrm{SU}(2)_L \times \mathrm{U}(1)_Y$ represents the symmetry group describing the unified weak and electromagnetic interactions.

According to the Standard Model, the fundamental particles are of two types: fermions, with half-integral spin that obey Fermi-Dirac statistics, and bosons, with integral spin, which obey Bose-Einstein statistics. The fermions can be further divided into two classes of particles called quarks and leptons. There are six flavors of quarks and leptons, grouped pairwise into 3 generations as shown in Table 1.1 [2]. The six quarks are the up (u), down (d), charm (c), strange (s), top (t) and bottom (b) quarks, and each quark flavor has three possible color states (Red, Green, Blue). The six leptons are the electron (e), muon (μ), tau (τ), and their corresponding neutrinos (ν_e, ν_μ and ν_τ). For each particle, there also exists an anti-particle[1] with the same mass and spin, but with opposite values for some other properties, such as electric charge.

Generation	Quarks (spin=1/2)			Leptons (spin=1/2)		
	Flavor	Charge ($\lvert e\rvert$)	Mass (GeV/c^2)	Flavor	Charge ($\lvert e\rvert$)	Mass (MeV/c^2)
1	u	$+2/3$	$(1.5-4.5)\times10^{-3}$	e	-1	0.511
	d	$-1/3$	$(5-8.5)\times10^{-3}$	ν_e	0	$<3\times10^{-6}$
2	c	$+2/3$	$1.0-1.4$	μ	-1	105.66
	s	$-1/3$	$0.08-0.155$	ν_μ	0	<0.19
3	t	$+2/3$	178 ± 4.3	τ	-1	1776.99
	b	$-1/3$	$4.0-4.5$	ν_τ	0	<18.2

Table 1.1: Quarks and leptons in the Standard Model.

[1]Some particles are their own anti-particles.

All matter is constructed from quarks and leptons and the forces between these elementary particles are mediated by the gauge vector bosons. In order of strength, the forces are the strong, electromagnetic, weak and gravitational force, and their properties are shown in Table 1.2.

Strong interactions are described by Quantum Chromodynamics (QCD) [3]. It is based on the $SU(3)_C$ symmetry group, where the symmetry is based on the three quark colors. Local gauge invariance for this symmetry requires eight $(3^2 - 1)$ massless gauge bosons, i.e., gluons. Two properties that characterize QCD are called *Asymptotic Freedom* and *Quark Confinement*. The gluon-gluon interaction results in a running strong coupling constant, i.e., the coupling strength is dependent on the distance between the interacting particles. At very short distances, the coupling strength is very small and quarks behave like free particles (*Asymptotic Freedom*). But when two quarks move apart from each other, the increasing force will either bind the quarks together or lead to the creation of quark-antiquark pairs, which results in two separate hadrons. This implies that physical particles must be color singlets (i.e., color neutral) and also explains the absence of free quarks (*Quark Confinement*).

The electroweak sector of the Standard Model is a gauge theory that unifies the weak and electromagnetic interactions. The gauge symmetry group $SU(2)_L \times U(1)_Y$ requires $(2^2 - 1) + 1 = 4$ massless gauge bosons. However, to describe the weak interaction, the so-called Higgs Mechanism [4] (spontaneous symmetry breaking [5]

Force	Mediator	Strength	Mass (GeV)	Spin	Range(m)
Strong	Gluon (g)	1	0	1	10^{-15}
EM	Photon (γ)	10^{-2}	0	1	∞
Weak	$W^{\pm}/Z^0$	10^{-6}	80.4/91.2	1	10^{-18}
Gravity	Graviton	10^{-40}	0	2	∞

Table 1.2: Properties of the four fundamental forces.

) is used to break the symmetry group and to give mass to the bosons by introducing a new particle called Higgs boson. As a result, 3 of the 4 gauge bosons acquire a mass and are identified as the $W^{\pm}$ and the Z^0 while the photon, γ, remains massless. To date, the Higgs boson has not been observed.

1.2 Physics Motivation of this Research

Heavy quarkonium production in hadronic collisions provides an ideal testing ground for our understanding of QCD. It involves both perturbative and nonperturbative processes. The production of the heavy quark pair occurs at short distances and can be calculated perturbatively due to the large scale of the quark masses, whereas the nonpertubative QCD effects that bind the heavy quark-antiquark pair into quarkonium can only be factorized into a wave function. Recent advances in the understanding of quarkonium production have been stimulated by the unexpectedly large cross sections for direct J/ψ and $\Upsilon(nS)$ production at large p_T measured at the Fermilab Tevatron [6].

Three types of models have been used to describe quarkonium formation: the color-singlet model [7]; the color-evaporation model [8] with a follow-up soft color interaction model [9]; and the color-octet model [10]. In the color-singlet model, the quarkonium meson retains the quantum numbers of the produced $c\bar{c}$ ($b\bar{b}$) pair, and thus each J^{PC} state can only be directly produced via the corresponding hard scattering color-singlet sub-processes. In the color-evaporation model, the directly produced quarkonium meson is not constrained to the same J^{PC} state as the $c\bar{c}$ ($b\bar{b}$) pair produced in the hard scatter because of the emission of soft gluons during the meson's formation. The color-octet mechanism extends the color-singlet approach by taking into account the production of $c\bar{c}$ ($b\bar{b}$) pairs in a color-octet configuration. The

color-octet state evolves into a color-singlet state via emission of soft gluons.

The production of bottomonium is somewhat simpler than the charmonium state production in that there is no contribution from b quark decays. Hence, bottomonium states are expected to be produced promptly, i.e., at the primary vertex, and to be isolated in space from other interaction products. However, a fraction of $\Upsilon(nS)$ mesons are produced indirectly as a result of a decay of a higher mass state, e.g., a radiative decay $\chi_b \to \Upsilon(1s)\gamma$ or $\Upsilon(2S) \to \Upsilon(1s)\pi\pi$. The known spectrum of the bottomonium states is shown in Fig. 1.1.

The only detailed studies of the $\Upsilon(nS)$ production at the Tevatron based on the Run I (1992 – 1996) data were done by the CDF Collaboration [12–14]. The DØ Collaboration extracted a signal of 90 $\Upsilon(nS)$ events in Run I.

In Run II, with the integrated luminosity increased by a factor of 2, the new tracking system, the expanded and improved muon coverage and the upgraded trigger system, DØ has recorded $\sim$200 pb^{-1} of high quality data between June 2002 and September 2003. We use this data sample to measure the $\Upsilon(1S)$ cross section as function of the $\Upsilon(1S)$ transverse momentum, p_T^{Υ}, for three ranges of the $\Upsilon(1S)$ rapidity: $0 < |y^{\Upsilon}| < 0.6, 0.6 < |y^{\Upsilon}| < 1.2$ and $1.2 < |y^{\Upsilon}| < 1.8$ at a center-of-mass energy of $\sqrt{s}$ =1.96 TeV. As one of the first absolute cross section measurements at DØ in Run II, this analysis was not only motivated by the physics interests described above, but also provide a comprehensive study of the DØ muon system performance on which other analyses can build.

A final note: during the summer of 2002, the author participated in the analysis of the J/ψ production cross section using the data sample of $\sim$4.74 pb^{-1}, collected by DØ from February to May 2002. The results of this analysis, that have been presented at many conferences, and described in detail in Ref. [15], are summarized in Appendix A.

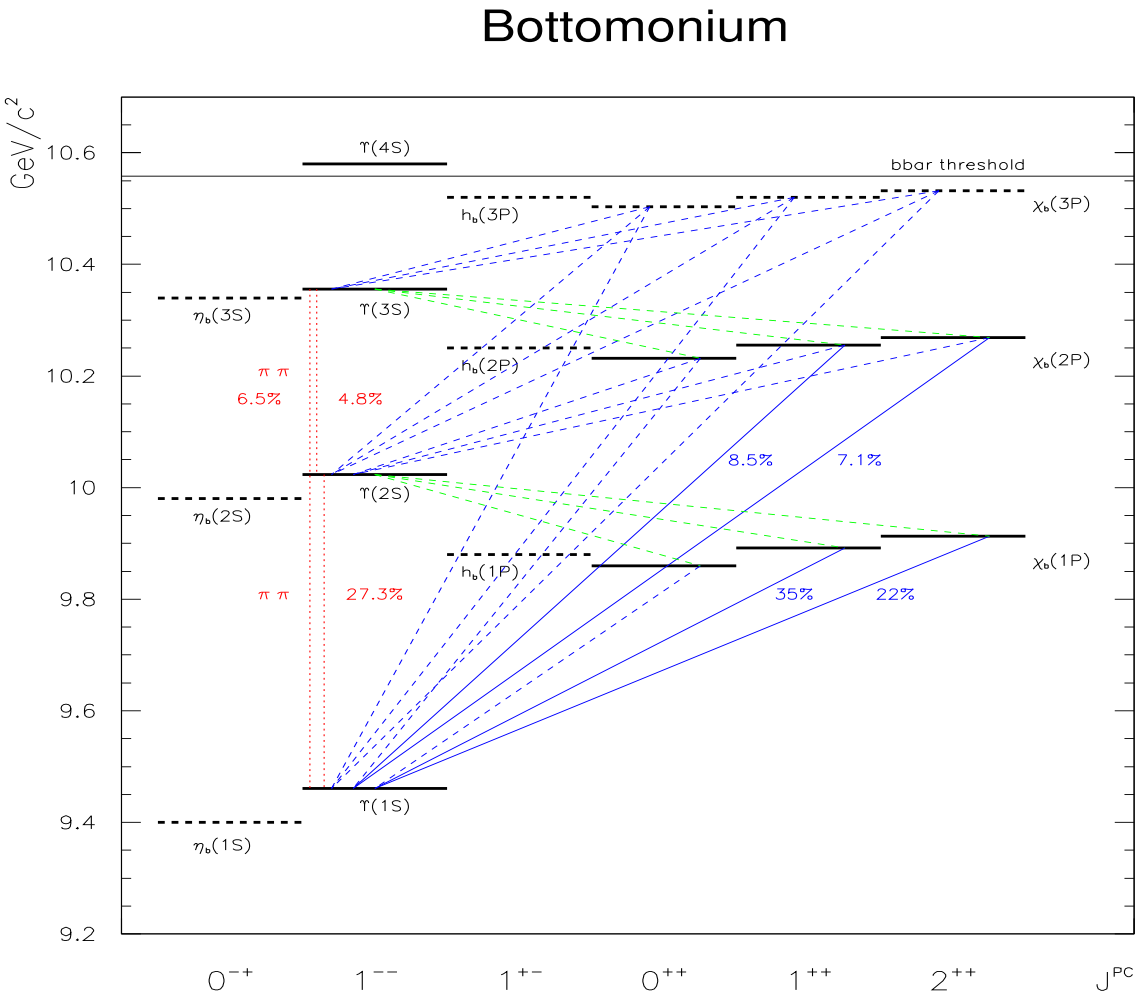

Figure 1.1: Bottomonium states and transitions [11].

Chapter 2

Quarkonium Production

This chapter gives a brief review of the theoretical developments in heavy quarkonium production [16 –18]. As mentioned in the previous chapter, three types of models have been developed to describe the quarkonium formation: the Color-Singlet Model (CSM), the Color-Evaporation model (CEM), and the Color-Octet model (COM).

2.1 Quarkonium Production Models

The first quarkonium production description in hadron collisions was based on calculations in the Color-Singlet Model. In this model, the production of a quarkonium state is assumed to proceed through parton processes that produce a $q\bar{q}$ pair in a color-singlet state with the appropriate quantum numbers. The cross section for producing a quarkonium state in any high energy process can be predicted in terms of a single nonperturbative parameter for each orbital-angular-momentum multiplet. Despite its great predictive power, the model is incomplete. The predictions of the CSM at the lowest order in α_s disagree dramatically with the Tevatron data. This discrepancy lead to two theoretical developments in heavy quarkonium physics. The first was the realization that heavy quarkonium at large transverse momentum is produced primarily by fragmentation, the hadronization of individual high p_T partons.

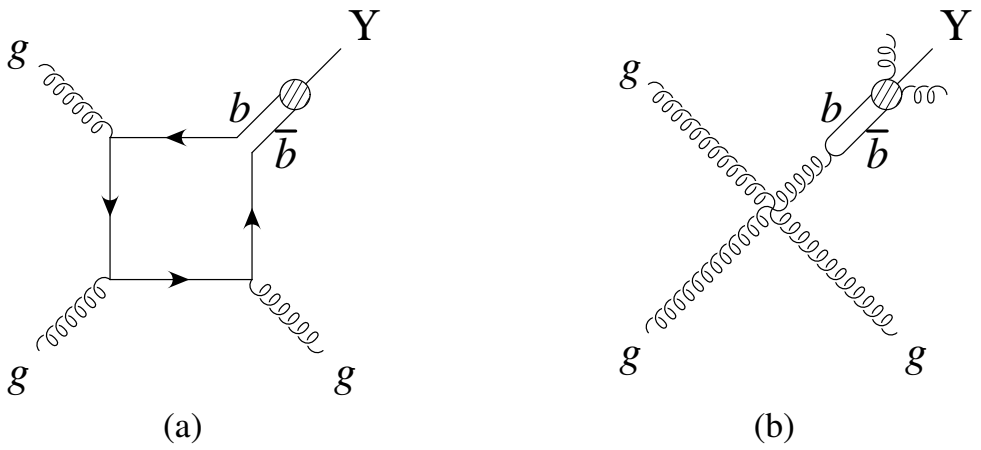

Figure 2.1: Quarkonium production: (a) Color-Singlet mechanism, (b) Color-Octet mechanism.

The second development was the idea that the color-octet mechanism in which the $q\bar{q}$ pair is produced at short distances in a color-octet state sometimes dominates the production. This is often referred to as Color Octet Model (COM). Contrary to the basic assumption of the CSM, a $q\bar{q}$ that is produced in a color-octet state can also bind to form quarkonium. These mechanisms can be analyzed systematically using the factorization formalism based on an effective field theory called Non-Relativistic QCD (NRQCD). Figure 2.1 shows the Feynman diagrams of the CSM and COM.

At the same time as the CSM, an alternative model for quarkonium production called the Color-Evaporation Model was developed [8]. It assumes the color exchange in the soft interactions randomize the color charges such that no information remains of the color configuration given by the proceeding hard interactions. Probabilities for color charge states can be obtained from color SU(3) algebra, with the relation $3 \otimes 3 = 1 \oplus 8$ being applicable to a $q\bar{q}$ pair composed of a triplet and an anti-triplet. With all color charge states having equal weight, this implies that the $q\bar{q}$ pair has a probability 1/9 to be in a color singlet state and 8/9 to be in a color octet state.

All color singlet $q\bar{q}$ pairs with invariant mass below the threshold for open charm or bottom will form a quarkonium state. Color singlet states above this threshold, as well as the $q\bar{q}$ pairs in a color octet state will produce open charm or bottom through the hadronization mechanism. The cross section for quarkonium and open quarkonium (in the case of bottomonium) can then be written as :

$$\sigma_{b\bar{b}} = \frac{1}{9}\int_{2m_b}^{2m_B} dm_{b\bar{b}} \frac{d\sigma_{b\bar{b}}}{dm_{b\bar{b}}}, \tag{2.1}$$

$$\sigma_{open} = \frac{8}{9}\int_{2m_b}^{2m_B} dm_{b\bar{b}} \frac{d\sigma_{b\bar{b}}}{dm_{b\bar{b}}} + \int_{2m_B}^{\sqrt{s}} dm_{b\bar{b}} \frac{d\sigma_{b\bar{b}}}{dm_{b\bar{b}}}, \tag{2.2}$$

where $m_{b\bar{b}}$ is the invariant mass of the $b\bar{b}$, m_b is the bottom quark mass and $2m_B$ is the $B\bar{B}$ threshold. The differential parton level cross $\frac{d\sigma_{b\bar{b}}}{dm_{b\bar{b}}}$ is the usual convolution of the perturbative QCD cross section with the parton density functions for the initial hadrons.

The total quarkonium cross section is then split in the different quarkonim states:

$$\sigma_i = \rho_i \sigma_{b\bar{b}}, \tag{2.3}$$

where relative rates ρ_i are assumed to be independent of process and energy. These non-perturbative parameters must be determined from comparison with data.

The CEM is one of the simplest approaches to color neutralization, where the effect of soft interactions is implicit in the non-perturbative factors.

2.2 Non-Relativistic QCD Factorization Method

The Non-Relativistic QCD factorization method is a general factorization formalism. This formalism can be used to factor quarkonium production cross sections into the short-distance parts that can be calculated using perturbative QCD and the long distance effects that are factored into parameters called NRQCD matrix elements. These nonperturbative parameters are universal, so values extracted from one high energy physics experiment can be used to predict the production rate in others.

According to the NRQCD [19], the differential cross section of inclusive production of a bottomonium state H with momentum P has the schematic form:

$$d\sigma[H(P)] = \sum_n d\sigma[b\bar{b}(n,P)]\langle O^H(n)\rangle, \tag{2.4}$$

where the sum extends over both color-singlets and color-octets and over all angular momentum channels for the $b\bar{b}$ pair. The $b\bar{b}$ cross sections, which are independent of the bottomonium state H, can be calculated using perturbative QCD.

In the case of direct $\Upsilon(nS)$ production, equation 2.4 can be written as:

$$\begin{aligned} d\sigma[\Upsilon(nS)] &= d\sigma[b\bar{b}_1(^3S_1)]\langle O_1^{\Upsilon(nS)}(^3S_1)\rangle \\ &+ d\sigma[b\bar{b}_8(^3S_1)]\langle O_8^{\Upsilon(nS)}(^3S_1)\rangle \\ &+ d\sigma[b\bar{b}_8(^3S_0)]\langle O_8^{\Upsilon(nS)}(^3S_0)\rangle \\ &+ (\sum_J (2J+1) d\sigma[b\bar{b}_8(^3P_J)]\langle O_8^{\Upsilon(nS)}(^3P_0)\rangle, \end{aligned} \tag{2.5}$$

where $\langle O_1^{\Upsilon(nS)}(^3S_1)\rangle$ is the color-singlet matrix element and $\langle O_8^{\Upsilon(nS)}(^3S_1)\rangle$,$\langle O_8^{\Upsilon(nS)}(^3S_0)\rangle$

and $\langle O_8^{\Upsilon(nS)}(^3P_0)\rangle$ are the three color-octet matrix elements.

Taking into account the feeddown from higher states as shown in Fig. 1.1, the inclusive $\Upsilon(nS)$ cross sections are given by:

$$\begin{aligned} d\sigma[\Upsilon(nS)]_{inc} &= d\sigma[b\bar{b}_1(^3S_1)]\langle O_1^{\Upsilon(nS)}(^3S_1)\rangle_{inc} \\ &+ d\sigma[b\bar{b}_1(^3P_J)]\langle O_1^{\Upsilon(nS)}(^3P_J)\rangle_{inc} \\ &+ d\sigma[b\bar{b}_8(^3S_1)]\langle O_8^{\Upsilon(nS)}(^3S_1)\rangle_{inc} \\ &+ d\sigma[b\bar{b}_8(^3S_0)]\langle O_8^{\Upsilon(nS)}(^3S_0)\rangle_{inc} \\ &+ (\sum_J (2J+1) d\sigma[b\bar{b}_8(^3P_J)]\langle O_8^{\Upsilon(nS)}(^3P_0)\rangle_{inc}, \end{aligned} \tag{2.6}$$

where the inclusive NRQCD matrix elements are:

$$\langle O^{\Upsilon(nS)}[n]\rangle_{inc} = \sum_H B_{H\to\Upsilon(nS)}\langle O^H[n]\rangle. \tag{2.7}$$

The sum over H includes $\Upsilon(nS)$ and all higher bottomonium states that can make transitions to $\Upsilon(nS)$. The coefficient $B_{H\,\to\,H'}$ is the inclusive branching fraction for H to decay into H'. It is measured experimentally [19].

These NRQCD matrix elements can be extracted by fitting to our measurements discussed in later chapters. The resulting values can be used to predict the cross sections and polarizations of the bottomonium states. At high p_T, the matrix element $\langle O_8^{\Upsilon(nS)}(^3S_1)\rangle_{inc}$ represents the gluon fragmentation contributions. The NRQCD predicts [20] the $\Upsilon(1S)$ is transversely polarized at high p_T (due to the contribution from gluon fragmentation) as shown in Fig. 2.2. The parameter $\alpha = 1$ (-1) corresponds to 100% transverse (longitudinal) $\Upsilon(nS)$ polarization. The model also predicts a much larger polarization for the more massive bottomonium states $\Upsilon(2S)$ and $\Upsilon(3S)$, which

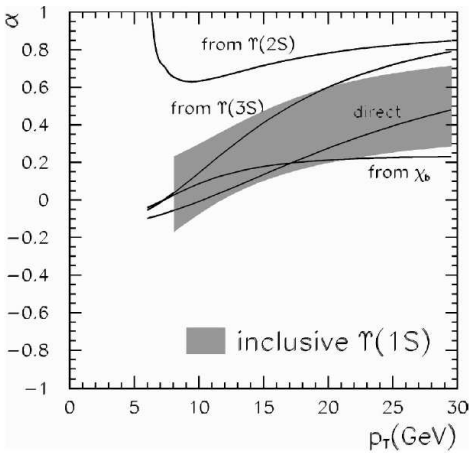

Figure 2.2: Polarization variable α vs p_T at $\sqrt{s} = 2.0$ TeV for inclusive $\Upsilon(1S)$.

are produced more directly than $\Upsilon(1S)$.

2.3 Summary of the Experimental Findings

The models discussed above for quarkonium formation lead to different expectations for the production rates and polarization of the quarkonium states. A priori, the same sets of parameters should apply to a variety of processes involving quarkonium production, including

1. quarkonium production at Tevatron Collider;
2. quarkonium production in hadron-nucleon collisions at fixed target energies;
3. production polarization measurements;
4. inelastic charmonium production at HERA;
5. $BR(Z \rightarrow \text{prompt } J/\psi + X)$ at LEP;

6. associated production of a $J/\psi + \gamma$, double J/ψ production;

7. and related processes such as rapidity gaps in hadronic and ep collisions.

For $\Upsilon(nS)$ production at the Tevatron [12–14], the most important CDF Run I findings are:

- Inclusive cross sections for $\Upsilon(nS)$ states in the rapidity range $|y^{\Upsilon}| < 0.4$ are in excess of the predictions of the Color Singlet Model by more than an order of magnitude for $p_T^{\Upsilon} > 10$ GeV/c [19].

- Approximately 50% of $\Upsilon(1S)$ mesons are produced directly.

- $\Upsilon(1S)$ polarization for $8 < p_T^{\Upsilon} < 20$ GeV/c is $\alpha = -0.12 \pm 0.22$.

  This result is consistent with the prediction of the NRQCD [20]. Our very preliminary polarization result for $\Upsilon(1S)$ is $\alpha = -0.11 \pm 0.16$ ($8.0 < p_T^{\Upsilon} < 16.0\ GeV/c$) is shown in Appendix B. It is also consistent with the CDF Run I and the NRQCD prediction.

A recent paper [21] successfully reproduces the transverse momentum distribution of upsilon states produced at Tevatron energies by combining separate perturbative approaches for low- and high-p_T regions. However, several model parameters have been adjusted to match the data, and the absolute cross section is not predicted by these calculations. In another very recent paper [22], the prompt hadroproduction cross sections of upsilon states are calculated in leading-order perturbative QCD. The results are consistent with the Tevatron values even without invoking non-perturbative "color-octet" type of contributions.

A much larger transverse polarization for $\Upsilon(2S)$ and $\Upsilon(3S)$ than for $\Upsilon(1S)$ has also recently been observed in bottomonium production in the p-Cu collisions at $\sqrt{s} = 38.9$ GeV by the Fermilab E866/NuSea Collaboration [23].

For a review of the experimental results on quarkonium production in Run I as well as from other relevant experiments, see Ref. [24]. Table 2.1 (from Ref. [25]) gives the most recent summary of the ongoing experiments studying quarkonium production. The same review provides a scorecard for different models, as shown in Fig 2.3. Whereas the Color Singlet Model (CSM) fails to describe the charmonium production at the Tevatron and the bottomonium polarization at the fixed target energies, it is more successful in describing the J/ψ production at the ep machines (HERA). An absence of the J/ψ polarization, observed at both the Tevatron and the fixed target energies is a setback for the Color Octet Model.

Experiment	Beams(GeV)	$\sqrt{s}$(GeV)	Run	Data
FOCUS/E831	$\gamma(175) - BeO$	18	96-97	
NuSea/E866	$p(800) - Cu$	38	96-97	9M J/ψ
SELEX/E781	$\sigma^-, \pi^-(600) - CCu$	33	96-97	15 B
Hera-B	$p(920) - C, Al, Ti, W$	41	00,02-03	308K J/ψ
Hera-I	$e^{\pm}(27.6) - p(890, 920)$	300,318	93-00	130 pb^{-1}
Hera-II	$e^{\pm}(27.6) - p(920)$	318	03-04	$\sim$ 70 pb^{-1}
LEP	$e^+(45, \sim 100) - e^-(45, \sim 100)$	90,210	89-00	3.6M bb
Tevatron I	$p(900) - \bar{p}(900)$	1800	92-96	125 pb^{-1}
Tevatron II	$p(980) - \bar{p}(980)$	1960	02-04	$\sim$ 200 pb^{-1}

Table 2.1: Summary of recent experiments for heavy quarkonium production from Ref. [25].

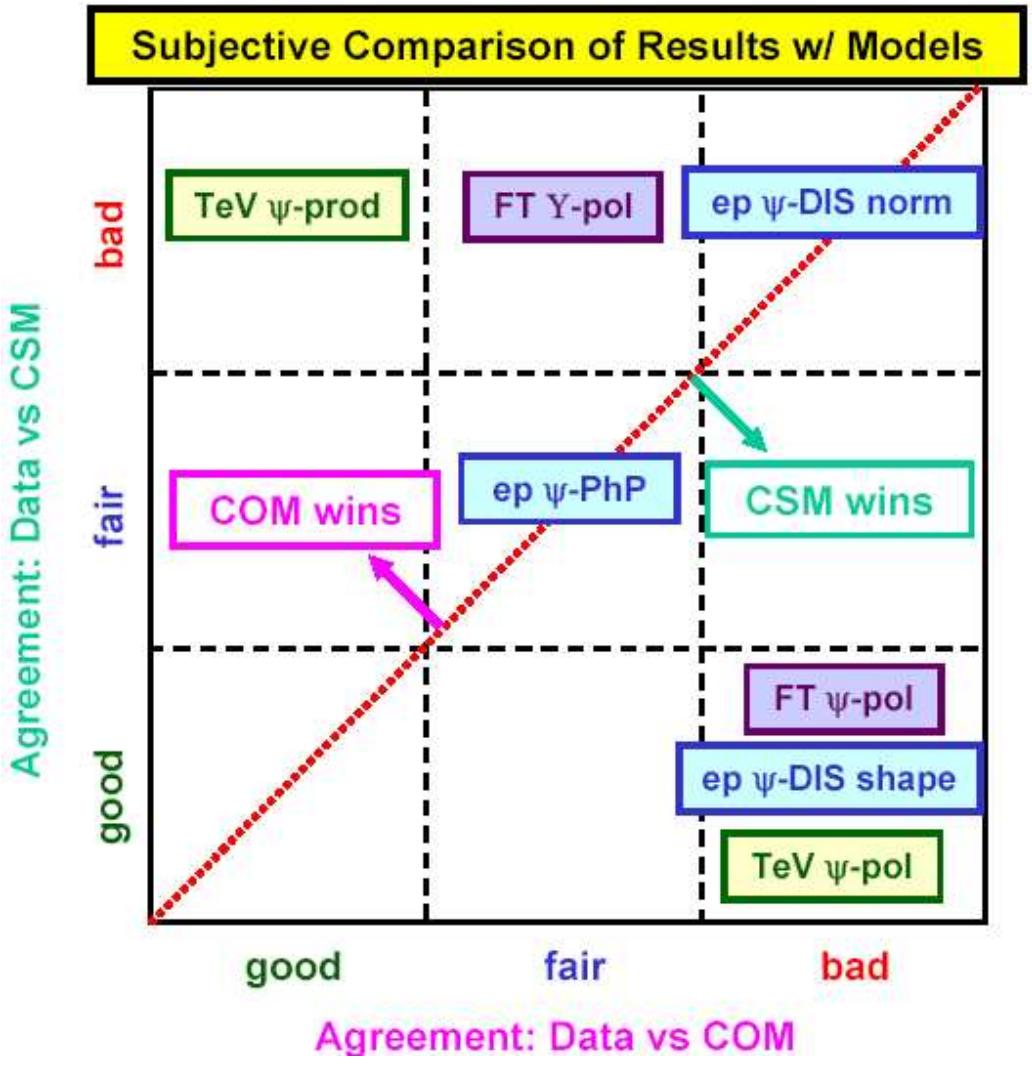

Figure 2.3: Scorecard for different quarkonium production models from Ref. [25].

Chapter 3

Experimental Apparatus

This chapter provides a brief overview of the Fermilab Tevatron accelerator complex and the technical details of the DØ detector, with emphasis on the muon systems.

3.1 The Tevatron Accelerator Complex

The Tevatron accelerator complex [26, 27] is a series of accelerators that are necessary to produce the colliding proton and anti-proton beams. The main components of the chain are: Cockcroft-Walton Pre-Accelerator, Linear Accelerator (The Linac), Booster synchrotron, Main Injector, Antiproton Source, Debuncher and Accumulator, Recycler, and the Tevatron. A schematic view of the Tevatron accelerator complex is shown in Fig. 3.1.

3.1.1 Pre-Accelerator, LINAC and the Booster

The proton beam starts as a pulsed negative hydrogen ion beam (H^-) from a magnetron surface-plasma source. These ions are first accelerated to 750 keV by the Cockcroft-Walton Pre-Accelerator, then injected to the linear accelerator that raises the energy to 400 MeV. Prior to the booster, the ions pass through a carbon foil,

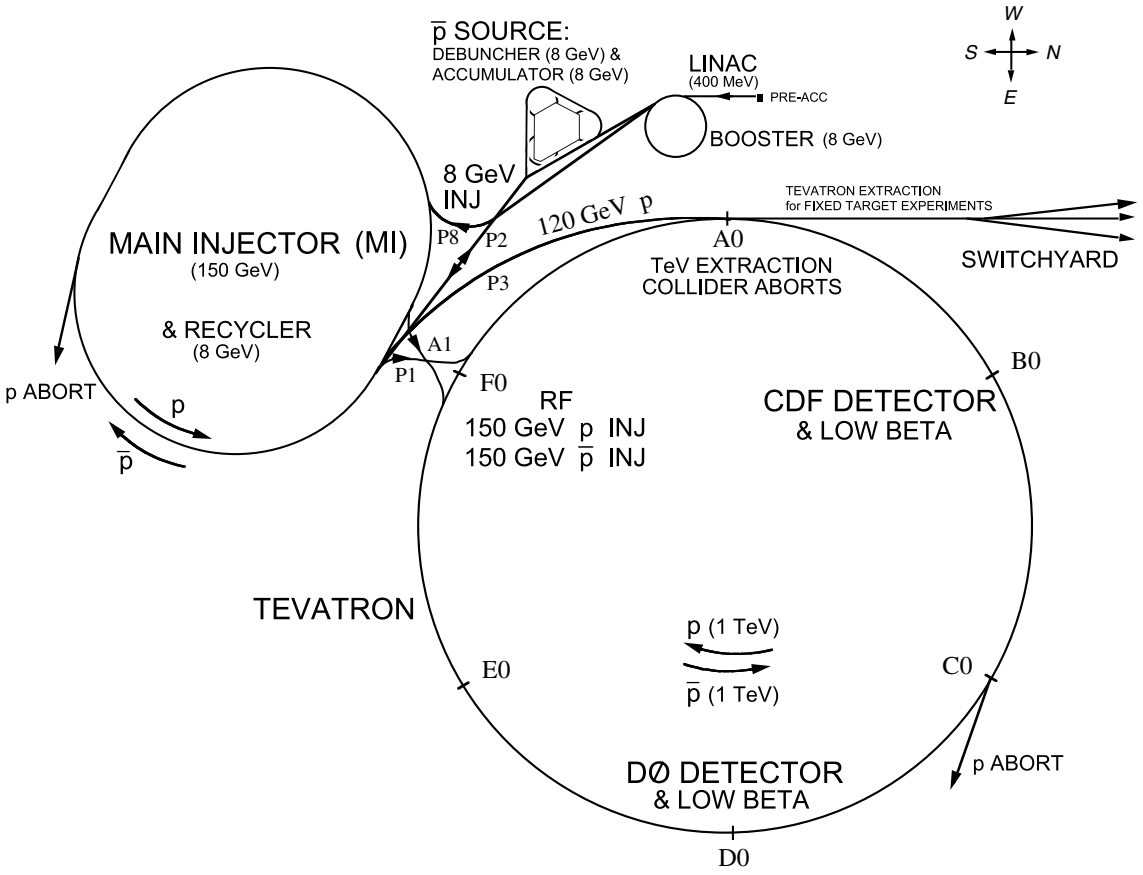

Figure 3.1: Fermilab accelerator complex.

which strips electrons from the H^- ion, leaving only the proton. Within the Booster, the protons reach an energy of 8 GeV and are injected into the next acceleration stage, the Main Injector.

3.1.2 The Main Injector and Antiproton Production

In Run II, the major upgrades include the new the Main Injector(MI) [28] and the Recycler within a common tunnel. The Main Injector is a 150 GeV synchrotron with a circumference of about 2 miles and capable of delivering three times as many protons to the Tevatron as the old Main Ring. It coalesces proton bunches from the Booster into a single high intensity bunch of approximately 5×10^{12} protons and accelerates them up to 150 GeV.

When protons in the MI are accelerated to the energy of 120 GeV, they can also be extracted to impact on an external nickel/copper target to produce antiprotons. The antiprotons are then injected into the antiproton storage ring. It comprises the Debuncher and the Accumulator. Within the Debuncher, the momentum spread of the selected 8 GeV antiprotons reduced by a process known as stochastic cooling. Once a small emittance beam is achieved, the antiprotons are transferred to the Accumulator, where they are further cooled and transferred to the Recycler ring.

The Recycler is a 8 GeV permanent magnet storage ring. It acts as not only a storage ring for antiprotons from the accumulator, but also acts as a receptacle for left over antiprotons from the previous store. Once a total stack of antiprotons reaches $\sim 3 \times 10^{12}$, they will be delivered to the the Main Injector and then into the Tevatron.

Run	Run Ib	Run IIa
Energy (GeV)	900	980
Bunches	6×6	36×36
Protons/Bunch	2.3×10^{11}	2.7×10^{11}
Antiprotons/Bunch	5.5×10^{10}	7×10^{10}
Typical Luminosity ($\times 10^{32} cm^{-2} s^{-1}$)	0.16	1.0
Integrated Luminosity (pb^{-1}/week)	3.2	9.0
Bunch Spacing (ns)	3500	396
Interactions/Crossing	2.5	2.3

Table 3.1: Tevatron operation parameters.

3.1.3 The Tevatron

The Tevatron [27] is currently the world's highest energy proton-antiproton particle collider, with a circumference of 6.4 km. Superconducting magnets are cooled to a temperature of 4.8 K and produce fields of 4 Tesla. In Run I (1992 – 1996), the Tevatron operated at a center-of-mass energy of 1.80 TeV, with a typical instantaneous luminosity of 0.16×10^{32} cm^{-2}s^{-1} and delivered an integrated luminosity of $\sim$140 pb^{-1}. In Run II (2001-today), the upgraded Tevatron has increased the center-of-mass energy to 1.96 TeV. The initial instantaneous luminosity has now reached up to 1.1×10^{32} cm^{-2}s^{-1}, with a goal of 2×10^{32} cm^{-2}s^{-1}, and integrated luminosity of $\sim$2 fb^{-1}. The main operation parameters of the Tevatron are listed in Table 3.1.

There are two detectors at Tevatron Collider: the DØ detector and the Collider Detector at Fermilab (CDF). Both detectors have also undergone comprehensive upgrades for Run II.

3.2 The DØ Detector

The DØ Detector was upgraded significantly from 1996 to 2001 in order to operate with the upgraded Tevatron. The upgrade builds on the strengths of DØ, i.e. excellent coverage in calorimetry and muon detection, while enhancing the tracking and triggering capabilities [29]. It considerably improves the experiment's physics ability to study the phenomena involving high p_T and high mass states. These include precision studies of the top quark and W/Z bosons, searches of the Higgs boson and heavy exotic particles like supersymmetric particles. The upgraded DØ detector is shown in Fig. 3.2. We will describe the DØ Coordinate System and each of the sub-detector in the following sections.

3.2.1 DØ Coordinate System

DØ uses a right-handed coordinate system with the positive z-axis along the proton beam direction (from North to South), the y-axis is upwards and the x-axis horizontal, pointing away from the center of the ring.

In the spherical coordinates (r, ϕ, θ), instead of using the polar angle θ, we often use pseudo-rapidity η, which is defined as:

$$\eta \;=\; -\ln[\tan(\theta/2)] \;=\; \tanh^{-1}(\cos\theta). \tag{3.1}$$

In the limit of $m \ll E$, the pseudo-rapidity approaches true rapidity y:

$$\mathrm{y} \;=\; \tfrac{1}{2}\ln(\tfrac{E+p_z}{E-p_z}), \tag{3.2}$$

where E is the particle's energy, m the rest mass, and p_z the momentum in the z-direction.

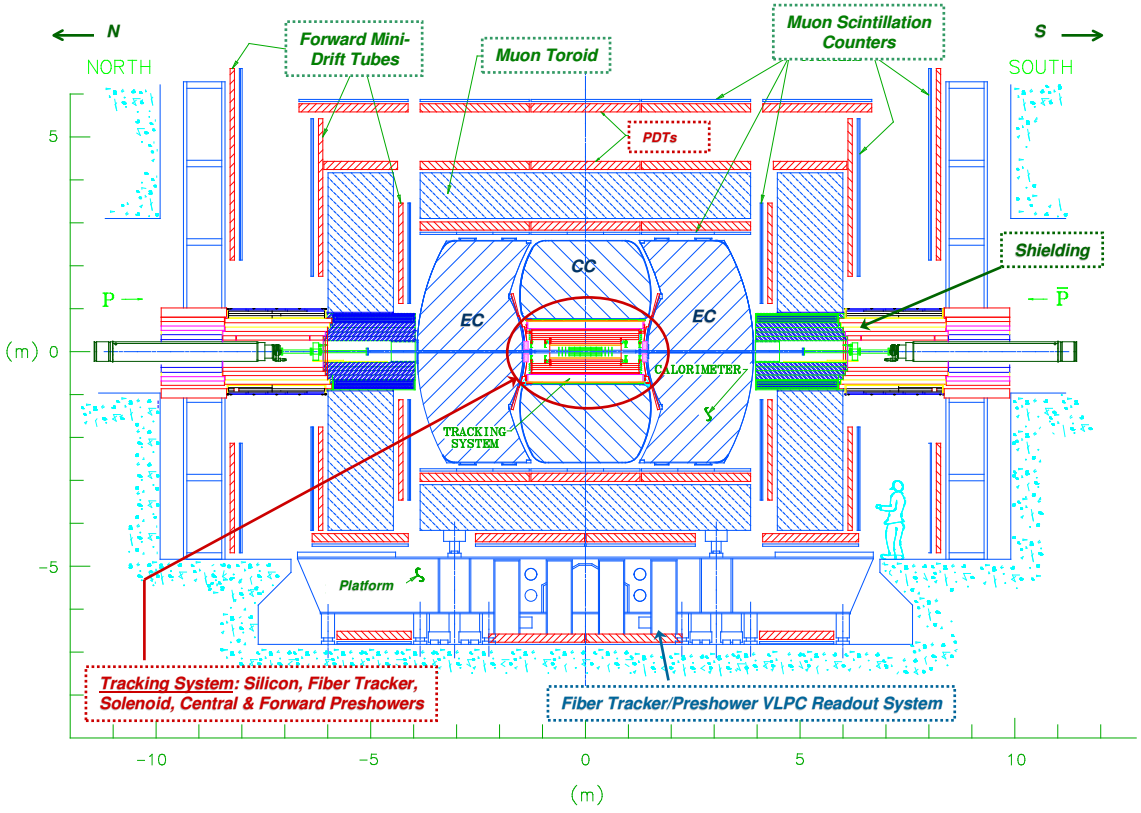

Figure 3.2: Two-dimensional view of the DØ detector.

Because the rapidity is invariant under Lorentz transformations, by using the rapidity, the shape of the particle distribution ($dN/d\eta$) is invariant under boosts along the z-axis.

3.2.2 Central Tracking System

The upgraded DØ central tracking system, shown in Fig. 3.3, consists of a Silicon Microstrip Tracker (SMT), surrounded by the scintillating Fiber Tracker (CFT) and a 2 Tesla superconducting solenoid. The tracking system is designed to meet several goals [29]: momentum measurement with the introduction of a magnetic field; good electron identification and e/π rejection, tracking over a large range in η ($\approx \pm 3$), secondary vertex measurement for identification of b-jets; hardware tracking trigger, fast detector response and radiation hardness.

Silicon Microstrip Tracker

The Silicon Microstrip Tracker [29] [30] is the high resolution part of the tracking system. To account for an extended interaction region with σ_z of 25 cm, the SMT is designed as a hybrid (barrel/disk) system, with barrel detectors measuring primarily the $r-\phi$ coordinate and disk detectors measuring the $r-z$ and $r-\phi$ coordinate. Thus, vertices at small rapidity ($|\eta| < 1.5$) are reconstructed in the barrels and vertices at high rapidity ($1.5 < |\eta| < 3.0$) are measured in the disks.

The SMT, shown in Fig. 3.4, consists of 6 barrel segments in z, 12 small diameter "F" disks and 4 large diameter "H" disks. The 12 cm long barrel segment has 4 layers with radii ranging from 2.6 cm to 10.0 cm. At layer 1 and 3, the 4 central barrel segments are double-sided detectors with axial and 90° stereo strips. The other two

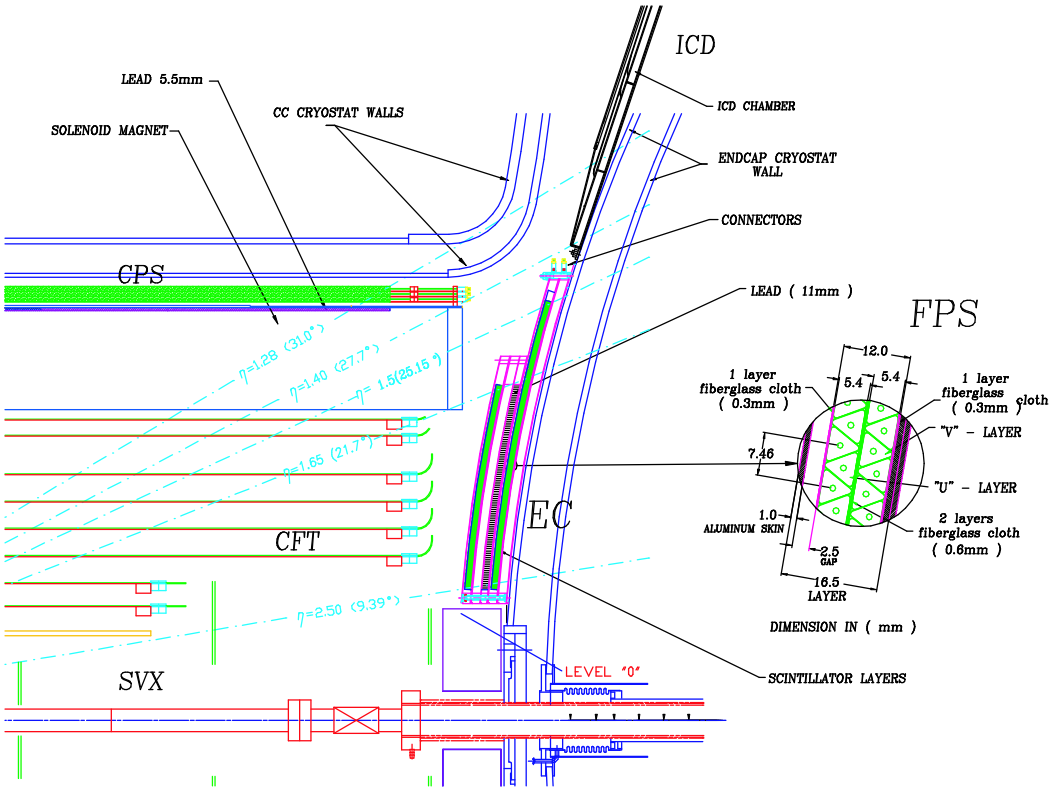

Figure 3.3: One quarter r-z ofview the DØ trackers.

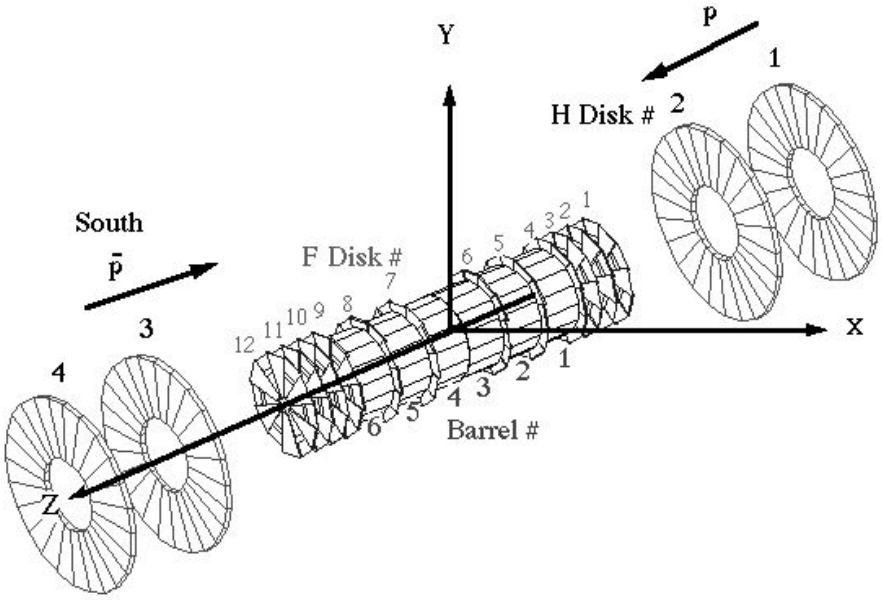

Figure 3.4: The silicon microstrip tracker.

outer barrels at each end are single-sided detectors with axial strips only. The barrel segments at layer 2 and layer 4 are double-sided detectors with axial and 2° stereo strips. F disks are also double-sided detectors with ±15° stereo angle. Four of them are sandwiched between barrel segments with the remaining 8 disks are located at each end of the barrel. The 4 H disks, located at $|z| = 110$ cm and 120 cm are double-sided detectors with a ±7.5° stereo angle. The SMT detector has ∼793k channels in total.

The barrels and the F disks are built on 50 and 62.5 μm small pitch silicon wafers, 300 μm thick, providing a spatial resolution of approximately 10 μm. The small angle stereo detectors provide the pattern recognition necessary to resolve tracks from b decays within jets. The 90° detectors provide resolution in r-z at the vertex of 100 μm. The readout for the SMT and the CFT is based on the 128 channel SVX II chip. The SVX II chips are mounted on a flexible printed circuit called a High Density Interconnect (HDI). At the outer radius of the detector, the HDIs are

connected by two metallic cables to the port cards mounted in crates located on the detector platform. The port card downloads parameters to the SVX II chip and sends their data to the data acquisition system through an optic fiber cable.

Central Fiber Tracker

Surrounding the SMT detector, the Central Fiber Tracker (CFT) serves two main functions: (1) combined with SMT detector, enables track reconstruction and momentum measurement in the $|\eta| < 2.0$ region; (2) provides fast, "Level 1" track triggering in the $|\eta| < 1.6$ region.

The CFT [31] consists of 8 concentric support cylinders with radii ranging from 20 to 50 cm. A fiber doublet layer with the fibers oriented parallel to the beam axis is mounted on each of the eight cylinders. Alternating with each cylinder, an additional doublet layer oriented at a stereo angle of 2° to 3° is mounted on top of the first doublet.

The CFT comprises 76,800 multi-clad scintillating fibers. The inner polystyrene core of each is surrounded by a thin acrylic cladding, which in turn is covered by another thin fluoro-acrylic cladding. The fiber's diameter is 835 μm (775 μm active) and its length ranges from 166 to 252 cm. Each cladding is 15 μm thick. Through an optical connector, the fiber is mated to a clear fiber waveguide that pipes the scintillation light to a photodetector called Visible Light Photon Counter (VLPC) [32]. It is an impurity band silicon-avalanche device that converts the light into electrical signals. The readout for CFT is almost same as that of SMT except there is a special "precursor" chip between the VLPC and the SVX II to provide a prompt Level 1 trigger pickoff.

A cosmic ray test of a large-scale CFT prototype was carried out from 1994 to 1995 [34]. The doublet position resolution, shown in Fig. 3.5, is about 92 μm.

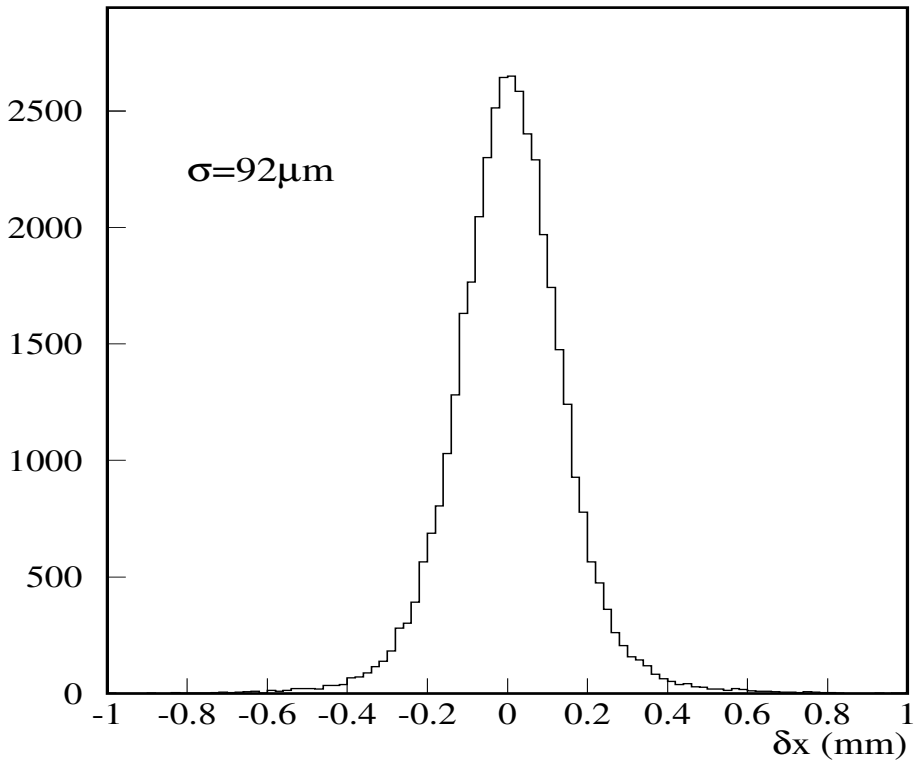

Figure 3.5: Position resolution for CFT fiber doublets from cosmic ray test.

The Solenoid

To determine the momentum of charged particles, a new 2 Tesla superconducting solenoid magnet [33] has been added to the DØ detector for RunII. It is a 2.8 m long two-layer coil with a mean radius of 60 cm. The thickness of the superconducting coil plus its cryostat is about 1.1 radiation lengths. The uniformity of the magnetic field inside the tracking volume is measured to be within 0.5%.

Transverse Momentum Resolution of the Tracking System

The relationship between the transverse momentum, p_T, and the radius of curvature for a charged particle is given by:

$$p_T = 0.3 \times q \times B \times R, \tag{3.3}$$

where R is in meters and q is the charge of the track and B is the magnetic field in Tesla.

Figure 3.6 shows the transverse momentum resolution of the DØ tracking system as a function of η for various p_T. At $\eta = 0$, the resolution can be parameterized as [31]:

$$\frac{\Delta p_T}{p_T} = \sqrt{0.015^2 + (0.0014 \times p_T)^2}, \tag{3.4}$$

where p_T is in GeV/c.

The resolution decreases above $|\eta| = 1.6$, which is due to the loss of the full CFT coverage. The further decrease above $|\eta| = 2.1$ is due to the loss in coverage from the forward SMT disks.

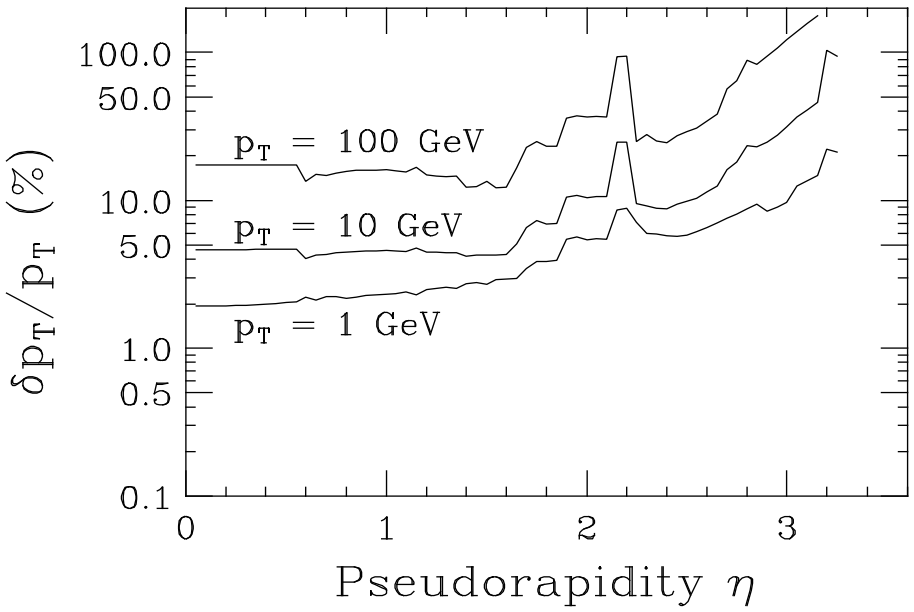

Figure 3.6: Charged particle momentum resolution vs. η of the tracking system.

3.2.3 Calorimeter

At DØ, the calorimeter [35] plays an important role in providing the energy measurement for electrons, photons and jets. They help to identify these particles and muons and establish the transverse momentum balance ("missing E_T") in an event. The calorimeter is a sampling calorimeter. The dense absorbing medium is either uranium or copper. The active medium is liquid argon, producing electrons which induce a pulse signal. When a particle passes through the uranium, it produces a shower of secondary particles (e,π). A correction called the sampling fraction is then

made to convert the fraction of the energy measured to the total energy lost by the particle.

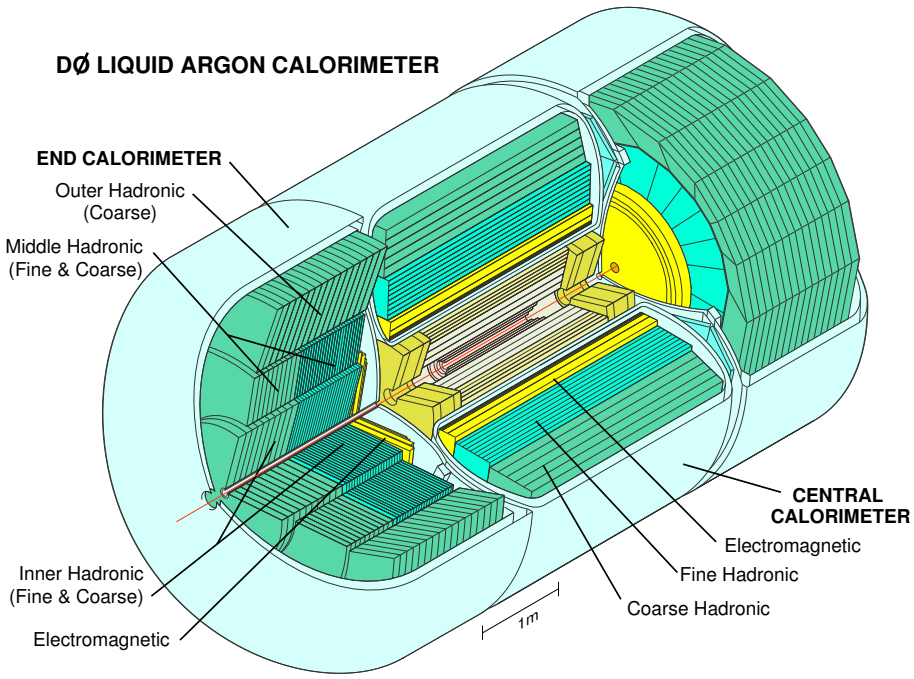

Figure 3.7: Cutaway view of the DØ calorimeter.

The calorimeter is divided into three sections, shown in Fig. 3.7: the Central Calorimeter (CC) covers the region $|\eta| < 1.0$ and two Endcap Calorimeters (EC) located on each side of the CC, cover the region $1.0 < |\eta| < 4.0$. Both CC and EC have three distinct types of modules: an electromagnetic section (EM) with relatively thin uranium absorber plates, a fine hadronic section (FH) with thicker uranium plates, and a coarse hadronic section (CH) with thick copper or stainless steel plates. The Central Calorimeter consists of three concentric cylindrical shells. There are 32 EM modules in the inner ring, 16 FH modules in the surrounding ring, and 16 CH modules in the outer ring. The Endcap Calorimeter contain 1 EM module, 1 inner hadronic module, 16 middle hadronic modules and 16 outer hadronic modules. The

details of the calorimeter segments are described in [35].

The Inter-Cryostat Detectors and Massless Gaps

Because of the structure of the cryostat walls, there is an uninstrumented gap between the central and end calorimeters at $0.8 < |\eta| < 1.4$. To correct for energy deposited in the uninstrumented region, two different types of detector are installed. The Inter-Cryostat Detector (ICD) [36] mounted on the inner face of the EC covers the gap in the region $1.1 < |\eta| < 1.4$. It is a single layer array of scintillating tiles. The Massless Gaps (MG) installed in both of the CC and EC cryostat walls. These are modules consisting of two signal boards surrounded by three liquid argon gaps, using the cryostat walls as absorber. Together, the ICD and MGs provide a good approximation to the standard sampling of EM showers.

3.2.4 Muon System

Muons are minimum ionizing particles that escape the calorimeter into the Muon system without producing EM or hadronic showers. Any charged particle that penetrates the absorbers and reach the muon system is assumed to be a muon.

The DØ muon system [15] [35] [37] is located at the outer-most layer of the DØ detector. It consists of three subsystems: the central muon detector (Proportional Drift Tubes - PDT). The forward muon detector (Mini-Drift Tubes - MDT) and Scintillation counters. The central muon detector provides coverage up to a pseudo-rapidity of $|\eta| \leq 1.0$. The forward muon detector extends muon detection to $|\eta| = 2.2$. Scintillation counters are used for triggering and rejection of cosmic muons and accelerator background. All of them have three layers, designated A, B and C. The A layer is located between the calorimeter and a 2 Tesla toroid magnet. The B and

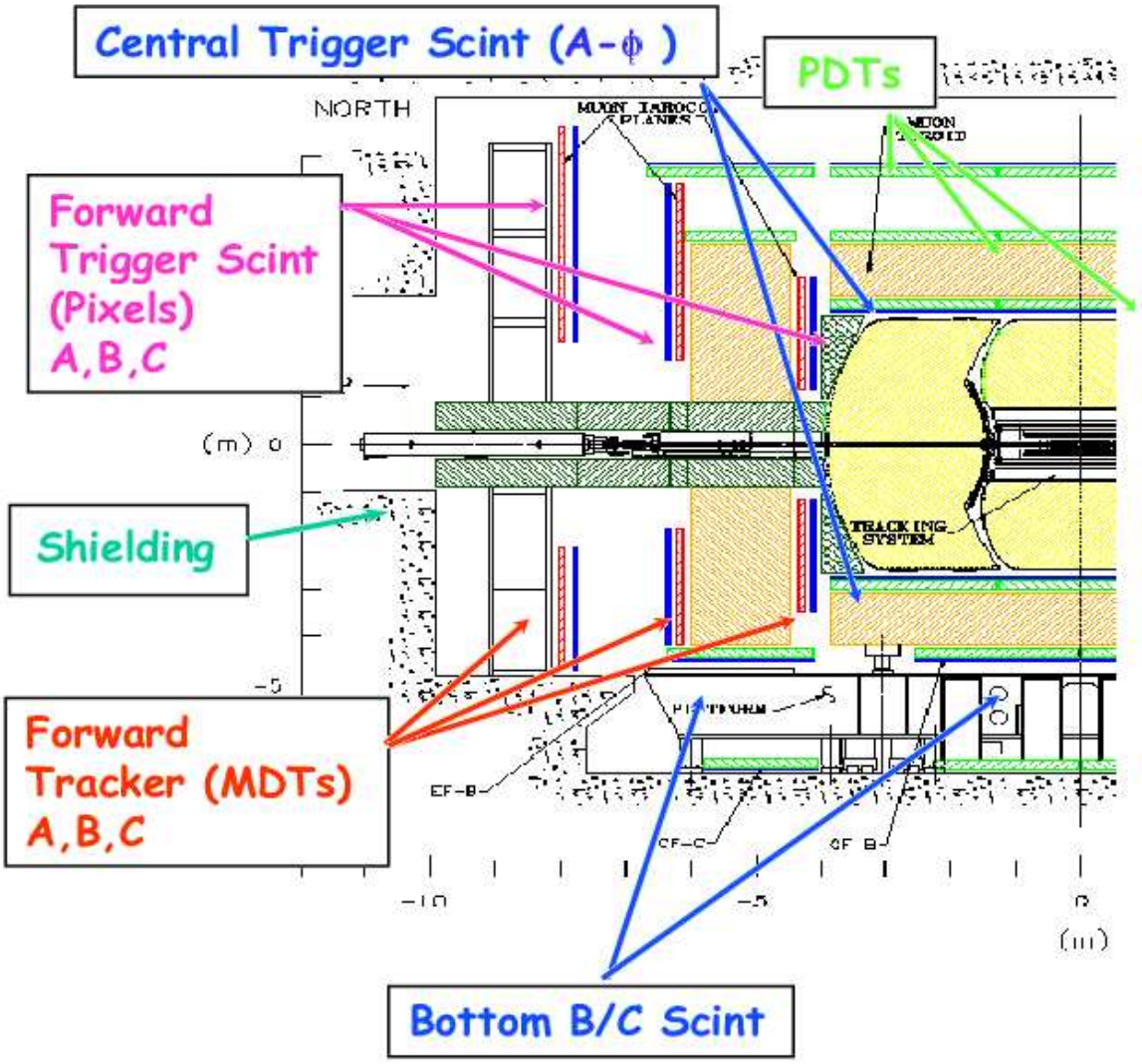

Figure 3.8: The half $r - z$ view of the DØ muon subdetector.

C layers are outside the toroid. To reduce background, shielding materials was added around the beam pipe from the edge of the End cap Calorimeter to the accelerator tunnel. Half r-z view of the DØ muon system is shown in Fig. 3.8. The detailed structures of the central and forward systems are discussed next.

Central Muon Detector

The Central Muon Detector has 94 PDTs in total. The A layer PDTs consist of 4 staggered decks of 24 cells each, except the ones at the bottom that have 3 decks. The B,C layer PDTs consist of 3 staggered decks of 24 cells each. The extruded aluminum cells are 4-inch in width and up to 228 inches long. The wires in the cells are parallel to the field in the toroid magnets so that the bending of the track in the toroids takes place in the drift ordinate (refer to Fig. 3.8 and 3.9).

The gas of the chamber is composed of 80% argon, 10% CF_4, and 10% CH_4 with a drift velocity of 0.1 mm/ns and a maximum drift time of approximately 500 ns. The drift coordinate resolution is $\sim$ 700 μm per hit, limited by the fluctuations in the drift time due to the gas.

The muon momentum is calculated from the bend in the toroid magnet and determined from the difference in slopes between the line formed from the interaction point and the A-layer hits and the line through the B and C layer hits. The momentum resolution is obtained to be $\sigma(1/p) = 0.18(p-2)/p^2 \otimes 0.005$ with p in GeV/c [15].

Forward Muon System

The Forward Muon System consists of 3 or 4 layers of Mini-Drift Tubes (MDT) [38]. The layers are divided into 8 octants. Each octant contains tubes of different lengths and is an independent assembly unit. As in the central region, the A-layer MDT has

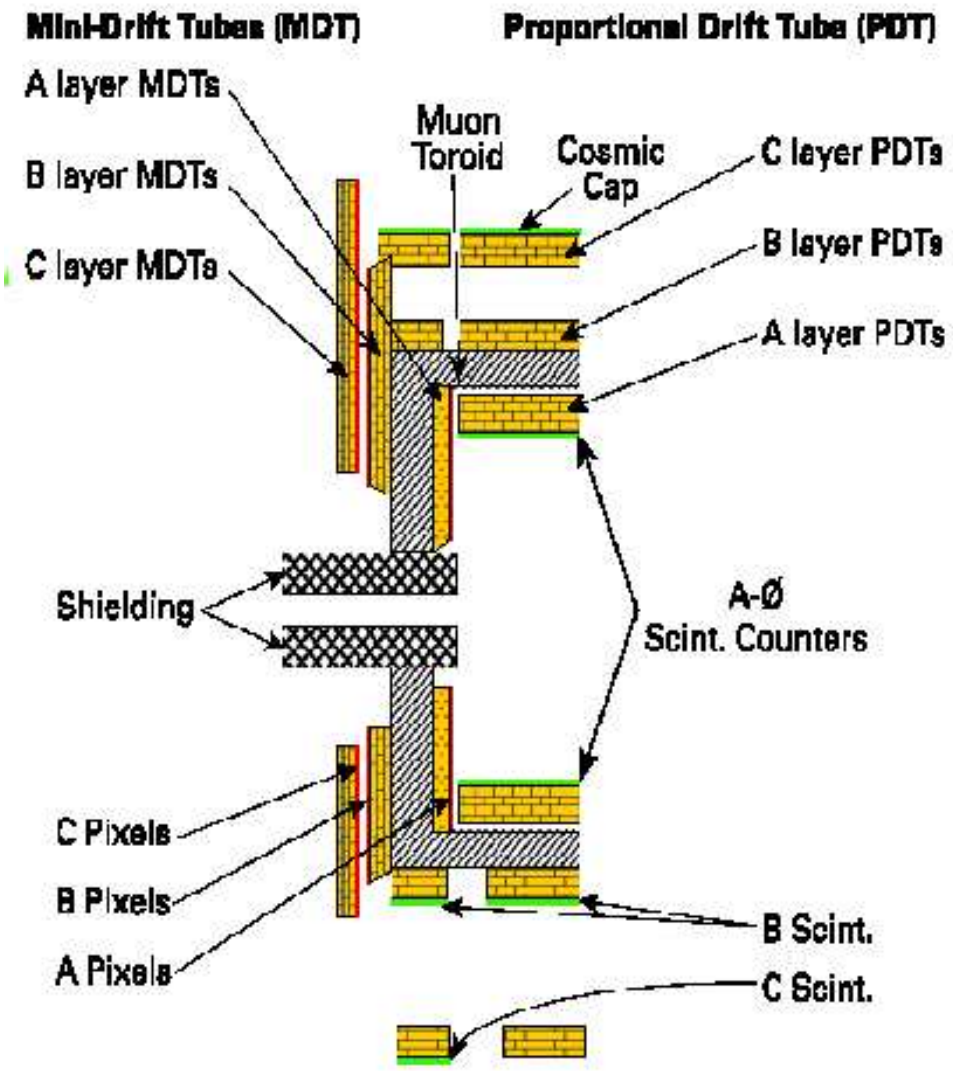

Figure 3.9: Illustration of the DØ muon subdetector components.

four decks of drift tubes and the B and C-layers have three decks each. Each drift tube consists of 8 cells, each with a $1 \times 1\ cm^2$ cross section with a 50 μm anode wire in the center. The tubes are made from aluminum extrusion combs with stainless steel cover foil and contained in plastic sleeves with a length up to 6 m. Wires in the cells are oriented parallel to the magnetic field of the forward toroid magnet. The sleeves of tubes are mounted on an aluminum support structure which also provides mechanical support for the infrastructure. A plane of MDT counters is shown in Fig. 3.10.

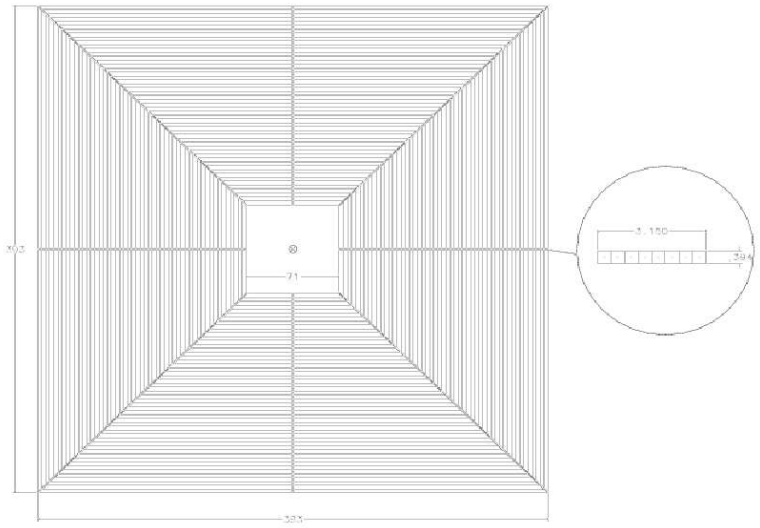

Figure 3.10: DØ forward muon mini-drift tube (MDT) plane.

The MDT's use a gas mixture composed of 90% CF_4 and 10% CH_4,with a maximum drift time of about 60 ns. The gas is non-flammable and fast. The momentum resolution of MDTs is limited by multiple Coulomb scattering in the iron toroid and the hit resolution of the detector. In addition, the MDT electronics uses a 18.8 ns time bin of digitization card for the drift time measurement. Taking into account the coordinate resolution, the magnetic field of the toroid and multiple scattering, the

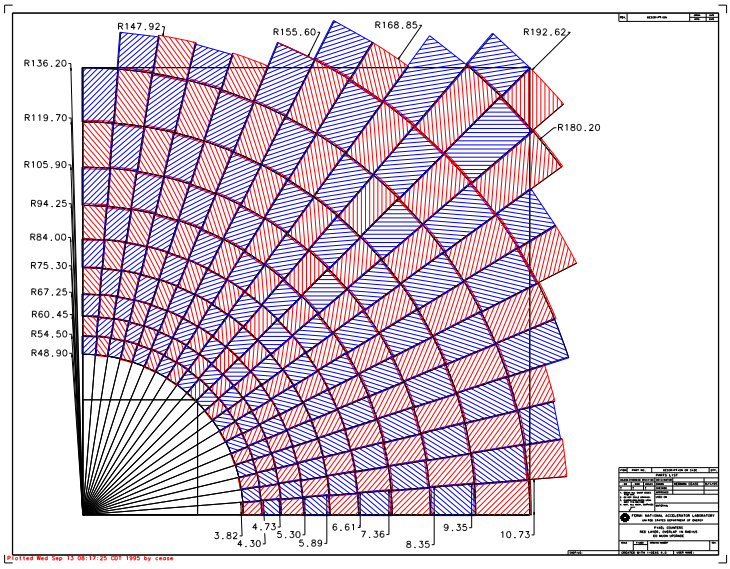

Figure 3.11: Two DØ forward muon pixel octants.

momentum resolution of MDT is roughly $\sigma(p_T)/p_T = 0.2$ for low momentum muons. Importantly, it is on par with the resolution of DØ's central tracker in the forward region where the full coverage of the fiber tracker has ended.

The Scintillation Counters

The Scintillation Counters are used to tag the bunch crossing from which the muons originate for the drift chambers and to reject background particles which leave hits at times other than expected from a muon originating at the interaction point.

In the central region ($|\eta| \leq 1.0$), the A-layer contains 630 "A-phi" scintillator counters. Located between the central calorimeter and the central A-layer PDTs, they provide a ϕ measurement matching high and low p_T triggers with the central

tracking system and reject out-of-time backgrounds.

The counters are approximately 33" long and their widths vary from 10" to 17" in order to maintain a constant segmentation. They divide the A layer into rows spanning 4.5° in ϕ. Each row contains 9 counters and has a slight overlap with a neighboring row as to minimize the cracks between counters. The counters span only 93% of the azimuthal angle because of a gap where the calorimeter is supported by the detector platform. The scintillators are made from 1/2 inch thick Bicron 404a and light collection is accomplished with Bicron G2 waveshifter fibers. The fibers collect and transmit the light to a single photomultiplier tube (PMT). The counters have a time resolution of $\sigma = 4$ ns and are capable of discriminating between muons produced in the collisions and the background originating at or near the exit of the calorimeter, which arrives about 14 ns later than a muon.

Outside of the muon toroid magnet, 240 "Cosmic Cap" C-layer scintillation counters were deployed late in Run I and are described in detail in [39]. They cover the top and sides of the central region with 12 divisions in ϕ and 20 divisions in z and provide a fast trigger to tag the crossing for hits in the B and C layers. These counters are between 81.5 and 113 inches long and 25 inches wide. Eight of them are mounted on the outside of each C-layer PDT on the top and sides of the central muon detector. At the bottom of the detector, the three layer coverage is broken up because of the support structure for the central platform and toroid magnets. The bottom of the central region is covered by the 116 new "Cosmic Bottom" counters arrayed on bottom C-layer and B-layer PDTs: 40 counters located on the B-layer PDTs underneath the central muon toroid; 36 counters located underneath the north and south forward toroids and 40 counters located underneath the north and south ends of the platform.

In the forward region ($1.0 \leq |\eta| \leq 2.0$), there are three layers comprising a total of

$\sim$ 4600 pixel scintillation counters [38] with a segmentation of $0.1 \times 4.5^\circ$ in $\Delta\eta \times \Delta\phi$. Their purpose is mainly for muon triggering. The pixel counters are trapezoidal in shape and made from 0.5" thick Bicron scintillator with wavelength shifting bars. The counters are grouped into octants of $\sim$96 counters each to match the MDT arrays. The octants provide mechanical support for the counters and their infrastructure. They are mounted directly onto the A- and B-layer sides of the forward toroid magnets and onto the inside face of the C-layer support frame. Two octants are shown in Fig. 3.11.

Both of the central and forward scintillation counters have an LED pulser calibration system. The system serves to quickly find dead PMTs, monitor PMT gains which most strongly affect trigger timing, track timing and threshold changes. It provides a clocked, timed, amplitude-controlled photon pulse. Each PMT is connected by a light-shielded optical fiber to a light-tight box which houses bundles of LED's glued into a clear acrylic block. A single box may provide the photon pulse for up to 100 PMT's. The stability of the photon pulse is monitored with a light-sensitive diode housed in the clear block.

3.3 DØ Trigger and Data Acquisition

The proton anti-proton collision rate at the Tevatron is 1.7 MHz, which is orders of magnitude higher than events can be readout and stored. The DØ Trigger and Data Acquisition System (DAQ) [40] [35] are used to select and record interesting physics events for further analysis.

The trigger system consists of two hardware (L1 and L2) and one software-based (L3) trigger levels. Additionally there is a scintillator hodoscope trigger sensitive to all inelastic $p\bar{p}$ collisions used mainly for luminosity measurements. The Level 1 (L1) and Level 2 (L2) provide fast decisions based on fast sums of the tracking, calorimetry

and muon detectors. Level 1 is capable of handling a maximum 7 MHz input rate and has an accept rate of 5 – 10 kHz. The Level 3 (L3) is a software filter with partial event reconstruction on computer farm nodes. The typical L1, L2, L3 trigger rates are 1.4 kHz, 800 Hz and 50 Hz respectively.

3.3.1 The Luminosity Monitor

The luminosity monitor registers the presence of inelastic collisions and provides diagnostic information regarding accelerator performance and identifying beam crossings with multiple interactions. It uses two hodoscopes of scintillation counters located on the front faces of the end calorimeters and the pseudo-rapidity coverage is $2.7 \leq |\eta| \leq 4.4$. In addition to identifying inelastic collisions, it also provides information on the z-coordinate of the primary vertex which is determined from the difference in arrival time for particles hitting the two counters.

3.3.2 Level 1

The L1 trigger provides a deadtimeless 4.2 μs trigger decision. Fig. 3.12 shows the structure of the Level 1 and Level 2 triggers. The trigger uses information from the calorimeter, the central fiber and preshower detectors, the forward preshower and the muon scintillators and drift chambers. The fiber tracker and muon systems provide muon triggering in the region $|\eta| < 2.0$. The calorimeter, fiber tracker, and preshower detectors provide electron triggering for $|\eta| < 2.5$.

All L1 triggers are pipelined and buffered to ensure the deadtimeless operation. The L1 trigger detectors examine each event and report their findings to the L1 Framework (L1FW). Each front-end digitizing crate includes sufficient memory to retain (pipeline) data from 32 crossings. The L1FW uses a series of field programmable get

arrays (FPGAs) and supports 128 unique L1 triggers bits, which are pre-programmed to require a specific combination of trigger terms. If one of the 128 bits is satisfied, the L1FW issues an accept and event data is digitized and moved from the pipeline into a series of 16-event buffers to await a L2 trigger decision.

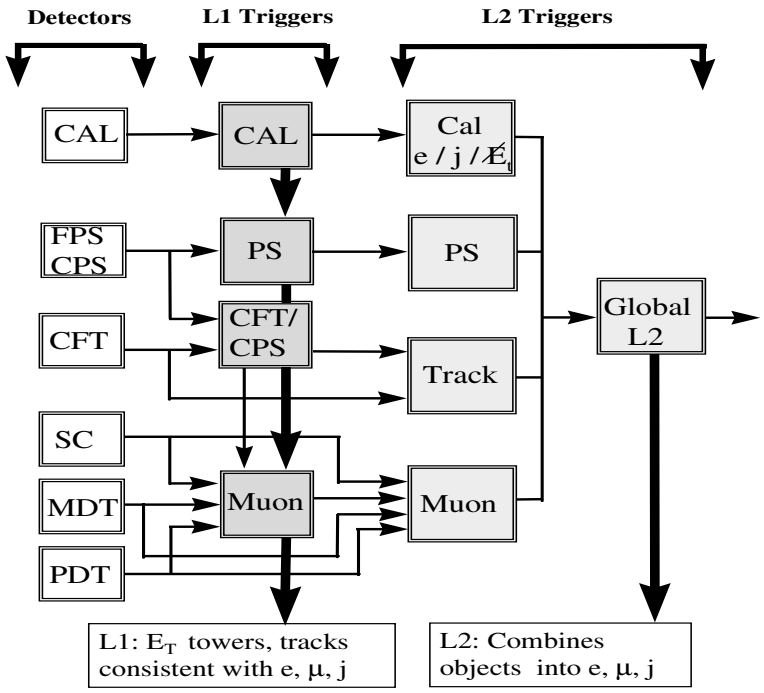

Figure 3.12: The structure of the Level 1 and Level 2 triggers.

3.3.3 Level 2

The L2 trigger shown in Fig. 3.12, comprises hardware engines associated with specific detectors and a single global processor. It tests for correlations between L1 triggers found in the event and reduces the L1 accept rate by a factor of ten within 100 μs.

There are two distinct L2 stages: the preprocessor stage and global processor stage. In the preprocessor stage, each detector system separately builds a list of trigger information. There are individual preprocessors for the calorimeter, CFT, muon tracker, and the preshower detectors. The L2 trigger information for each detector is transformed into physical objects such as energy clusters or tracks and this preprocessor information is transmitted into the global processor. The global processor uses the preprocessor information to provide trigger decisions which are based upon correlations among multiple detector systems within 75 μs. A L2 framework (L2FW), utilizing the same FPGA logic as the L1 Framework coordinates the operation of L2 and reports trigger decisions to L3. Upon receipt of a L2 accept from the global processor, L3 initializes the detector readout and moves the event data into eight transfer buffers.

3.3.4 Level 3 and Data Acquisition

The L3 trigger reconstructs events on a farm of processors for a final accept rate of 50Hz and functions as the Data Acquisition System (DAQ). Figure 3.13 shows the Run II data acquisition path. Once a L2 accept occurs, digitized data is loaded from the L3 transfer buffers to a VME Receiver Collector (VRC) by the VME Buffer Drivers (VBDs) through one of 16 high speed data pathways. The VRC sends the data to the L3 farm Segment Controllers (SCs) through the fiber path. Also notified at the same time, the Event Tag Generator (ETG) uses trigger bits to assign an event to a specific event class. A SC accepts the tag and assigns the event to a specific L3 node in the attached segment. Each SC examines passing data blocks and moves the data blocks belonging to a single event into one of the 114 L3 processor nodes. Software filtering in the L3 nodes is accomplished by a series of software tools. These tools have access to all event data to search for electron, muon, jet candidates and

other physics objects. Any event meeting filter requirements will be transferred to tape storage for offline reconstruction.

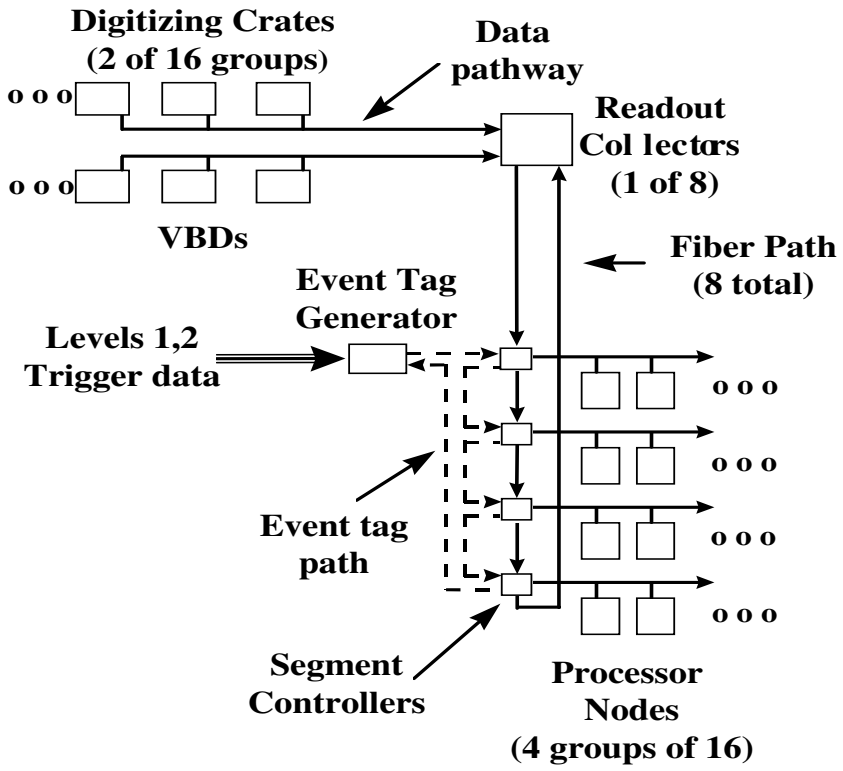

Figure 3.13: Level 3 framework.

3.3.5 DAQ Shifts

A priori, the DØ experiment collects data 24 hours a day, 7 days per week. All members of the collaboration are obliged to take at least 18 8-hour shifts per year. The author started as an SMT shifter, and later was trained as a DAQ shifter. He has taken over 40 DAQ shifts since December 2003. DAQ shifts are considered one of the most demanding and important at DØ. The primary responsibilities of a shifter include: securing a smooth data taking process for both physics and various calibration runs, downloading triggers with prescales selected by the captain, monitoring performance of all sub-detector crates and of the triggers. A DAQ shifter executes the *"begin of store"*, *"end of store"*, *"begin of run"*, and *"end of run"* commands. In addition he/she has to do routine safety checks of the electronic crates in the moving counting houses and record all the ongoing activities into a logbook. A shifter performance is evaluated by the amount of transition time used between runs and at the beginning of a store. The tools at the shifter's disposal are described next.

There are many online GUI (Graphic User Interface) programs through which the shifter controls the data taking. The most important one is called a "taker". Using the "taker", the shifter starts and ends a run, configures electronic crates and downloads a required version of the trigger list, selected according to the initial Tevatron luminosity before the run start. The shifter can also check the trigger rates for each individual trigger term at all trigger levels.

There are three main online monitor GUIs that help a shifter to monitor the data flow:

- "CoorMon": the run Coordinator Monitor, which coordinates all the sub-detector and trigger crates, the Level 3 farm nodes, and database and monitor server connections through the network. All the crates configured in a given

run are also shown in this program;

- "ÜMon": Über Monitor, which monitors the sub-detector and trigger crates at the L1 and L2 levels. It shows the Level 1 and Level 2 input and output rates. It is the shifter's responsibility to check that these rates are within acceptable range;

- "FüMon": the Farm nodes Monitor, which monitors the performance of all the Level 3 farm nodes.

During the data taking, once a problem occurs, such as a connection is lost, or some crates get front-end busy (which indicates that either an electronic board or a farmnode got stuck), the corresponding block in a monitor GUIs will turn to a red color and a vocal warning will be issued. To save beam time, the shifter has to respond quickly. He/she has to either identify and solve the problem himself/herself, or inform a relevant sub-detector shifter and determine when to call for help from a given system expert on duty. In addition to the monitors listed above, the alarm and luminosity monitor GUIs have to be checked on a regular basis.

Chapter 4

Alignment and Calibration Database for the Muon Detector

This chapter describes the service work the author has done for the DØ muon detector: (i) the alignment of the muon subsystems, and (ii) the design and implementation of the on-line and off-line calibration databases. The purpose of the alignment is to locate the position of the muon chambers relative to each other and to the DØ global coordinate system. The databases are used to store the various calibration constants for the muon electronics. Many of these constants are downloaded to the Front End Boards at the beginning of each run. The off-line databases are intended for the data reprocessing with improved constants.

4.1 Alignment

Maintaining good knowledge of the locations of the DØ sub-detectors is essential. The alignment problem for muon detector is compounded by the fact that the DØ detector is to good approximation hermetic, so that the inner detectors are hidden from external view and by the fact that major pieces (Central Field (CF) and End Field (EF) toroid magnets) are moved for access to the inner detectors and thus can

return to different locations. Most of this work was done in 2001 and 2002 with regular updates and the verification of the constants with improved precision in the following years.

As discussed in Section 3, the muon detector consist of three subsystems: (i) Wide Angle Muon Spectrometer (WAMUS) proportional drift tubes (PDTs) and attached scintillator counters, (ii) Forward Angle Muon Spectrometer (FAMUS) Mini Drift Tubes (MDTs) and (iii) FAMUS scintillator pixel counters. The author was co-responsible for the alignment of the PDTs and MDTs. The project was done in collaboration with A. Zieminski and A. Ito from Fermilab. The pixel alignment was carried out by the Dubna and Protvino groups. In addition, the positions of the so called A-phi scintillator counters, located around the inner most part of the WAMUS detector, were taken directly from the survey data.

The layout of the PDT and MDT chambers are shown in Figure 4.1.

The alignment of PDTs was done separately for each of the 94 chambers, whereas the MDTs were aligned by octants (24 in total). The alignment of PDTs was by far the more demanding task. The difficulties arose due to:

- several phases of survey using different coordinate systems;
- 16 different types of PDTs;
- numerous offset constants for wire positions;
- DØ geometry software for reconstruction combining a given PDT and its associated scintillators into one geometrical object;
- large dimensions of the PDTs with the possibility of the wire sagging in the middle; and

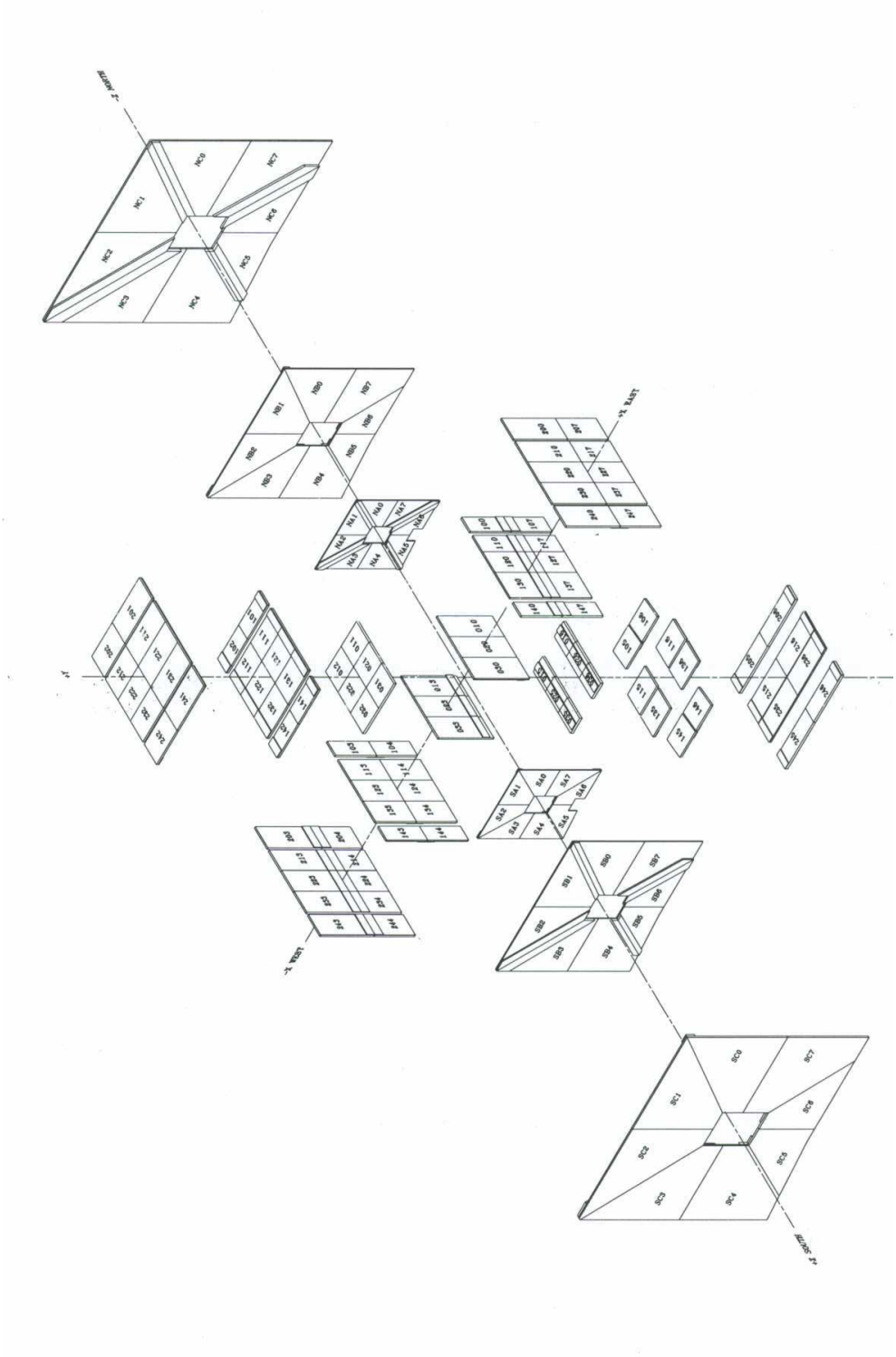

Figure 4.1: The layout of PDT and MDT chambers.

- verification process obscured by competing effects resulting from inaccuracies in the drift time starting point (T0) and the time-to-distance parametrization. The latter turned out to be very sensitive to the water admixture of the purified gas flowing in the A-layer PDTs, showing up to 6% seasonal variation [15].

The verification of the alignment has been done primarily by A. Zieminski with important contributions from J. Butler (Boston University) and G. Hesketh (Northeastern). Positions of the A-layer chambers (MDTs and PDTs) were verified using a "$\Delta drift$" variable, defined as a difference in positions of the A-layer local muon segment and that of the matching central track, extrapolated to the center of gravity of the segment, measured along the drift direction. The achieved precision is at the 1.0 mm level. Verification of the B and C alignment was done by comparing their relative positions and by studies of the local muon momentum resolution.

4.1.1 The Survey for PDTs

The survey of the muon chambers was done in three phases by the DØ survey group and the results were stored in the alignment database. Definitions of different Coordinate Systems used in the process can be found in Ref. [41]. The steps were as follows:

- Phase I : Measurement of positions of the reference holes and tooling balls in the Survey Local Coordinate System;

  The position of all PDT wires relative to these reference holes is known from the chamber design and construction technique. Figure 4.2 shows the geometry of a PDT cell. The center of the chamber can also be calculated from the positions of the reference holes. However, these reference holes are invisible once the

chamber is mounted on the detector. Therefore, on each chamber there are four visible 0.5" diameter tooling balls mounted near the corners of the chamber.

- Phase II: Measurement of the tooling ball positions relative to the EF and CF toroid magnets in the Survey Global Coordinate System;

  The 94 muon PDT chambers are mounted on different supports and can be divided into 3 groups: 58 chambers in the East-West mounted on the CF toroid magnets; 28 chambers in North-South mounted on the EF toroid magnets; 8 chambers mounted on the platform that will never be moved.

- Phase III: Measurement of the toroid magnet positions relative to the beam center. Every time the detector is closed, the chambers in the East-West and North-South groups can return to different positions and their locations need to be adjusted; and

- Phase IV: Rotation and shift of the global coordinate system (Phase III) to that of the central tracking.

4.1.2 Alignment Fitting Procedure

The alignment procedure involves the following steps:

1) The survey phase I results, modified for extra shifts provided by Al Ito, are used to determine the coordinates of the center of the chamber and relative positions of the wires and tooling balls. In addition, all coordinates are transformed from the Survey Local Coordinate System to the Physics Local Coordinate System (C.S.); The coordinate system transformations are summarized in Table 4.1. At this stage corrections are applied for the offsets used in the DØreco geometry to account for the

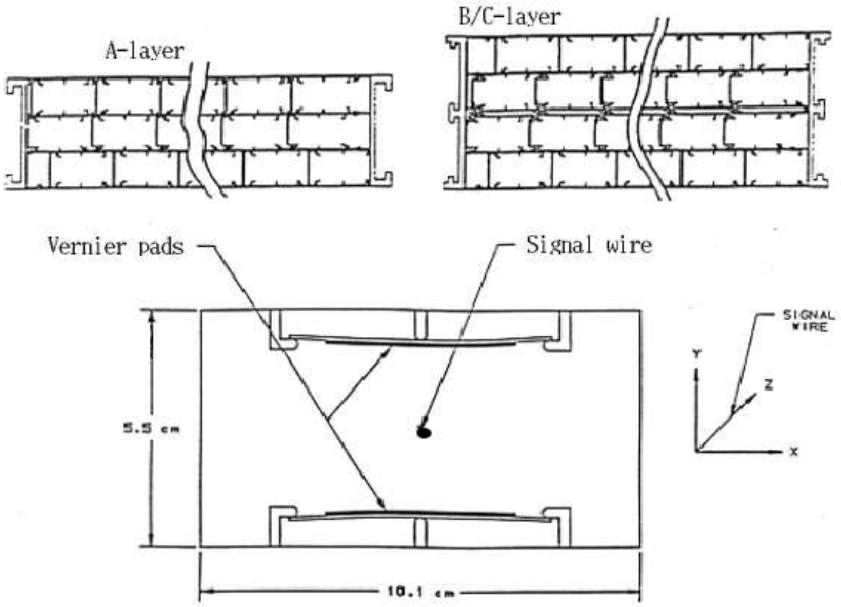

Figure 4.2: Geometry of a PDT cell.

scintillators attached to different sides of the chambers (top, bottom, or at one of the sides).

2) The survey phase II results for the tooling balls are transformed from the Survey Global C.S. to the Physics Global C.S. This involves both redefining the coordinate axes (see Table 4.1) and rotations and shifts between the Survey Global C.S. and Physics Global C.S. These small shifts and rotations (called the Survey Phase III results) have to be determined after each opening and closing of the detector. This has been done at least 5 times since February 2002.

3) The transformation parameters (3 components of the translation vector and 3 rotation Euler angles) from the Physics Local C.S. to the Physics Global C.S. are determined using a χ^2 fit of the transformed phase I data (step(1) here) to the phase III data (step(2) here). The standard Cernlib program Minuit [42] was used for the

minimization. After a best fit is obtained, we get the translations and rotations between the Physics Local and Global coordinate systems and also the position of the chamber center in the Physics Global coordinate system. The χ^2 is calculated assuming a 254 μm survey accuracy per coordinate. The actual accuracy is closer to 500-700 μm (combined for two survey measurements). There are 6 degrees of freedom per fit (3 coordinates * 4 tooling balls minus 6 fit parameters). Therefore, the expected average χ^2 per fit is 30-40, as observed in Figs. 4.3, 4.4 and 4.5.

4) The fit parameters are stored in a Run Control Parameter (RCP) file (*MuoBase-Geometry.rcp*) which describes the default muon detector geometry. A simplified version of the *MuoBaseGeometry.rcp* file, with the Euler rotation angles rounded up to 0, 90, 180 and 270 degrees is used for Monte Carlo. Originally, the RCP file was used directly by the DØ reconstruction program. Later, it has been decided to transform the muon and calorimeter detector coordinate system (Physics Global C.S.) into the coordinate system used by the central tracking. The Global Alignment group is responsible for this final step, that has lead to some confusion in the past, as illustrated in the next subsection.

The alignment procedures for the MDTs have been much simpler. The phase I data were determined from the blue prints and the phase II and III steps were combined in the survey. Our role was reduced to extracting the phase I coordinates, performing the fit and converting the results into the RCP format.

Phase I data		Phase II data	
Survey Local C.S.	Physics Local C.S.	Survey Global C.S.	Physics Global C.S.
x	Y	x	X
y	Z	y	$-Z$
z	X	z	Y

Table 4.1: Coordinate System transformations

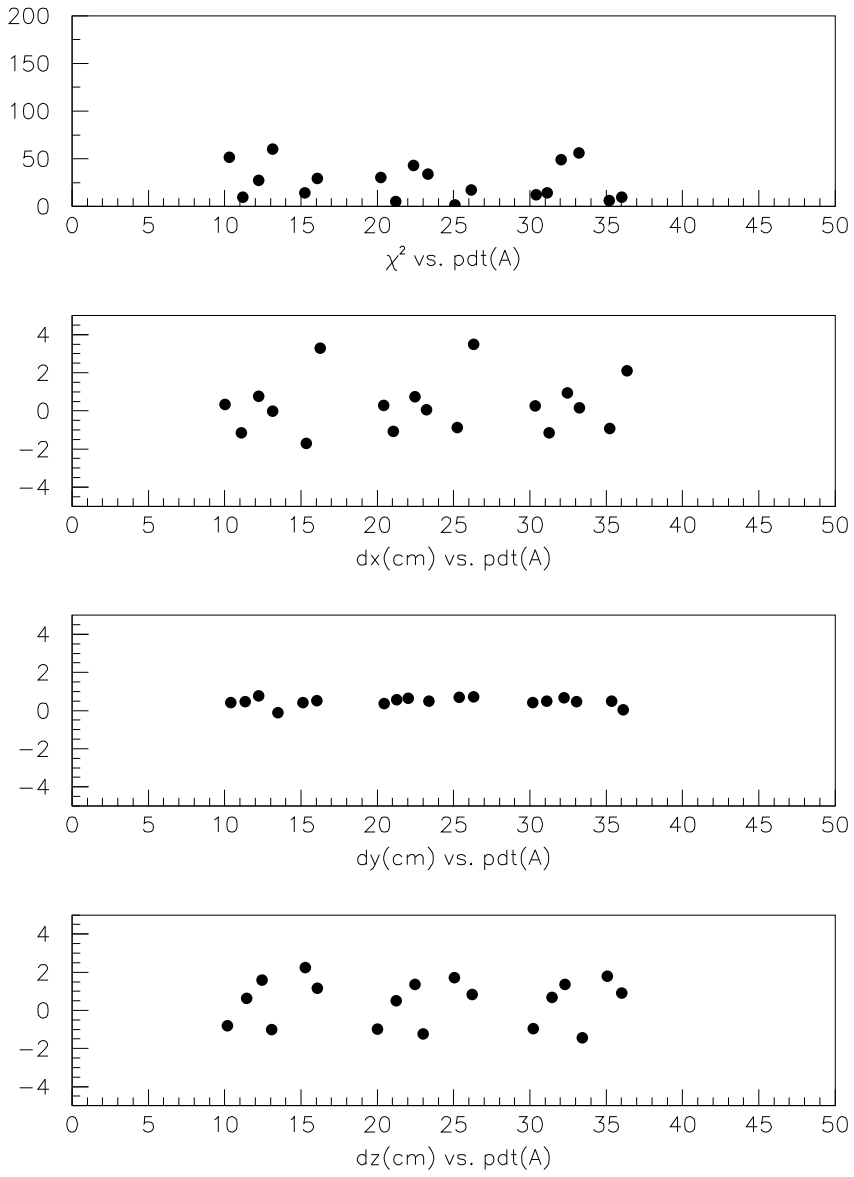

Figure 4.3: The fitted χ^2 and the differences between the fitted coordinates and their nominal values taken from the Run I alignment constants for the A layer chambers.

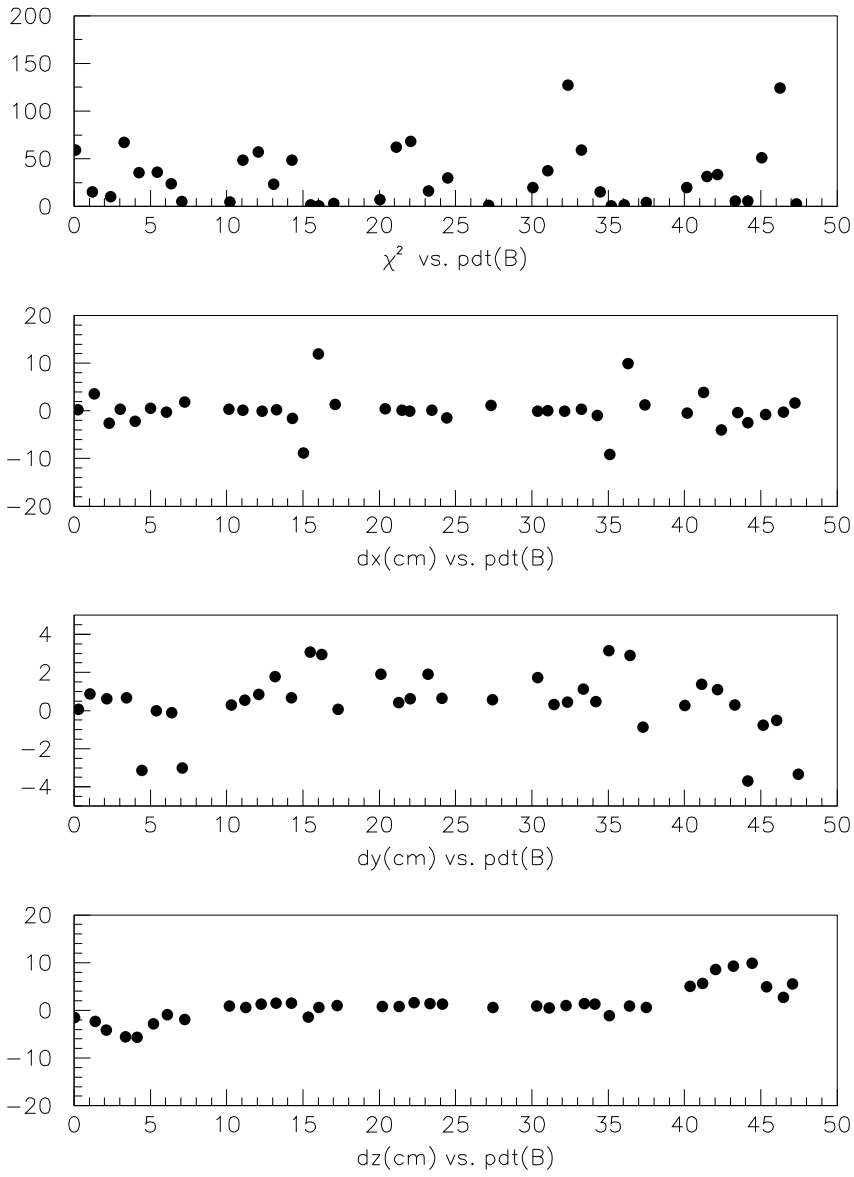

Figure 4.4: The fitted χ^2 and the differences between the fitted coordinates and their nominal values taken from the Run I alignment constants for the B layer chambers.

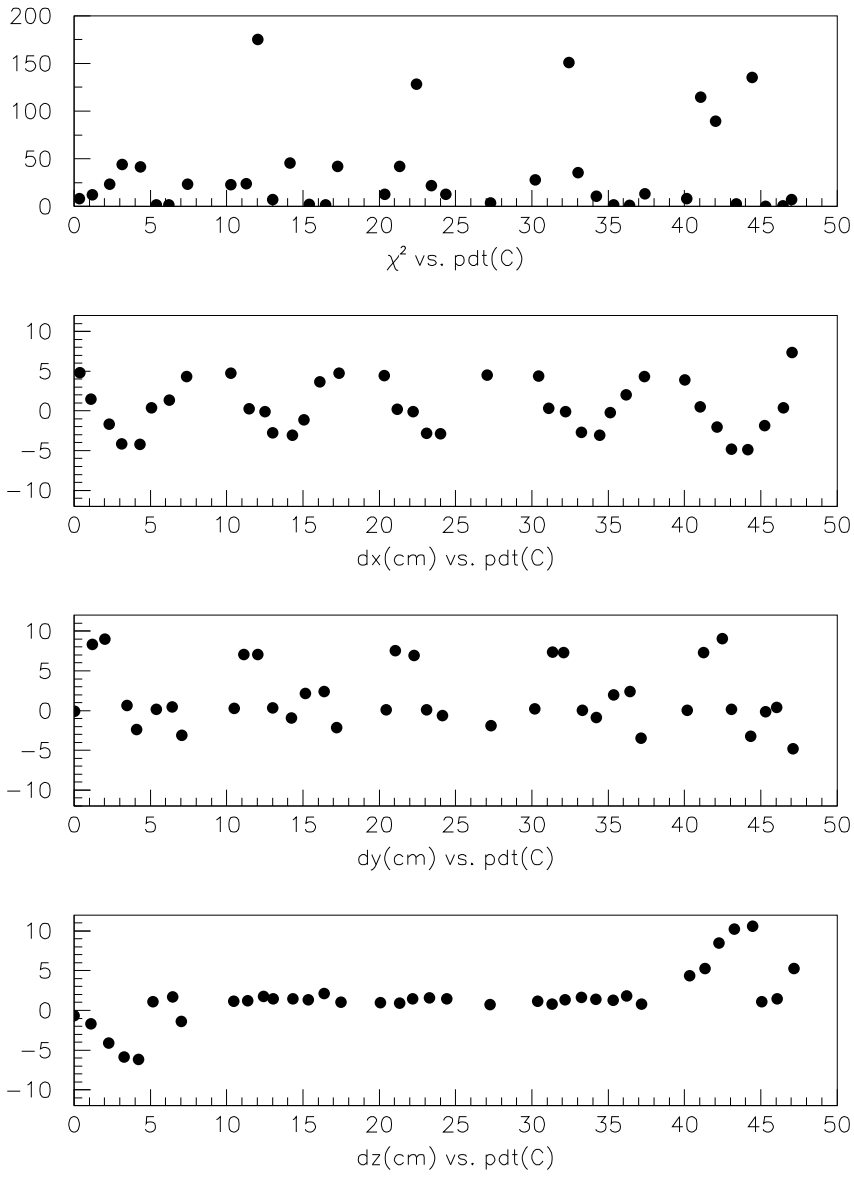

Figure 4.5: The fitted χ^2 and the differences between the fitted coordinates and their nominal values taken from the Run I alignment constants for the C layer chambers.

4.1.3 Alignment Results and Verifications

The fitted coordinates of the A,B,C layer PDT centers are compared to their nominal values, taken from the Run I alignment constants, in Figs. 4.3, 4.4 and 4.5 respectively. In this comparison, the z coordinate coincides with the proton beam direction and corresponds to the drift direction. The y-coordinate points upward and the x-coordinate completes the right-handed coordinate system. The observed shifts by several centimeters reflect offsets due to the attachment of scintillators. In addition, the barrel 0 and 4 PDTs are attached to the North and South truss that has been rotated compared to its Run I position, hence the observed behavior of the dz difference.

To verify the positions of the chambers after the alignment, several studies have been done. They are described in detail below.

(1) Studies of the $\Delta drift$ distributions for the A layer PDT and MDT chambers:

The first such analysis , performed at the beginning of 2003, using 4 million extracted dimuon events, revealed that the muon system had been, by mistake, rotated by 2.5 mrad with respect to the tracking system. Once our results became known, a typo was discovered in the rotation matrix used. For this analysis, we plotted average values of $\Delta drift$ (defined in Section 4.1) as a function of the octant number for several regions of muon pseudo-rapidity. We also reprocessed 100k events using corrected rotation matrix, in order to verify that the effect was gone. Examples of relevant plots for WAMUS and FAMUS are shown in Figs. 4.6, 4.7 ($|\eta| < 0.4$), and in Figs. 4.8, 4.9 ($|\eta| > 1.3$), respectively.

The actual $\Delta drift$ distributions, combined for all octants, before and after corrections, are shown in Fig. 4.10. The observed width of the corrected distributions is consistent with the expectations based on the known multiple scattering of muons in

the calorimeter for the selected momentum range (50 cm/p (in GeV/c)).

Our analysis of the $\Delta drift$ distributions was recently repeated, using a large statistics muon data set, by G. Hesketh [43]. He fully confirms our observations, but finds that there is still a 2-3 mm shift between the muon and central tracking systems along the z-direction, observed for all A-layer PDTs. This shift is being investigated.

(2) We have attempted to verify the relative alignment of pairs of the B and C layer PDTs by forming local muon segments, separately for each chamber in a pair, and projecting them into a plane half way between the layers. The difference in the z-coordinate, Δz, is sensitive to both the chamber translational misalignment and to uncertainties in the Euler rotational angles. It also is sensitive to shifts in the $T0$ variable and variations on the time-to-distance parameterization. The sensitivity to the Euler angle uncertainty makes this method not very rigorous for the barrel 0 and 4 PDTs, for which muon incident angles exceed 45 degrees.

As an example, the B/C layer Δz distributions for six octants of barrel 2 are shown in Fig. 4.11. All chambers are aligned to a better than 1 mm precision. The average values of the B/C layer Δz are collected in Table 4.2. The 5 mm shifts observed for some barrel 0 and 4 PDTs reflect uncertainties in the determination of the segment slopes. The typical deviations of the fitted Euler angles from the nominal values are less than 3-5 mrad. The slopes of the local muon segments are determined with uncertainties of 15 mrad (a BC segment slope is known to a precision better than 1 mrad). In Figs. 4.12 and 4.13, we show examples of Δz, $\Delta slope$ and the BC-segment χ^2 distributions for two pairs of PDTs: 123-223 and 103-203. The first example is typical for $\sim$85% of the WAMUS muons recorded in the barrel 1, 2 and 3 PDTs (incident angle less than 45 degrees). The χ^2 distributions for all these chambers indicate that the muon hit resolution, averaged over an internal position uncertainty and relative chamber alignment is approx. 800 μm. The second example, typical

for muons with large incident angles recorded in the WAMUS, indicates that the hit resolution for such muons drops to ∼1.5-2 mm.

(3) The ultimate test of the alignment is provided by comparisons of the local muon momentum resolution with the Monte Carlo expectations. The local momentum resolution is determined by comparing the variable q/p, measured using either local muon or central tracking information, where q is the charge of a track and p is its momentum. Such comparisons were carried out by J. Butler [44] in the summer of 2002 and spring 2003. He found that, whereas the FAMUS momentum resolution was consistent with Monte Carlo ($\sigma(p)/p \approx 45\%$ at $p = 100$ GeV/c), the observed WAMUS resolution was much worse. This discrepancy was due to a variety of factors: It was discovered by Luo and Zieminski [15] that the "pure" gas flowing in the A-layer PDTs is 10% slower than the "dirty" gas flowing in the B and C layer PDTs and two separate time-to-distance parametrizations were introduced. Once these and other [45] corrections were introduced, the WAMUS momentum resolution has improved to ≈ 45-50% at $p = 50$ GeV/c [46], compared with 40% expected from Monte Carlo. Several additional small mistakes in the chamber parameters have been discovered since. PDTs 115, 116, 135, and 136 have not been properly corrected for the Phase II to Phase III transformation. Three PDTs: 140, 202, 247 seem inefficient and have twice worse hit resolution than the average. In addition, for the last six months the detector has been run with obsolete values of $T0$. These mistakes have not affected the muon identification efficiency, but have had an adversary effect on the Level 3 trigger turn on curves. A muon task force, formed this summer, is due to revise the muon reconstruction software and introduce a better data quality monitoring program.

Barrel,Octant	7	0	1	2	3	4
0	+0.14	+0.09	+0.52	−0.15	+0.34	0.4-0.6
1	+0.06	+0.14	+0.00	−0.01	−0.35	−0.34
2	+0.08	+0.11	−0.17	+0.03	−0.03	+0.04
3	−0.27	+0.03	+0.09	+0.13	+0.24	+0.32
4	−0.27	+0.45	+1.20	−0.20	−0.66	−0.58

Table 4.2: The average values of the B/C layer Δz.

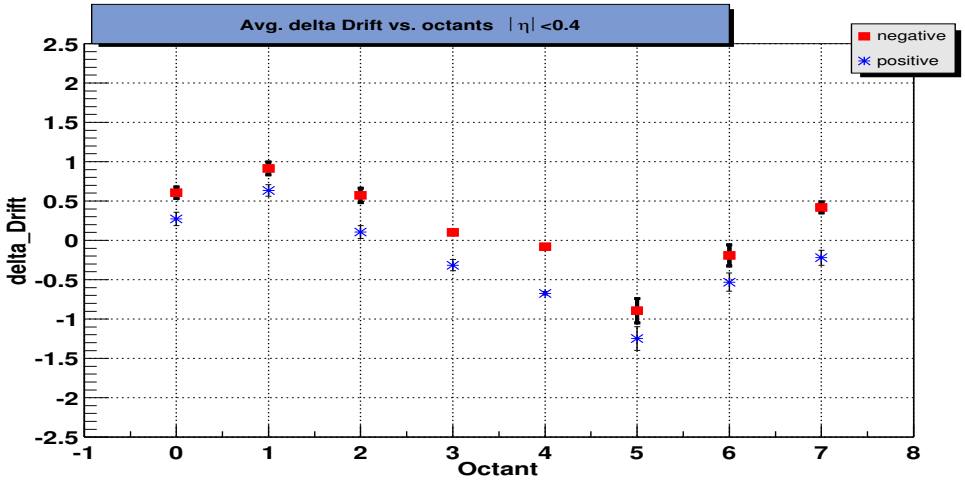

Figure 4.6: The uncorrected $\Delta drift$ vs. octant number for WAMUS ($|\eta| < 0.4$).

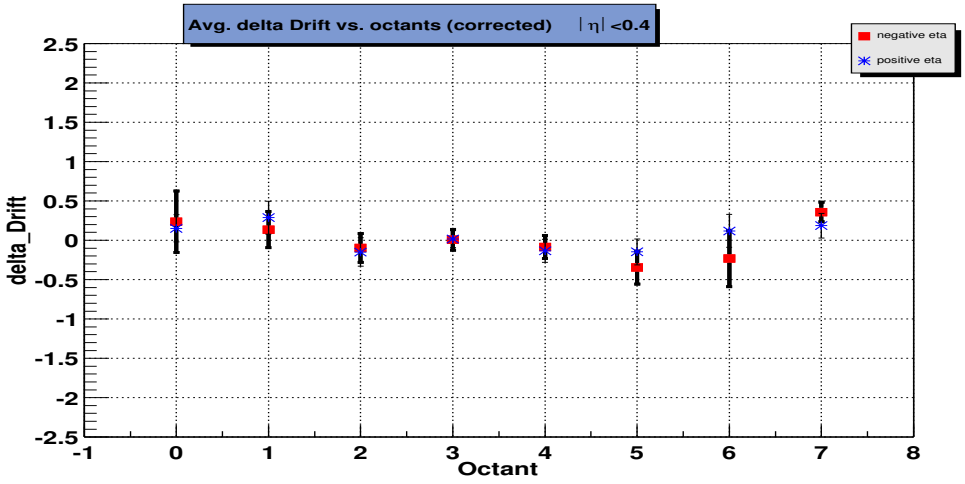

Figure 4.7: The corrected $\Delta drift$ vs. octant number for WAMUS ($|\eta| < 0.4$).

4.2 Calibration Databases

Periodic calibration of the sub-detector systems is one of the most important tasks during the data taking at DØ. The calibration constants for the DØ detector are stored in a central Oracle database [48] and organized separately for each sub-detector. These constants need to be accessed by the DØ offline reconstruction program (DØreco) running at the processor farm at Fermilab or at the processor farms at remote institutions. To reduce the number of concurrent accesses to the central database, DØ has implemented a three-tier architecture. It is comprised of the central Oracle Database, CORBA (Common Object Request Broker Architecture) servers and CORBA clients embedded in the DØ reconstruction program. It is a vendor-independent architecture and infrastructure that computer applications use to work together over networks. The database server and client functions like this: the client sends a request to the server and in turn the server queries the central database. The results of the query are returned by the server to the client and also

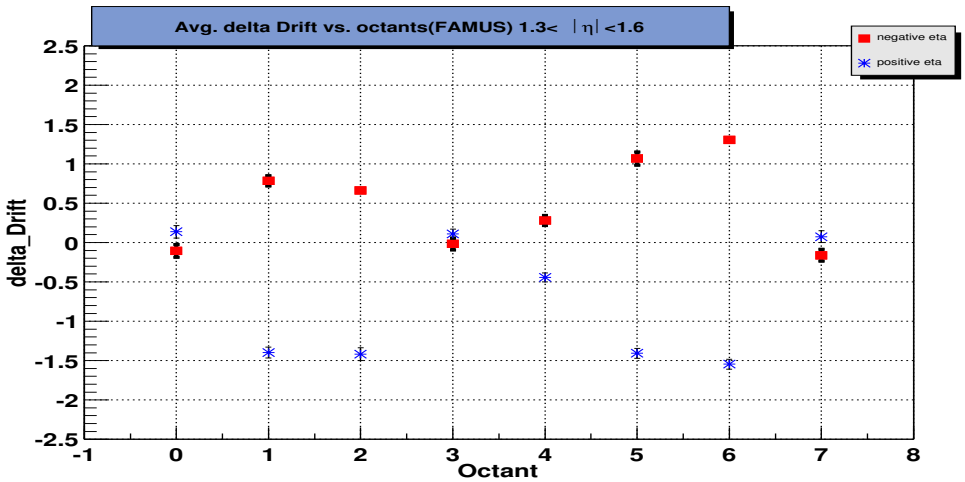

Figure 4.8: The uncorrected $\Delta drift$ vs. octant number for WAMUS ($|\eta| > 1.3$).

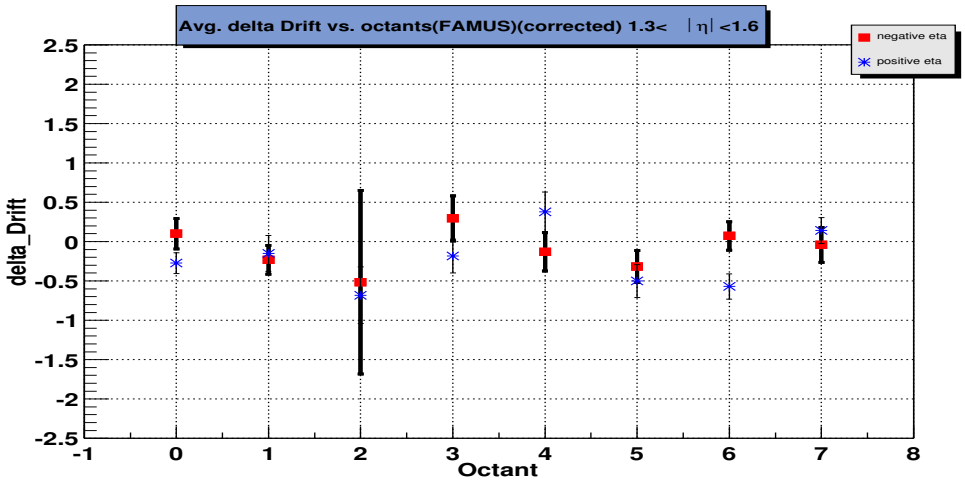

Figure 4.9: The corrected $\Delta drift$ vs. octant number for WAMUS ($|\eta| > 1.3$).

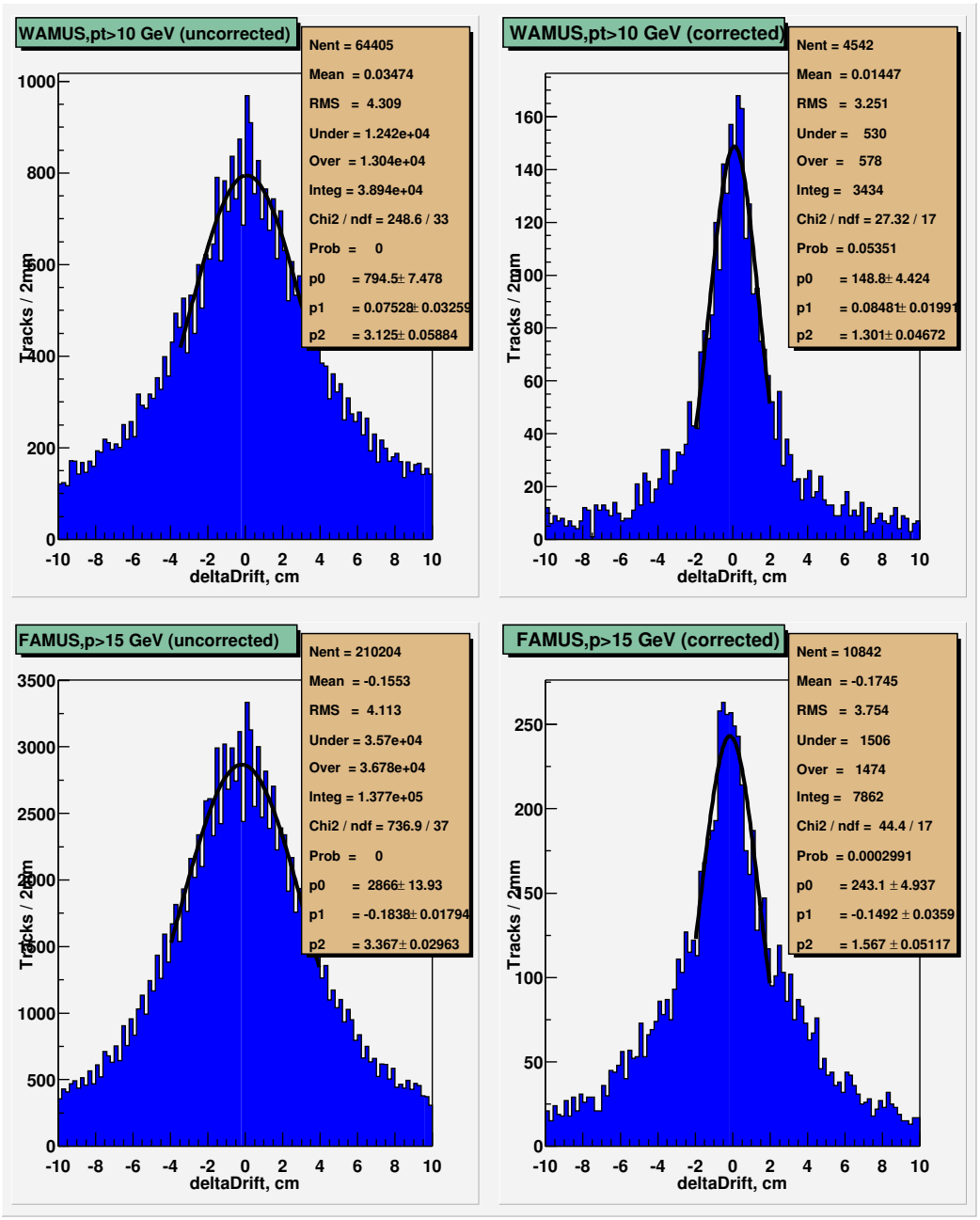

Figure 4.10: The actual $\Delta drift$ distributions (all octants combined, before and after the correction).

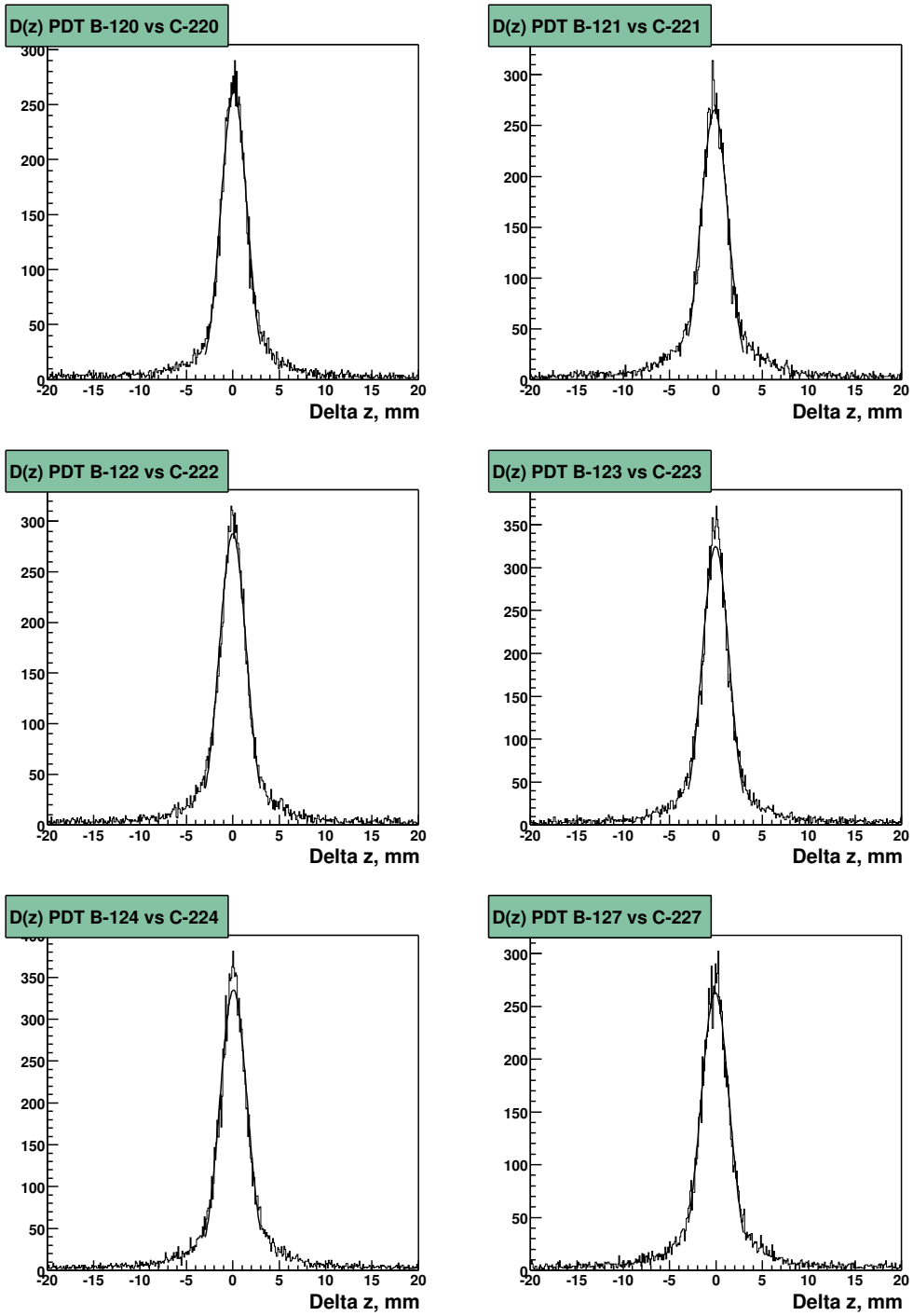

Figure 4.11: The B/C layer Δz distributions for six octants of barrel 2.

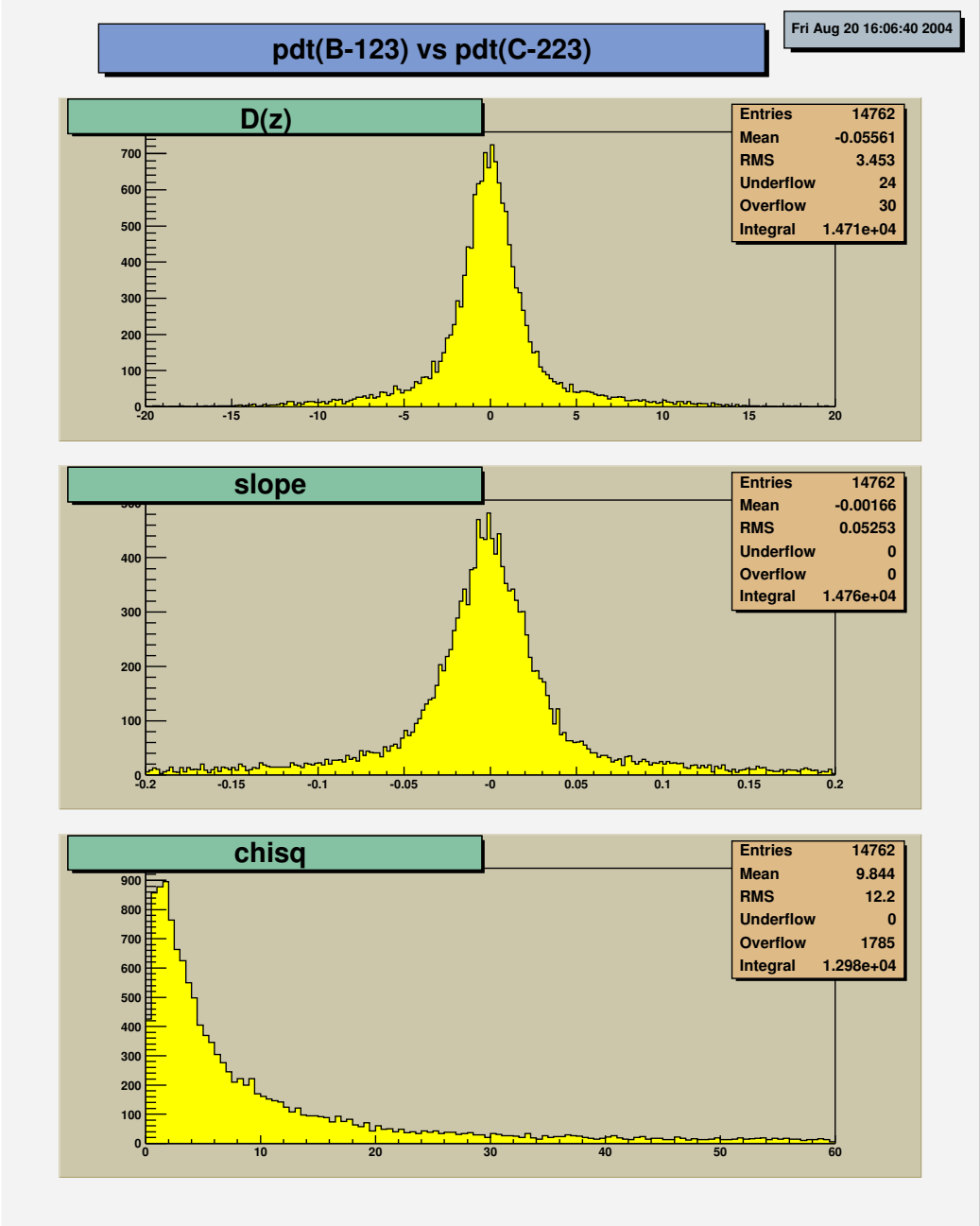

Figure 4.12: Δz (cm), Δ slope (radian) and the BC-segment χ^2 distributions for PDT pair 123-223.

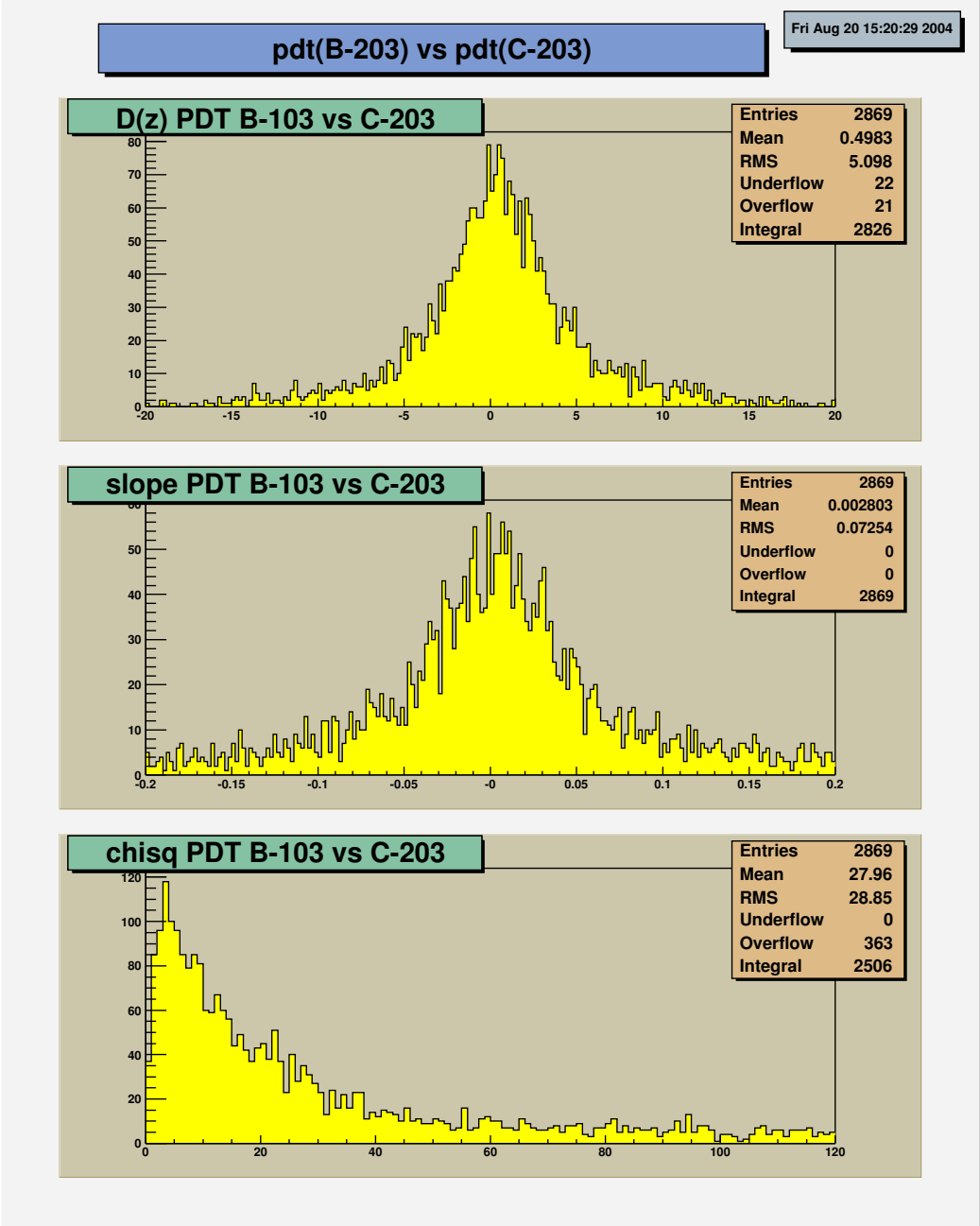

Figure 4.13: Δz (cm), Δ slope (radian) and the BC-segment χ^2 distributions for PDT pair 103-203.

are cached in memory or in a disk file for later fast access.

The author was responsible for designing the databases for the muon detector and their implementation. He was also responsible for populating and maintaining these databases through the end of 2002. In addition, he worked with A. Mayorov (Indiana, Protvino) and V. Lipayev (Protvino) on providing analysis and downloading tools. Later, he worked with R. Usha (Indiana) and A. Kutchner (Saclay) on coding and implementation of the Muon Calibrators in the DØreco software. This software was designed to access databases in D0reco, whenever data had to be reprocessed with improved constants. The muon calibrator was commissioned, but the access of databases turned out to be very CPU consuming, the databases were not available at remote sites. As the number of muon constants to be changed is limited (94 PDT $T0$), the required changes have been hardwired into the DØreco program.

4.2.1 Muon Calibration Databases

The muon systems take special data during the quiet time between the beam stores for calibration. These data are analyzed offline to determine the calibration constants [47]. We have chosen to define a set of separate offline and online databases for muon PDTs, MDTs and MSCs. The database designs for PDTs are shown in Figs. 4.14 and 4.15. The designs for MDTs and MSCs are shown in appendix C. The calibration constants such as T0s and gains are stored in both the online and offline databases. These tables are almost identical. The differences between the online and offline databases are: (i) the online databases also include tables that define parameters of the Front-End electronic Boards (FEB) such as thresholds, gates and masks. These parameters need to be downloaded to the FEBs for online data taking; (ii) the constants stored in the offline databases can be used by the DØreco program when reconstructing events. The detailed definitions of the constants can be found in [47].

All the muon databases are organized in similar hierarchical tree structures. As an example, the offline PDT database shown in Fig. 4.14 is discussed here. The top table called MUON-PDT-CALS, keeps track of the valid calibration sets by the valid run ranges (columns of the first-run and last-run). The other column such as DTDC-ID, is the primary key of the table MUON-PDT-DTDCSETS in the second row. It also keeps track of the valid 16 parameters of DTDC (the Drift Time to Distance Conversion) by the valid run ranges for all the PDT chambers in table MUON-PDT-DTDCS. All the other calibration constants are organized in the same way. The difference is that they are related to different hardware, either a single channel or a FEB and PDT module. The three tables at the bottom of Fig. 4.14, MUON-PDT-MODS, MUON-PDT-FEBS, MUON-PDT-CHNS, represents the hardware structure of the PDT. We populate the offline database constants using the script language Python. V. Lipayev (Protvino) provided a graphic interface to populate and download the constants to the online databases, as shown in Figs. 4.16 and 4.17. As one can also see from Fig. 4.14, the alignment constants described in previous section are also included in the offline databases.

4.2.2 Calibration Database Client and Server

A calibration database object is defined as a CORBA IDL (Interface Definition Language, which is used to define interfaces to objects on the network) object for transportability and also as a DØOM (DØ Object Model) object for persistency. The IDL definition is generated from the database table design in two steps: first the table definition is mapped to a dictionary file that includes the information about the columns in each table and their relations between tables. Then an IDL definition is generated from the dictionary file.

The server code is written in Python and is generated from the dictionary files

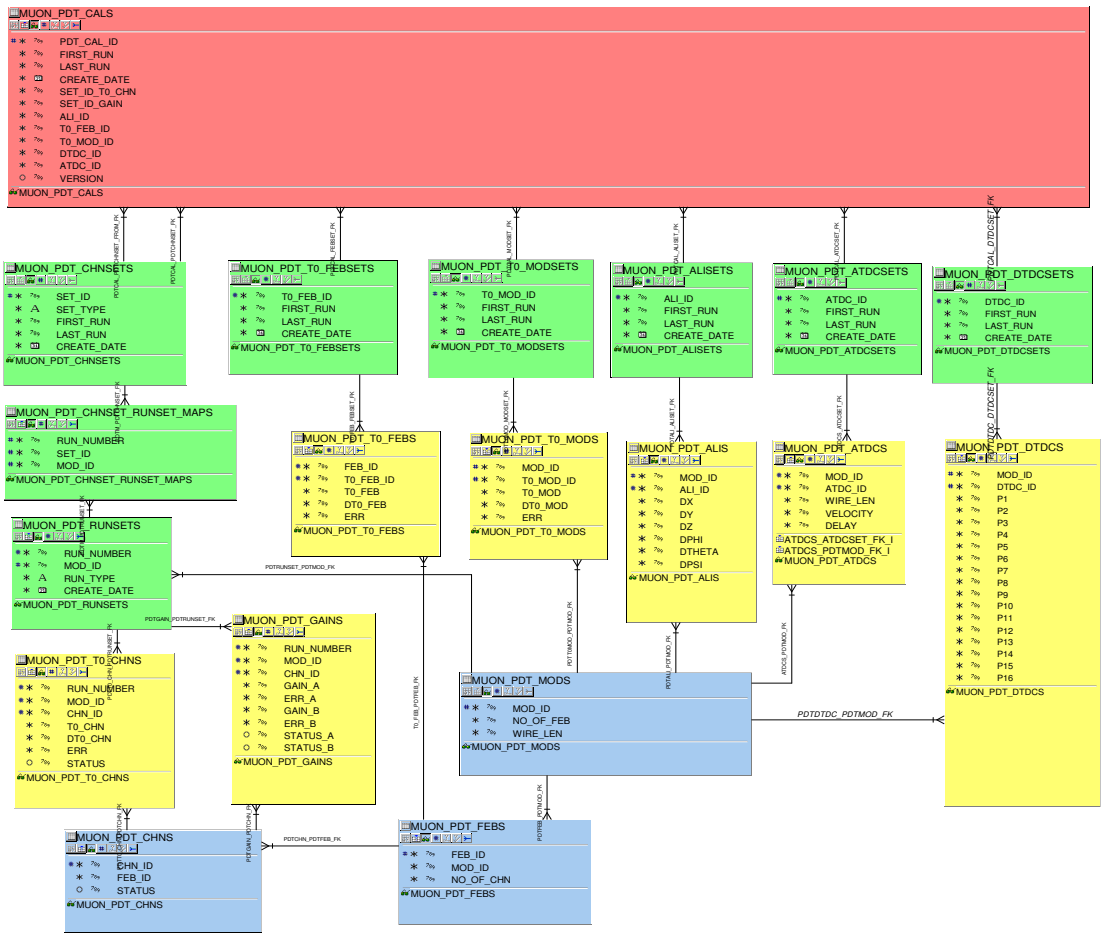

Figure 4.14: PDT Offline Database Design.

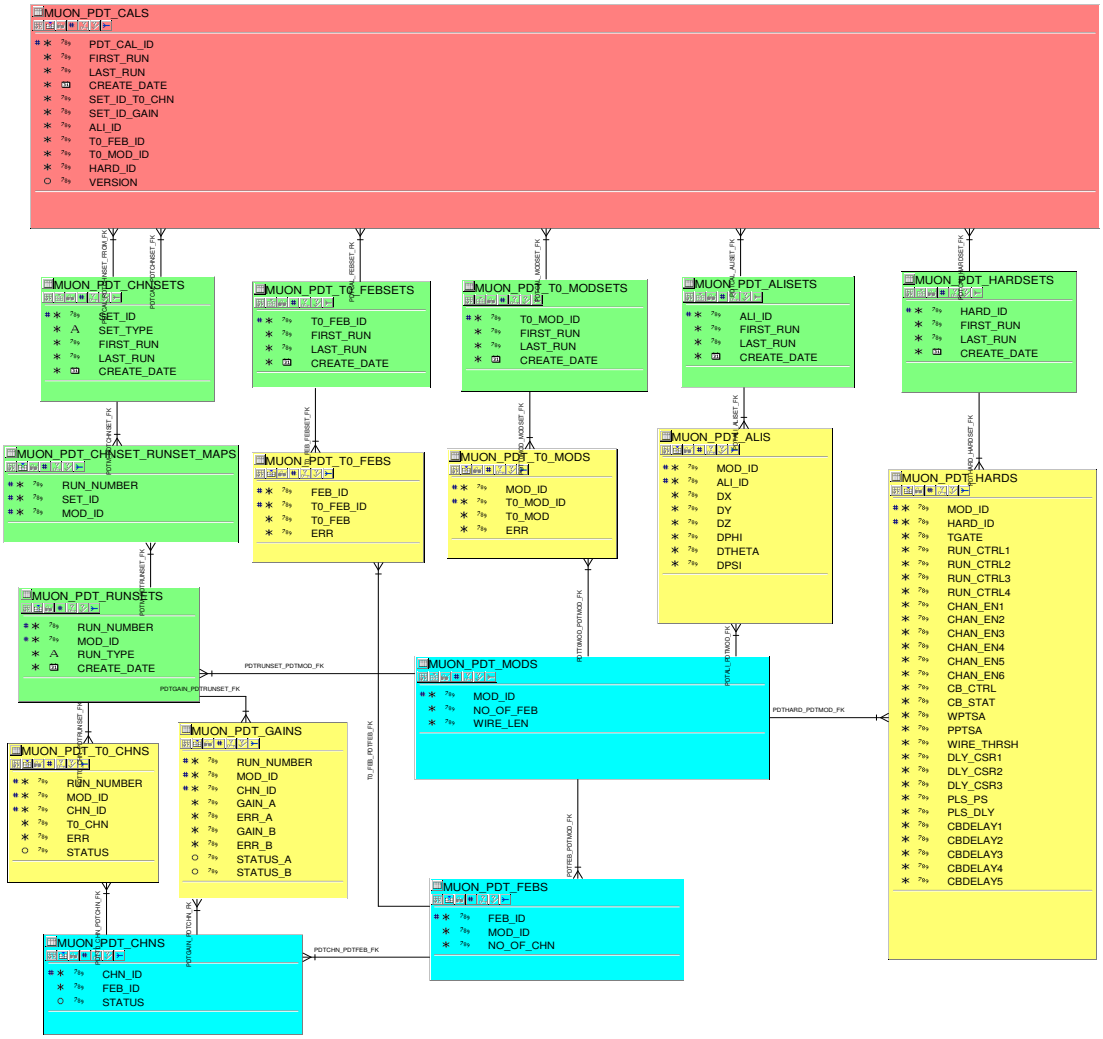

Figure 4.15: PDT Online Database Design.

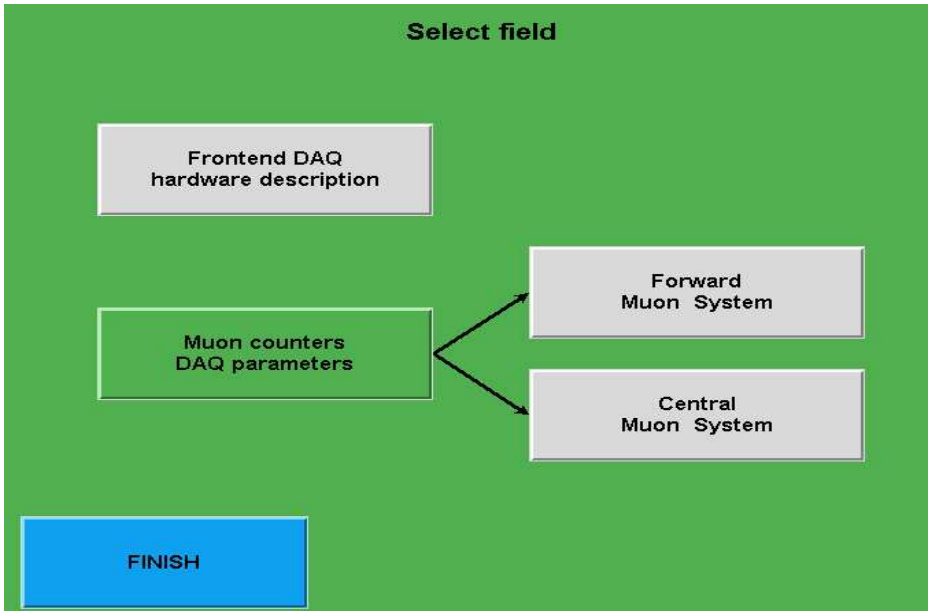

Figure 4.16: Muon database download GUI.

using a code generator. The client code embedded in DØreco is written in C^{++}. The header files for C^{++} classes that correspond to database tables are also generated from the dictionary files.

Figure 4.17: Muon database download GUI.

Chapter 5

Data Sample and Event Selection

5.1 Data Sample

This analysis is based on data collected by the DØ detector from June 2002 to September 2003 during the Tevatron Run II at $\sqrt{s}$ =1.96 TeV. The data were reconstructed by the program DØreco version p14.05. The dimuon events were skimmed by the B-physics group [49], requiring two muon objects with "$nseg > 0$" or "$nseg = -3$" and no trigger requirement (The "$nseg$" variable is defined in Section 5.2.2). The data used span runs from 160582 to 180956 and fire trigger lists (v8-v12). For this analysis, events are required to pass one of the two triggers: "2MU-A-L2M0" or "2MU-A-L2ETAPHI". These two triggers were introduced starting with run 160562. At least one of them remained unprescaled throughout the run range covered with the exception of runs 179759 through 180040, when the "2MU-A-L2ETAPHI" trigger had a prescale factor of 2. Events from these runs represent 0.5% of the data. Their detailed definition and other triggers presented in the data sample will be discussed next. After removing bad runs (783 runs due to muon and central tracking data quality and the runs 174207-174217 and 172359-173101 due to muon trigger malfunction) and bad luminosity blocks (less than 2% of the data), the integrated luminosity of the sample for reconstructed events was found to be 159.1 $\pm$ 10.3 pb^{-1}, assuming a

standard DØ 6.5% luminosity uncertainty.

5.1.1 Triggers

The triggers used for this analysis are muon-system-only triggers using only the first two levels of the DØ trigger system. They are described in detail below. The muon quality at the online trigger level are defined as follows:

- Tight: ≥ 2 wire hits in the A layer, ≥ 4 wire hits in the B and C layer, ≥ 1 scintillator hits in A and ≥ 1 scintillator hits in B or C layer, $\chi^2 \geq 0$;
- Medium: ≥ 3 wire hits in the A layer, ≥ 2 wire hits in the B or C layer. ≥ 1 scintillator hit in B or C layer. $\chi^2 \geq 0$; and
- Loose: ≥ 3 wire hits in the A layer, or ≥ 2 wire hits and ≥ 1 scintillator hit in A layer.

As mentioned above, this analysis is done for events triggered by the following two triggers:

- *2MU-A-L2M0*

  Level 1: two muons meeting tight scintillator requirements within the central or forward muon system.

  Level 2: at least one muon meeting medium requirements but no p_T or region requirement.

- *2MU-A-L2ETAPHI*

  Level 1: two muons meeting tight scintillator requirements within the central or forward muon system.

Level 2: at least one muon meeting medium requirements with (η,ϕ) separations of at least (3,6) in bins of 0.05 and 2.25° respectively.

In addition to these two dimuon triggers, we have found there is a significant contribution to our data sample from several other triggers. They are used to verify the relative trigger efficiencies and to estimate losses due to adding the Level 2 requirements as described in Chapter 7.

- Level 1 dimuon triggers: *mu2ptxatxx-fz* or *mu2ptxatxx*. We have verified that the *2MU-A-L2M0* or *2MU-A-L2ETAPHI* dimuon trigger combination was 96.5%, 97.3%, and 98.5% efficient with respect to the *mu2ptxatxx-fz* or *mu2ptxatxx* triggers in the three regions of dimuon rapidity studied (0-0.6, 0.6-1.2, 1.2-1.8), respectively.

- Single muon triggers *MUW-W-L2M0-2TRK3* (runs 170307-178720) and *MUW-L2M0-2TK3-MM* (starting at run 173516). As discussed later, the relative efficiency of our triggers with respect to these triggers, averaged over the Υ transverse momenta is (70±1)% in the dimuon rapidity range of less than 1.

- single muon triggers *MT3-L2M0-2TK3-MM* and *MT3-L2M0-MM5*, both activated since run 178721.

5.2 Muon Reconstruction and Identification

5.2.1 Muon Reconstruction

Muon objects are first reconstructed in the muon system from conversion of the raw hits and time information into three dimensional position information. After the

individual hits are found, track segments in each layer are formed by fitting associated muon hits into a straight line. The tracking is done separately for segments before and after the toroid magnet. The segments are then matched and the momentum is determined from the measurement of the bend of the track while passing through the muon toroid magnet. Finally, the local muon tracks are combined with the information from the central tracking system and the calorimeter to build a muon candidate.

5.2.2 Muon Identification

The offline muon identification [50] is based on a match between a charged particle detected in the central tracker and a reconstructed muon candidate in the muon system. Charged Particles are objects made by associating tracks detected in the SMT and CFT detectors. The reconstructed muon candidates are classified using two parameters: muon *type* and muon *quality*.

The *type* is given by the parameter *nseg*. A positive value of *nseg* indicates that the muon reconstructed in the local muon system was matched to a track in the central tracking system. A negative value of *nseg* tells that the local muon could not be matched to a central track. The absolute value $|nseg|$ 1, 2 or 3 indicates that the local muon is made up of A layer only hits, B or C layer only hits, or both A and B or C layers hits. In this analysis, events are required as $nseg = 3$. The detailed muon *types* are listed in Table 5.1.

The muon *quality* can be "Loose", "Medium" or "Tight". The standard quality criteria are listed for muon type $nseg = 3$:

"Tight":

- at least two A layer wire hits;

nseg	Muon Type	Central track Matching algorithm
3	Central track + local muon track (A and BC) layer	Muon to central if local muon track fit converged, otherwise central to muon;
2	Central track + BC only	central to muon
1	Central track + A only	central to muon
0	Central track + muon hit	central to muon
-1	A segment only	no match
-2	BC segment only	no match
-3	Local muon track(A + BC)	no match

Table 5.1: Definitions of muon types

- at least one A layer scintillator hit;
- at least three BC layer wire hits;
- at least one BC scintillator hit; and
- a converged local fit ($\chi^2 > 0$).

"Medium":

- at least two A layer wire hits;
- at least one A layer scintillator hit;
- at least two BC layer wire hits; and
- at least one BC scintillator hit (except for central muons with less than four BC wire hits).

A "Loose" muon is defined as a "Medium" muon but allowing one of the above tests to fail, with the A wire and scintillator requirement treated as one test and requiring always at least one scintillator hit.

5.2.3 Variables used in muon selection

The definitions of variables used in the analysis are defined as followings:

- *nseg* - muon type.
- *isCosmic* - if the muon is a cosmic candidate (timing cuts only).
- χ^2 - global track matching χ^2.
- *dca* - distance of closest approach of the track associated to the muon.
- *etTrkCone5* - a sum of transverse energies of charged tracks in a cone. of radius 0.5 (in $\eta - \phi$ space) around the muon.
- *etHalo* - a sum of the calorimeter transverse energies in an annulus cone of radii 0.1 and 0.5 around the muon.

5.3 Event Selection Criteria

In this analysis, the following event selection cuts are applied to muon candidates:

- $p_T^{\mu} > 3$ GeV/c;
- $|\eta^{\mu}| < 2.2$;
- Two opposite-charge "Loose" muons, with wire hits in all three layers;
- *nseg* = 3: each muon matched to a central track;
- the central track associated with a muon has at least one SMT hit;
- *isCosmic* = *false*: cosmic rejection; and

- Isolation cuts, as described below.

The Υ states are produced expectedly to be *isolated*. After trying several combinations of isolation variables, we have converged on a combination of two: *etTrkCone5* and *etHalo*.

The Υ isolation requirement are defined as:

- at least one muon satisfying either *etTrkCone5* < 1 GeV or *etHalo* < 1 GeV;
- *etTrkCone5* < 8 GeV for both muons.

Figure 5.1 shows the dimuon mass spectra with and without the isolation requirement. This isolation requirement reduces the background by 35% and the signal by less than 6%. Only a hint of a signal is seen for the non-isolated sample. Monte Carlo predicts that this isolation requirement is 100% efficient because the MC does not have a good simulation of noises in the calorimeter. The efficiency correction has to be derived from data. Similarly the requirement of at least one SMT hit is not well simulated in Monte Carlo. Therefore, to correct for these cuts, we performed mass fits without requirements on the central track quality and muon isolation.

A stronger requirement on the isolation of both muons removes a large fraction of the signal, a behavior that is not well modeled in the Monte Carlo. We will use a data sample with an enhanced upsilon signal (both muons with *etTrkCone5* < 1 GeV), shown in Fig. 5.2, only for the data - Monte Carlo comparison.

An additional requirement on the isolation of the upsilon candidate itself has a small effect on the dimuon mass spectra. A cut on *etTrkCone5*< 7 GeV, applied around the upsilon momentum vector, removes 3% of the background, and a comparable fraction of the signal. Therefore, this cut was not used.

We have investigated effects of imposing additional cuts on muon track parameters, such as local muon track χ^2, muon-track matching χ^2, central track χ^2, and the distance of the closest approach to the primary vertex (dca). We have found only a marginal improvement in the signal to background ratio. In particular, a $dca <$ 0.125 cm requirement on both muons would remove 2% of events without a loss to the signal. However, a stronger cut of $dca < 0.10$ cm removes 10% of the background events at the expense of 4% of the signal. These additional quality cuts are difficult to monitor with Monte Carlo and are not applied.

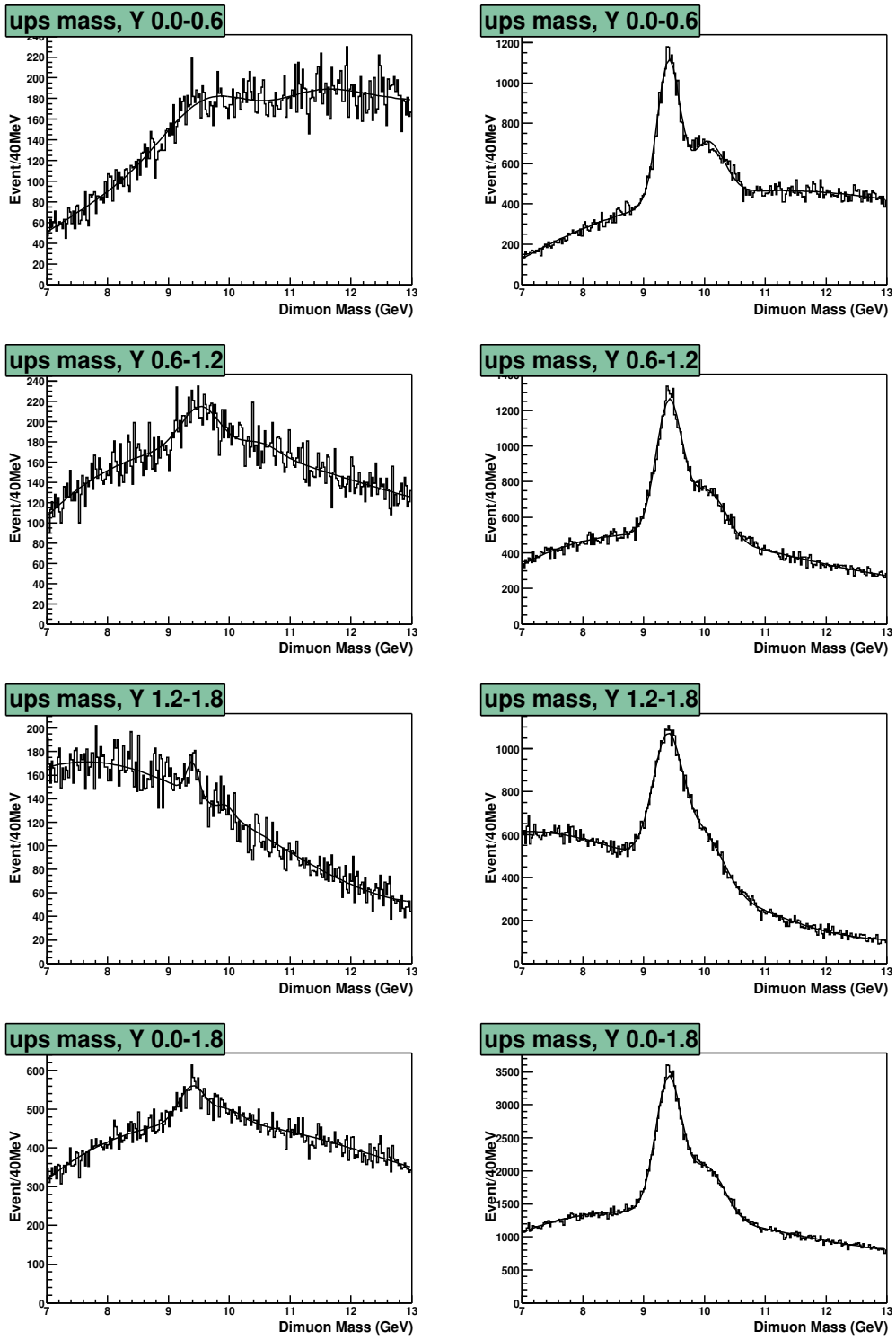

Figure 5.1: Dimuon mass spectra with the anti-isolation and isolation requirements.

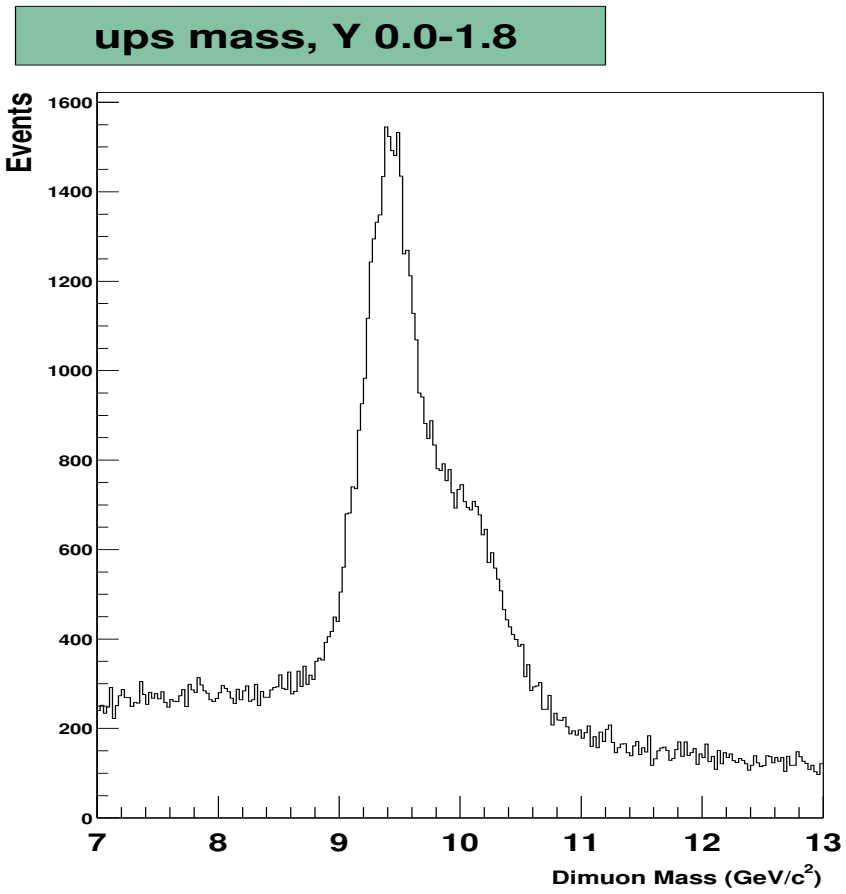

Figure 5.2: Dimuon mass spectra with tight isolation requirements on both muons.

Chapter 6

Monte Carlo Simulation

Monte Carlo simulation is an extremely important tool used in high energy physics. It not only helps to characterize signals and model the backgrounds, but is also essential in calculating the acceptance of the detector and data selection efficiency. At DØ, the simulation consists of two steps: event generation and detector simulation.

6.1 Event Generator and Detector Simulation

At DØ, the most commonly used Monte Carlo event generators for hadron-hadron collisions are ISAJET [51], PYTHIA [52], and HERWIG [53]. For this analysis, PYTHIA (Version 6.202) has been used for the generation of $\Upsilon(1S)$ events. PYTHIA is a program for the generation of high-energy physics events, i.e. for the description of collisions at high energies between elementary particles such as e^+, e^-, p and $\bar{p}$ in various combinations. Based on theoretical understanding it provides models for a number of the physics aspects of the interactions of interest to us, including hard and soft interactions, parton distributions, initial and final state parton showers, multiple interactions, fragmentation and decay. The user supplies the event generator with an input "card file" [54] which specifies the details of the physics processes to be

simulated. The event generator outputs a list of vertices and particle types/four-vectors that come out of those vertices.

The generated events are then processed by detector simulation packages to add detector effects.

The detector simulation consists of two major packages: DØGSTAR [55] and DØSIM [56]. The DØGSTAR package which is based on GEANT [57] (a general detector description and simulation tool) describes the geometry of DØ detector and simulates the behavior of particles passing through the DØ detector in detail. Detector "hits" are generated during this process just as in a real collisions. The DØSIM package does the digitization for each sub-detector, pileup, overlapping minimum bias events and adds noise. The output of the simulation is in the same format as the real data and the simulated events are reconstructed using the same reconstruction packages (DØreco).

6.2 $\Upsilon(1S)$ Monte Carlo Sample

Three $\Upsilon(1S)$ Monte Carlo files are available for this analysis. The same PYTHIA generator v6.202 was used in all cases. All samples had the same p_T cutoff for initial parton scattering ($PTLOW$ parameter) of 1.0 GeV/c but differ in the DØmess [58] selection criteria used before the events were fed through GEANT. Due to limited CPU resources available, events that do not pass certain minimal requirements are rejected after the generator stage. These are typically events that can not be reconstructed for principal reasons, eg., lack of detector coverage. These minimal requirements are listed with each sample and are internally referred as DØmess selection criteria.

The PYTHIA cards used for this generation are available from Ref. [59].

The Monte Carlo samples are:

(a) $PTLOW = 1.0$ GeV/c, $p_T^\mu > 1.0$ GeV/c, $|\eta^\mu| < 3$, 77k events processed by MC farms.

(b) $PTLOW = 1.0$ GeV/c, $p_T^\mu > 1.0$ GeV/c, $|\eta^\mu| < 3$, 30k events processed at IU.

(c) $PTLOW = 1.0$ GeV/c, $p_T^\mu > 1.8$ GeV/c, $|\eta^\mu| < 2.5$, 90k events processed at IU.

In addition, in order to evaluate various corrections, we have used 302.5k J/ψ Monte Carlo events: 190k direct J/ψ events and 112.5k $b \to J/\psi$ events.

Kinematic distributions for dimuons and muons from the $\Upsilon(1S)$ decay (defined here to be dimuons in the mass window: (9.0 – 9.8) GeV/c^2) are shown in Figs. 6.1 and 6.2. We show the dimuon rapidity and p_T spectra as well as muon p_T^μ, η^μ, ϕ^μ distributions for $\Upsilon(1S)$ with $2 < p_T^\Upsilon < 8$ GeV/c, in three different ranges of the $\Upsilon(1S)$ rapidity. For this purpose, we used the data shown in Fig. 5.2, with the isolation requirement of $etTrkCone5 < 1$ GeV/c^2 imposed on each muon. The background events have not been subtracted from the data distributions. Distributions for Monte Carlo events are superimposed in the same plots. Monte Carlo events were processed through the trigger simulator.

Only a fair agreement between data and Monte Carlo is observed for the upsilon transverse momentum spectra. The Monte Carlo p_T^Υ spectrum is steeper than observed in the data. On the other hand, the muon kinematic distributions, in restricted regions of p_T^Υ and y^Υ agree quite well.

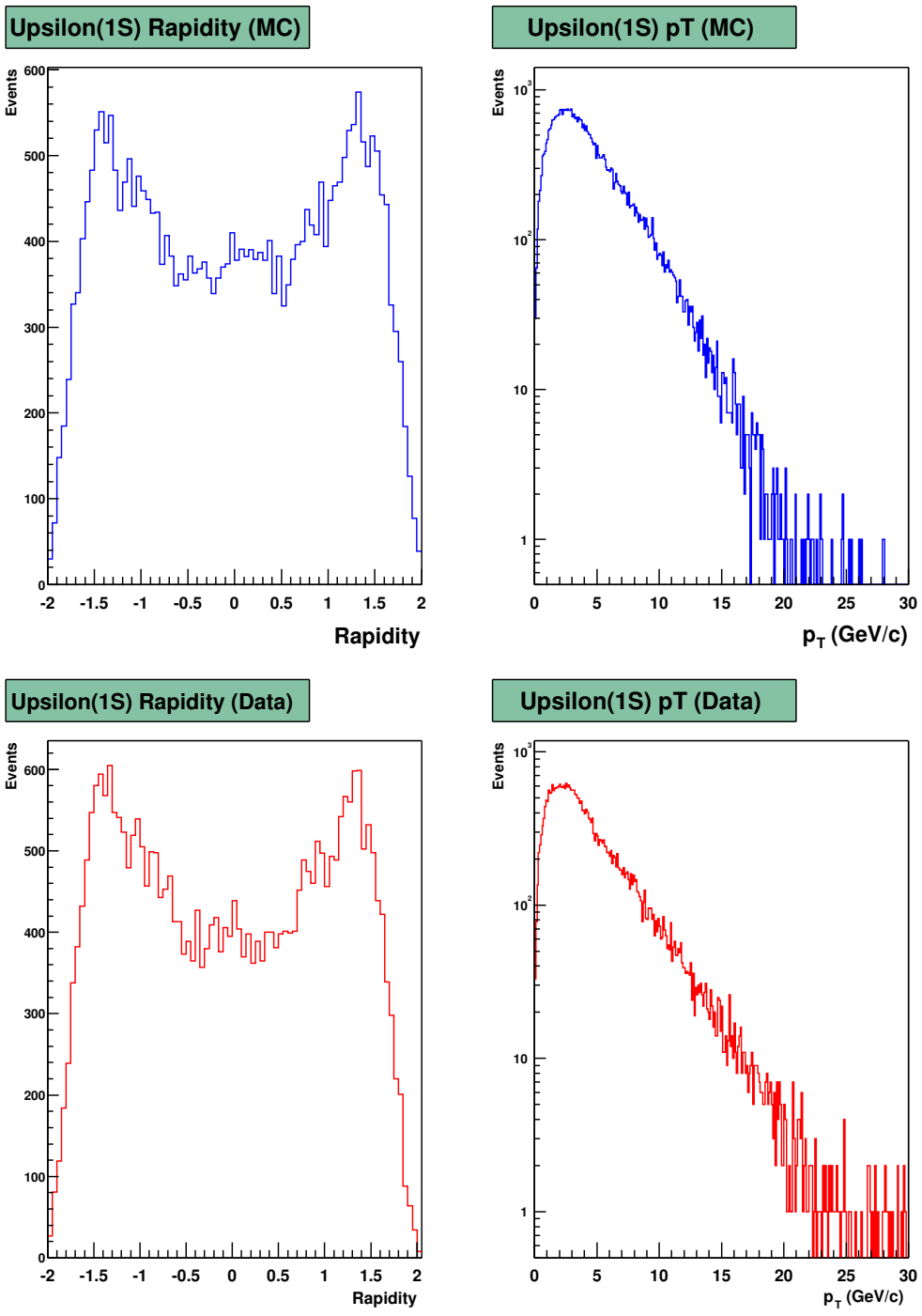

Figure 6.1: Kinematic distributions for dimuons in the (9.0 – 9.8) GeV/c^2 range from data and Monte Carlo.

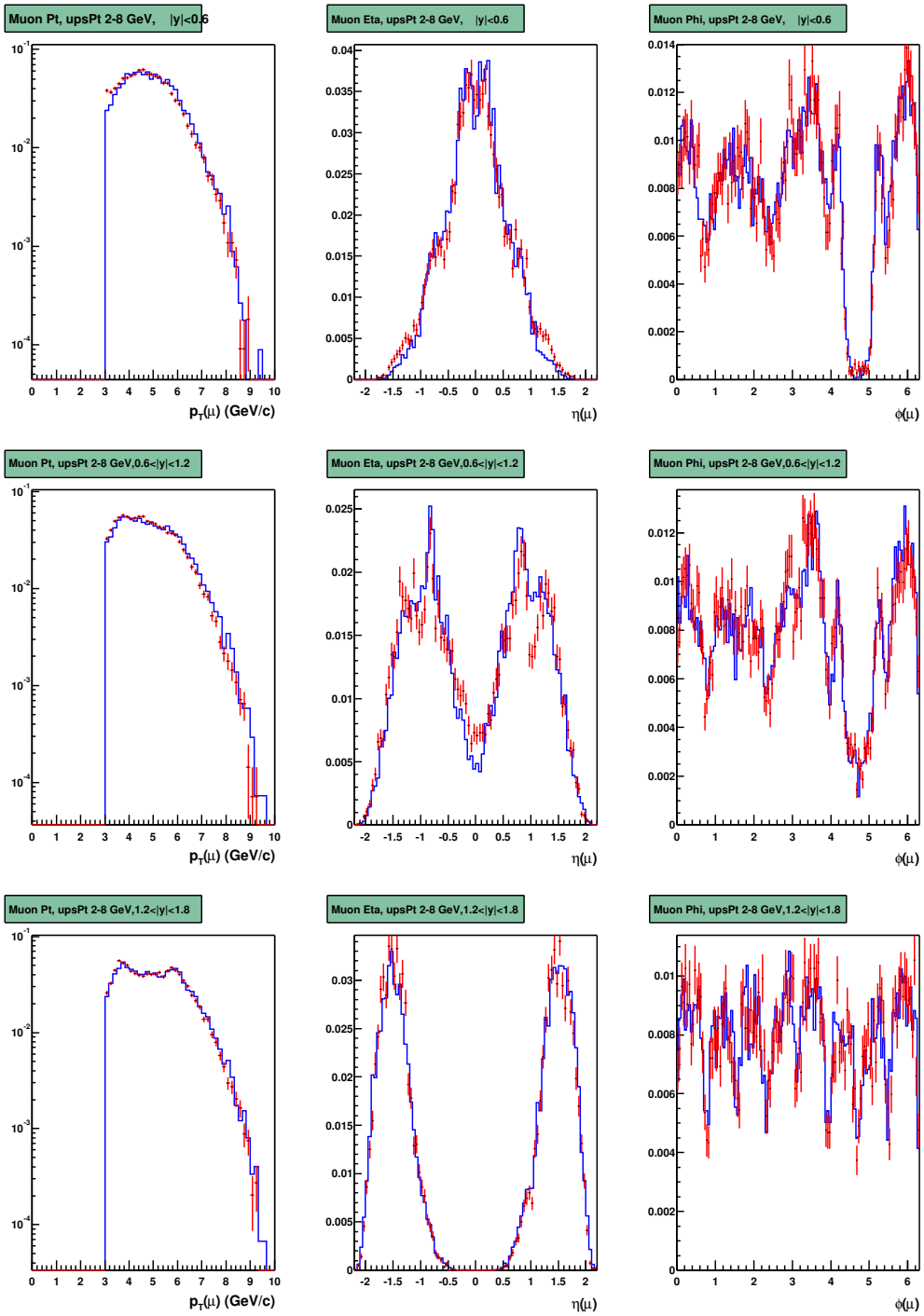

Figure 6.2: Kinematic distributions for muons from dimuon pairs in the (9.0 – 9.8) GeV/c^2 range (data, points) and (MC, histogram).

Chapter 7

Cross Section Calculation

7.1 Cross Section Calculation

The cross section for a given kinematic range, multiplied by the branching ratio $\Upsilon(1S) \to \mu^+\mu^-$, is given by

$$\frac{d^2\sigma(\Upsilon(1S))}{dp_T \cdot dy} = \frac{N(\Upsilon)}{\mathcal{L} \cdot \Delta p_T \cdot \Delta y \cdot \varepsilon_{kinem} \cdot \varepsilon_{acc} \cdot \varepsilon_{trigg-reco} \cdot \varepsilon_{iso-SMT} \cdot \varepsilon_{dimu} \cdot \varepsilon_{trk} \cdot \varepsilon_{fit}} \quad (7.1)$$

where $\mathcal{L}$ is the integrated luminosity of the data sample, $N(\Upsilon(1S))$ is the number of fitted $\Upsilon(1S)$ events and the ε_i represent various efficiency and acceptance factors.

The muon acceptance and reconstruction efficiency is based on a Monte Carlo analysis and has been factorized into two parts: losses due to kinematic cuts on muon momenta before the Monte Carlo events were processed through the simulation/reconstruction packages (ε_{kinem}) and an acceptance/reconstruction efficiency for muons that had a chance to be reconstructed in the detector (ε_{acc}). The product ($\varepsilon_{kinem} \times \varepsilon_{acc}$) represents the fraction of generated $\Upsilon(1S)$ candidates that was successfully reconstructed in the DØ detector, albeit without the trigger condition imposed:

$$\varepsilon_{kinem} \cdot \varepsilon_{acc} = \frac{N(muon\ kine.\ cuts)}{N(all)} \cdot \frac{N(reco)}{N(muon\ kine.\ cuts)} = \frac{N(reco)}{N(all)}. \qquad (7.2)$$

The dimuon trigger efficiency ($\varepsilon_{trigg-reco}$) for reconstructed dimuons was estimated by running a trigger simulator, and also independently derived from the data using other triggers.

We adopted a double-Gaussian mass resolution function with a shape based on the J/ψ signal studies. Compared to a single Gaussian fit, this approach allows for a better separation of individual contributions from the three upsilon states. The factor ε_{fit} is set to 1 and the difference between single- and double-Gaussian fits, corrected for the expected losses, is used to estimate systematic uncertainties of ε_{fit}.

The remaining factors in Eq. A.1 account for the differences between the data and Monte Carlo efficiencies.

The correction ($\varepsilon_{iso-SMT}$) is defined as a ratio of the number of fitted upsilon candidates obtained with and without the data quality cuts (isolation, SMT-hit requirement, cosmic rejection), divided by the corresponding ratio of the Monte Carlo $\varepsilon_{acc} \cdot \varepsilon_{trigg}$ efficiencies for these two cases.

The central track matching correction (ε_{trk}) was derived from the J/ψ data and Monte Carlo and turns out to be very close to unity at the central muon pseudo-rapidity region and drops $\sim 6\%$ at the very forward regions.

The correction factor (ε_{dimu}) accounts for both the differences in the *local* muon reconstruction and trigger efficiencies between data and Monte Carlo. The muon ID certification note [50] suggests that the Monte Carlo overestimates the *local* muon reconstruction efficiency, and the actual efficiency is (91.5 $\pm$ 7.0)% of the Monte Carlo value. This correction seems to be independent of the type of muons used,

and was determined specifically for the $nseg = \pm 3$ muons. The correction does not show a significant p_T dependence, but it changes with the muon pseudo-rapidity. Later, we evaluate relative contributions to the ε_{dimu} correction from the *local* muon reconstruction and from the muon trigger.

A detailed discussion of each contribution to the cross section calculations is covered in Section 7.3.

7.2 Dimuon Mass Distributions and Signal Fits

The dimuon mass distributions were fitted under two conditions that differed in the central track quality and in the muon isolation. The final cross section results are based on the analysis requiring one of the muons to be isolated. Several examples of dimuon mass plots are shown in Fig. 7.1. In each plot a strong $\Upsilon(1S)$ signal is seen, accompanied by a shoulder representing unresolved signals due to $\Upsilon(2S)$ and $\Upsilon(3S)$ production.

The dimuon mass distributions were fitted in the 7.0 (7.8)–13.0 GeV range using three mass resolution functions for each of the $\Upsilon(nS)$ bound states and a third order polynomial for the background. The fit mass range was expanded for larger dimuon transverse momenta. The measured mass of $\Upsilon(1S)$ was a free parameter of the fit, the remaining two masses were shifted by the $m(\Upsilon(nS))$ - $m(\Upsilon(1S))$ differences of 563 MeV ($\Upsilon(2S)$) and 840 MeV($\Upsilon(3S)$), taken from the Particle Data Book [2]. In addition, only the width of the $\Upsilon(1S)$ state, $\sigma(\Upsilon(1S))$, was allowed to vary. The width of the other states were assumed to scale with the mass of the resonance. This assumption is supported by the experimentally observed change in the signal width between the J/ψ and $\Upsilon(1S)$ mass range. The typical width changes from 65 MeV to 200 MeV, exactly as expected (65 MeV $\times$ 9.46/3.097 = 199 MeV). Normalizations

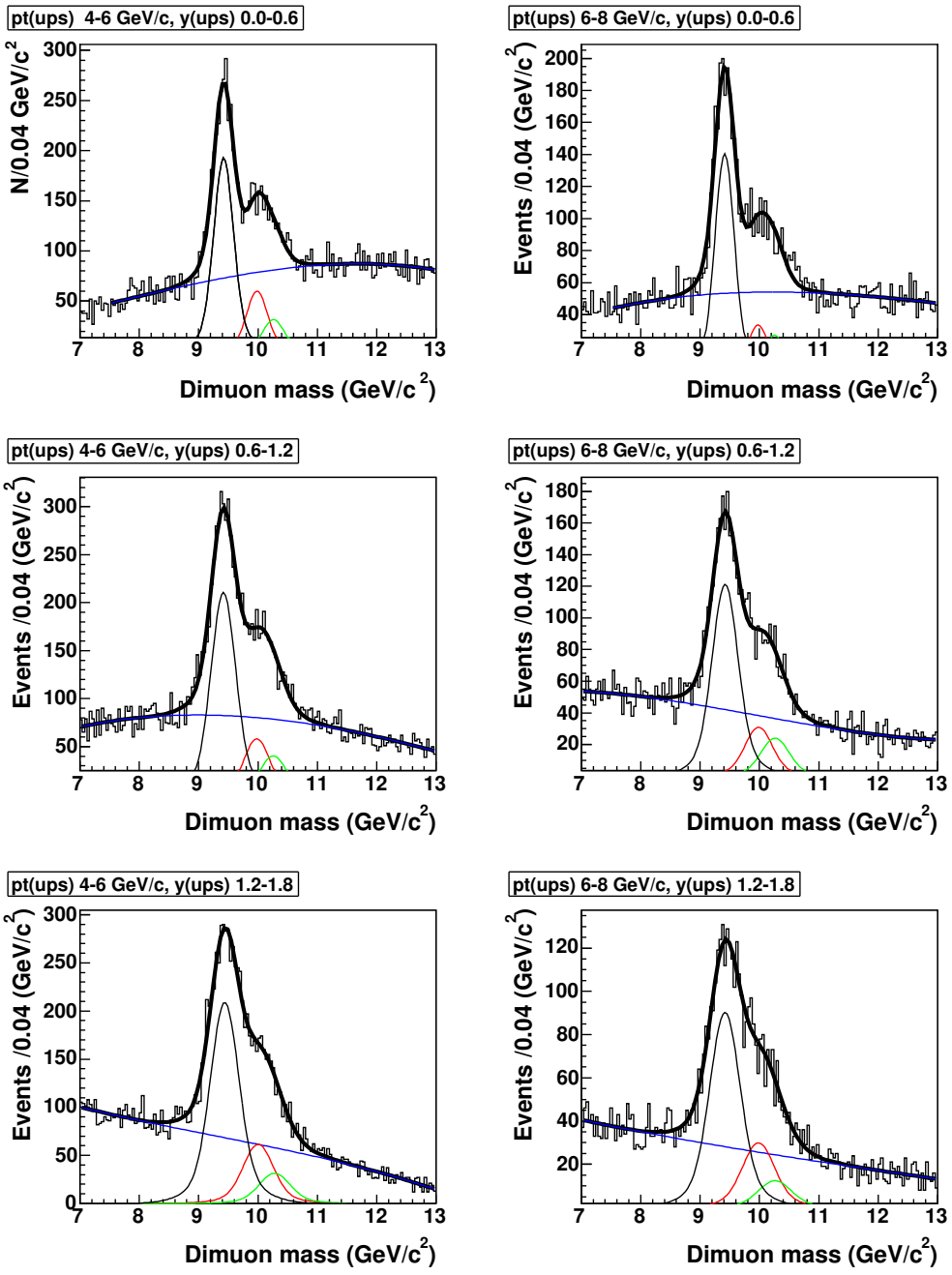

Figure 7.1: Examples of the fits for the dimuon spectra.

of resolution functions representing each resonance were free parameters of the fit.

In the first attempt of the analysis, the mass resolution function was approximated by a single Gaussian. The size of the required correction, ε_{fit}, derived from the $\Upsilon(1S)$ Monte Carlo and the observed J/ψ signal, varied between (93 – 95)%. However, we found that the single-Gaussian $\Upsilon(1S)$ fit is influenced by the presence of the nearby $\Upsilon(2S)$ and $\Upsilon(3S)$ signals. Therefore, we have adopted a double Gaussian resolution function with:

(i) the width of the second Gaussian equal to the width of the first times a constant factor of 2.2;

(ii) the relative contribution of the second Gaussian fixed at 16%.

Only the mass and the width of the first Gaussian were free parameters of the fit. The two constants defining the second Gaussian were taken from our extensive studies of the observed J/ψ mass resolution in different rapidity ranges. We have also studied the sensitivity of the fit results over a wide range of the second Gaussian parameters. Unfortunately, the χ^2 of the fit itself does not have a sufficient sensitivity to differentiate between the assumed $\Upsilon(1S)$ mass resolution functions.

A complete set of all mass distribution together with fit results are shown in Appendix A.

We find the fitted mass $m(\Upsilon(1S))$ to be approximately 40 MeV below the nominal mass of the resonance and the fitted width $\Gamma(\Upsilon(1S))$ to increase from approximately 160 MeV (for $|y^{\Upsilon}| < 0.6$) to (210 – 270) MeV for $1.2 < |y^{\Upsilon}| < 1.8$. For the two lower rapidity ranges, the signal width is almost constant for transverse momenta less than 10 GeV/c (see Fig. 7.2). The fitted width is consistently some 30 MeV larger than that predicted by Monte Carlo (the different is 60 MeV when single Gaussian parameterization for data is used).

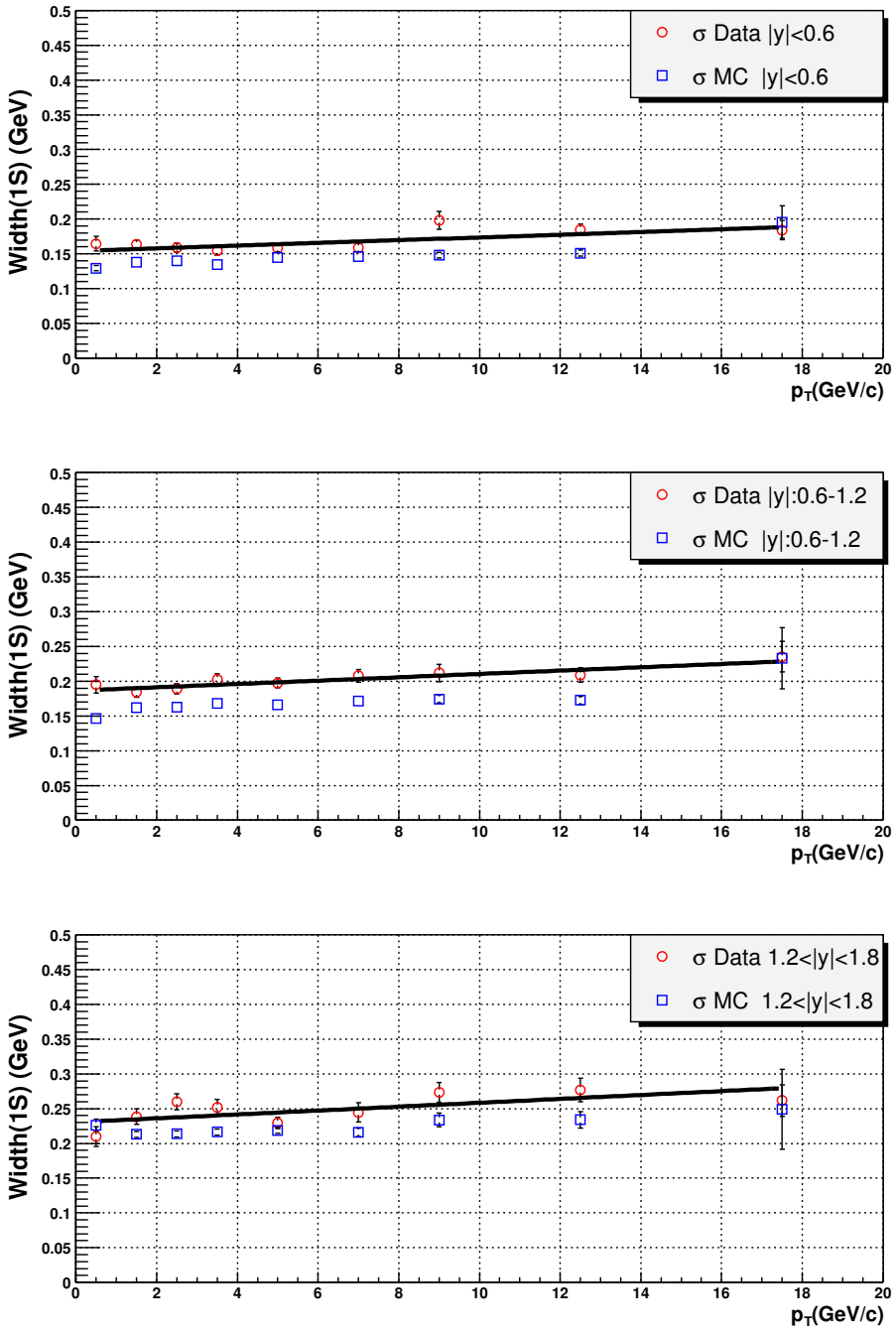

Figure 7.2: Comparison between the fitted signal width in data and Monte Carlo predictions for different rapidity bins.

The uncertainty on the number of fitted events includes the uncertainty in the fitted width. The ratio of the number of fitted $\Upsilon(2S)$ and $\Upsilon(3S)$ candidates (combined) to the number of fitted $\Upsilon(1S)$ candidates, shown in Fig. 7.3, slowly increases with transverse momentum and varies between 40% and 60%.

7.3 Efficiency Determination

7.3.1 Pre-geant

For all efficiency/acceptance studies, we have used Monte Carlo events generated with the initial parton scattering transverse momentum cutoff of $PTLOW = 1.0$ GeV/c. We have used DØmess initial cuts of $p_T^\mu > 1.8$ GeV/c and $|y^\mu| < 2.5$. Originally, we calculated the kinematic (pre-GEANT) efficiencies for these specific cuts. However, to take advantage of the large statistics available at generator level as compared to the relatively low number of events available after full simulation, we chose to determine the ε_{kinem} efficiencies for the $p_T^\mu > 3.0$ GeV/c and $|y^\mu| < 2.2$ cuts. The values of these efficiencies are included in Table 7.1.

We have also studied the dependence of the ε_{kinem} efficiency on the value of the cutoff $PTLOW$. We do not observe a statistically significant variation of ε_{kinem} within the $PTLOW$ range of (1 – 2) GeV/c. The current Monte Carlo statistics limits our systematic uncertainty for this efficiency to less than 1%.

7.3.2 Acceptance and Reco

For the calculations of the acceptance and trigger and reconstruction efficiency, we used fully reconstructed Monte Carlo events. The acceptances were normalized to

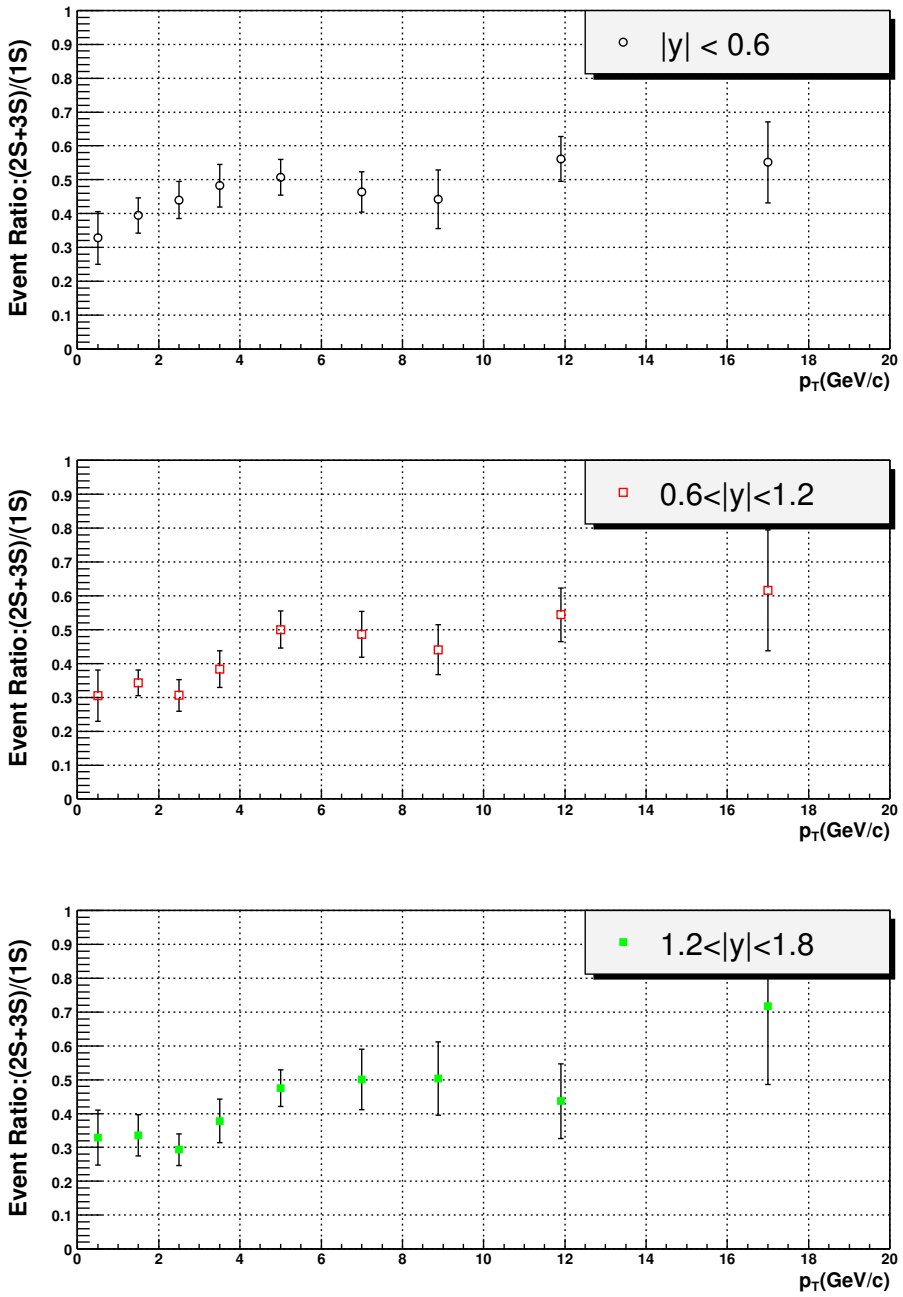

Figure 7.3: Ratio of the number of fitted $\Upsilon(2S)$ plus $\Upsilon(3S)$ candidates to the number of fitted $\Upsilon(1S)$ candidates as a function of transverse momentum for different rapidity bins.

the number of dimuons passing the muon preselection cuts described in the Pre-geant section:

$$\varepsilon_{acc} = \frac{N(recoed - events, p_T^{\mu} > 3GeV, |\eta^{\mu}| < 2.2, \mu_{ID}\ cuts)}{N(generated - events, p_T^{\mu} > 3GeV, |\eta^{\mu}| < 2.2)}. \tag{7.3}$$

The muon momentum smearing effect is taken into account by using reconstructed muon momenta for the numerator cuts and nominal muon momenta in the denominator.

7.3.3 Trigger

The Level 1 and Level 2 trigger simulator was run on the accepted/reconstructed Monte Carlo events, and its efficiency was normalized to the reconstructed events with our kinematic cuts on muons. The full dimuon trigger efficiency was obtained by multiplying the Monte Carlo Level 1 trigger efficiency by the relative Level 2 / Level 1 efficiency derived from data. This correction was at the $(96.5 - 98.5)\%$ level, in good agreement with the Level 2 trigger simulator prediction. We use the combined Level 1 and Level 2 efficiencies from Monte Carlo to the same effect. The trigger efficiency is defined as

$$\varepsilon_{trigg-reco} = \frac{N(recoed - events, p_T^{\mu} > 3GeV,\ |\eta^{\mu}| < 2.2, \mu_{ID}cuts, triggered)}{N(recoed - events, p_T^{\mu} > 3GeV,\ |\eta^{\mu}| < 2.2,\ \mu_{ID}cuts)} \tag{7.4}$$

The acceptances and trigger efficiencies are listed in Table 7.1 and trigger efficiencies are plotted in Fig. 7.4. The trigger efficiency for fully reconstructed dimuon

p_T^{Υ} GeV/c	ε_{kine} Monte Carlo	ε_{acc} Monte Carlo	$\varepsilon_{trigg-reco}$ MCarlo + Data
$\lvert\eta^{\Upsilon}\rvert < 0.6$			
0 – 1	0.734±0.004	0.351 ±0.010	0.684 ± 0.018
1 – 2	0.683±0.003	0.328 ±0.006	0.705 ± 0.011
2 – 3	0.631±0.002	0.297 ±0.005	0.694 ± 0.011
3 – 4	0.574±0.002	0.268 ±0.006	0.684 ± 0.012
4 – 6	0.483±0.002	0.302 ±0.005	0.697 ± 0.010
6 – 8	0.470±0.003	0.371 ±0.007	0.699 ± 0.013
8 – 10	0.519±0.014	0.407 ±0.010	0.705 ± 0.016
10 – 15	0.580±0.005	0.418 ±0.012	0.755 ± 0.018
15 – 20	0.696±0.014	0.478 ±0.035	0.688 ± 0.051
$0.6 < \lvert\eta^{\Upsilon}\rvert < 1.2$			
0 – 1	0.738±0.004	0.382 ± 0.010	0.682 ± 0.017
1 – 2	0.684±0.003	0.385 ± 0.006	0.692 ± 0.011
2 – 3	0.631±0.002	0.378 ± 0.006	0.699 ± 0.010
3 – 4	0.572±0.003	0.360 ± 0.006	0.702 ± 0.011
4 – 6	0.477±0.002	0.376 ± 0.006	0.716 ± 0.009
6 – 8	0.465±0.003	0.401 ± 0.008	0.768 ± 0.011
8 – 10	0.511±0.004	0.442 ± 0.011	0.741 ± 0.016
10 – 15	0.591±0.005	0.480 ± 0.013	0.763 ± 0.017
15 – 20	0.649±0.016	0.589 ± 0.039	0.816 ± 0.042
$1.2 < \lvert\eta^{\Upsilon}\rvert < 1.8$			
0 – 1	0.589±0.005	0.466 ± 0.013	0.802 ± 0.016
1 – 2	0.580 ±0.003	0.473 ± 0.008	0.803 ± 0.010
2 – 3	0.545±0.003	0.486 ± 0.007	0.783 ± 0.009
3 – 4	0.506±0.003	0.497 ± 0.007	0.788 ± 0.009
4 – 6	0.412±0.002	0.483 ± 0.007	0.798 ± 0.008
6 – 8	0.369 ±0.003	0.490 ± 0.010	0.828 ± 0.011
8 – 10	0.403±0.004	0.463 ± 0.013	0.798 ± 0.017
10 – 15	0.489±0.006	0.485 ± 0.016	0.828 ± 0.018
15 – 20	0.592±0.018	0.570 ± 0.048	0.895 ± 0.042

Table 7.1: Detector acceptance and trigger efficiency.

events varies from 65% in the central rapidity region to 80% in the forward region.

Trigger efficiency verification

Two methods are used to verify trigger efficiencies with the data:

- Method I: calculate relative efficiencies of our dimuon triggers with respect to other triggers and compare the results with those from the Level 1 and Level 2 trigger simulator.
- Method II: use the J/ψ data sample collected with single muon triggers, identify the trigger muon and check if the other muon also triggered. The same procedure is applied to both data and Monte Carlo and the results are compared. Final corrections to the trigger simulator efficiencies are based on this method.

We also refer to the verification of the Level 1 single muon trigger simulator against analysis done by the Arizona group [63]. There is an agreement to within 5% for muon transverse momenta above 3 GeV/c.

The relative trigger efficiencies obtained from data and Monte Carlo are plotted as a function of the upsilon transverse momentum in Figs. 7.4 and 7.5. It also shows the absolute trigger efficiencies obtained from Monte Carlo (for the Level 1 trigger *mu2ptxatxx-fz*) and corrected using data for the additional Level 2 requirements. Figure 7.4 is obtained by using all events in the (9.0 - 9.8) GeV/c^2 mass window and Fig. 7.5 by performing standard mass fits for the $\Upsilon(1S)$ signal. The relative trigger efficiencies calculated for the sidebands give numerical values consistent with those for the selected signal region.

For data at $|\eta^{\Upsilon}| \leq 1.2$, these plots show a rather low relative trigger efficiency with respect to single muon triggers ($\approx 70\%$ when averaged over the full Υ transverse

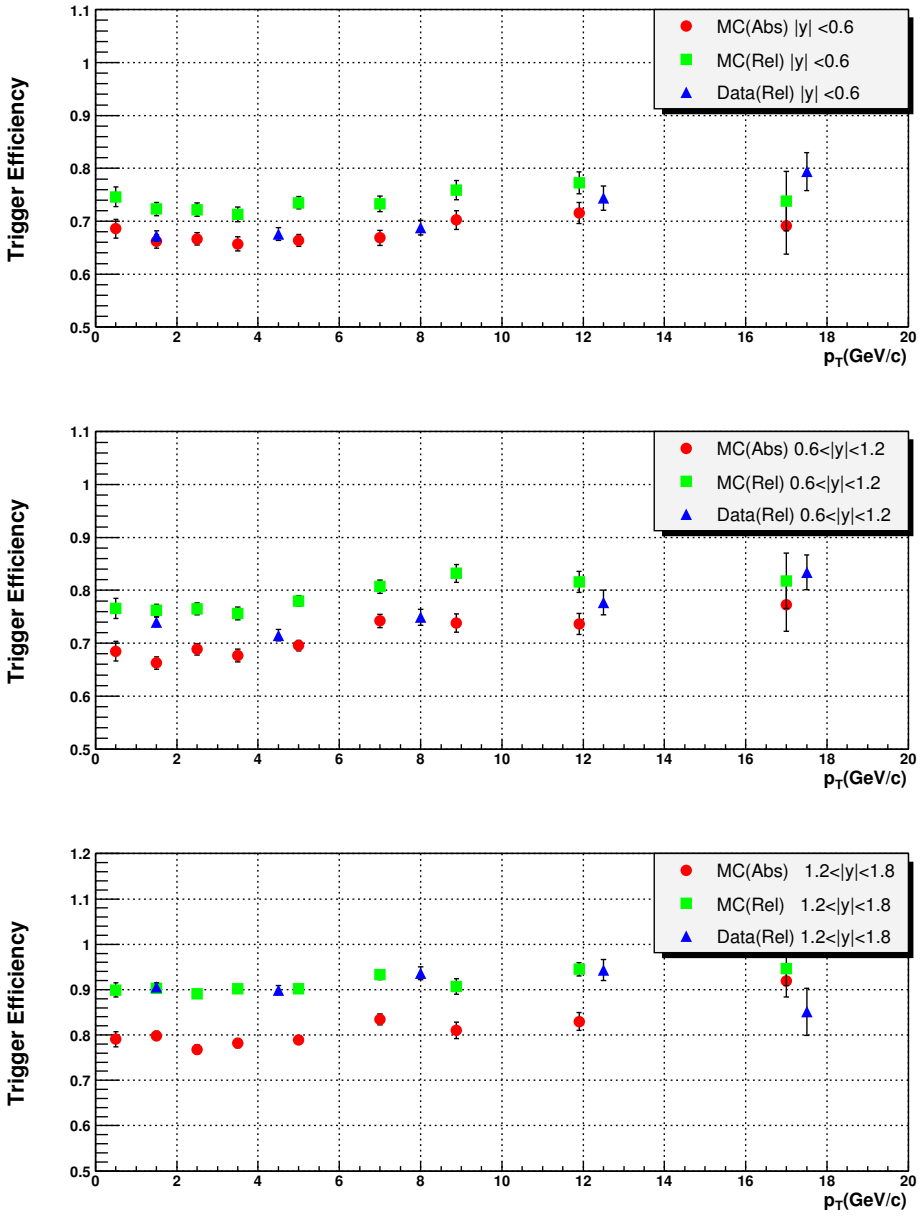

Figure 7.4: Comparison of relative trigger efficiency derived from Monte Carlo events processed through the trigger simulator and from data. Absolute trigger efficiencies for the dimuon trigger are also shown. The data points were obtained for dimuon events in the mass range of (9.0 – 9.8) GeV/c^2.

momentum range; This relative efficiency also holds for the data sample with both muons isolated (for the mass spectrum shown in Fig. 5.2). The combined Level 1 and Level 2 trigger simulator predicts these relative efficiencies to be some (5 –10)% higher, also, irregardless of the isolation requirement. The data and Monte Carlo agreement is very good for the large Υ rapidity range.

7.3.4 Central Tracking

The efficiency for the central tracking has increased substantially in DØreco since 2004. This conclusion, based on our own studies, is confirmed by independent investigations [61] [62] on higher momentum muons. To estimate this efficiency, we used the J/ψ signal observed in the dimuon skimmed events [49], satisfying at least one of the dimuon triggers. We analyzed the dimuon mass spectra for two "tight" local muon candidates, the first muon being matched to a central track $nseg = 3$, *central-rank* $= 1$, $p_T^\mu > 3.0$ GeV/c, track match $\chi^2 < 100$, the number of SMT hits > 0), the second muon being of either $nseg = 3$ or $nseg = -3$ type. The dimuon invariant mass was calculated in each case using the "global-local" tracking information. The J/ψ mass resolution for the "global-local" case was determined for each kinematic bin using events in the (2.83 – 3.37) GeV/c^2 dimuon mass window from the "global-global" mass distribution. This resolution was parametrized by a double Gaussian function with mean masses allowed to be different, to account for the asymmetry in the resolution function. This function plus a second-order polynomial were then used to fit the "global-local" mass spectra in the (0.6 – 6.6) GeV/c^2 range. This was done for three ranges of the second muon transverse momentum and in five different regions of its rapidity - fifteen different kinematic regions in total.

The fit was done twice: (a) for muon pairs with the second muon either $nseg = 3$ or $nseg = -3$ type, and (b) for the $nseg = -3$ type muons only. From the ratio of the

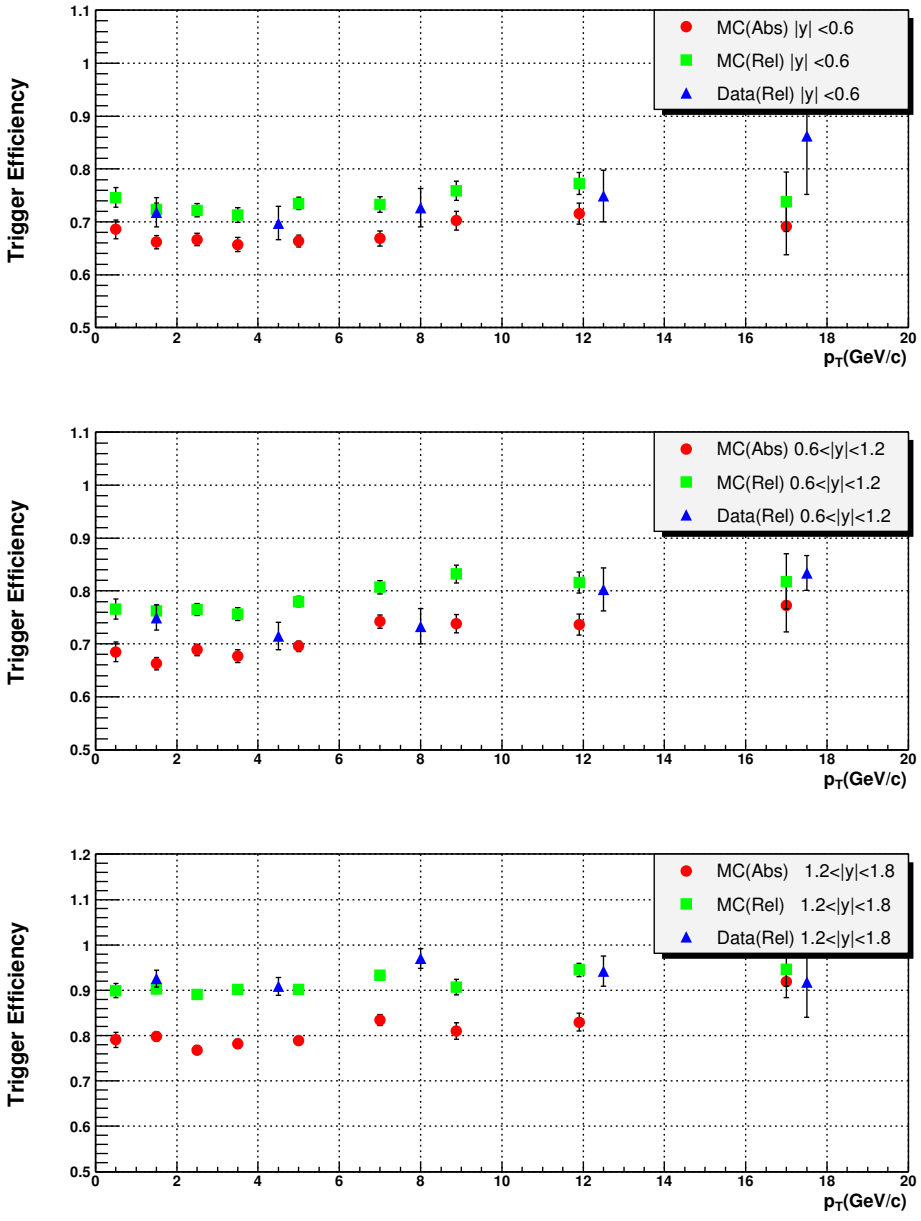

Figure 7.5: Comparison of relative trigger efficiency derived from Monte Carlo events processed through the trigger simulator and from data. Absolute trigger efficiencies for the dimuon trigger are also shown. Same as previous figure, except that the data points were obtained from fits to the mass spectra.

number of J/ψ candidates fitted in both cases we derive the tracking efficiency for a given kinematic region.

Examples of mass spectra fitted both ways are shown in Fig. 7.6. There is little variation of the efficiency with muon p_T. Therefore we have combined all p_T bins in a given muon pseudo-rapidity bin and determined a single tracking efficiency for $p_T^\mu > 3.0$ GeV/c. The efficiency is above 97% for $|\eta^\mu| < 1.5$ and decreases to 90% for $|\eta^\mu| > 1.6$.

The same procedure applied to Monte Carlo events yields tracking efficiencies consistent with the data to within 1% except for the two very forward regions where data efficiency is less than 96% of the Monte Carlo value. The tracking efficiencies derived from the data and Monte Carlo are collected in Table 7.2. Their ratios shown in Fig. 7.7, applied to individual muons from the Υ decay and averaged over a given Υ rapidity/p_T bin, were used as a correction to the tracking efficiency.

rapidity range	data	Monte Carlo	correction
0.0 – 0.4	0.974 ±0.01	0.979 ±0.004	1.00±0.01
0.4 – 0.8	0.992±0.01	0.993 ±0.004	1.00±0.01
0.8 – 1.2	0.991 ±0.01	0.987 ±0.004	1.00±0.01
1.2 – 1.6	0.975 ±0.01	0.982 ±0.003	1.00±0.01
1.6 – 1.8	0.910±0.01	0.951 ±0.005	0.957±0.01
1.8 – 2.2	0.859 ±0.01	0.942 ±0.005	0.912±0.01

Table 7.2: Tracking efficiency for p_T^μ >3.0 GeV/c.

The tracking efficiency for dimuons was estimated by weighting Monte Carlo events with weights being a product of tracking efficiencies for individual muons.

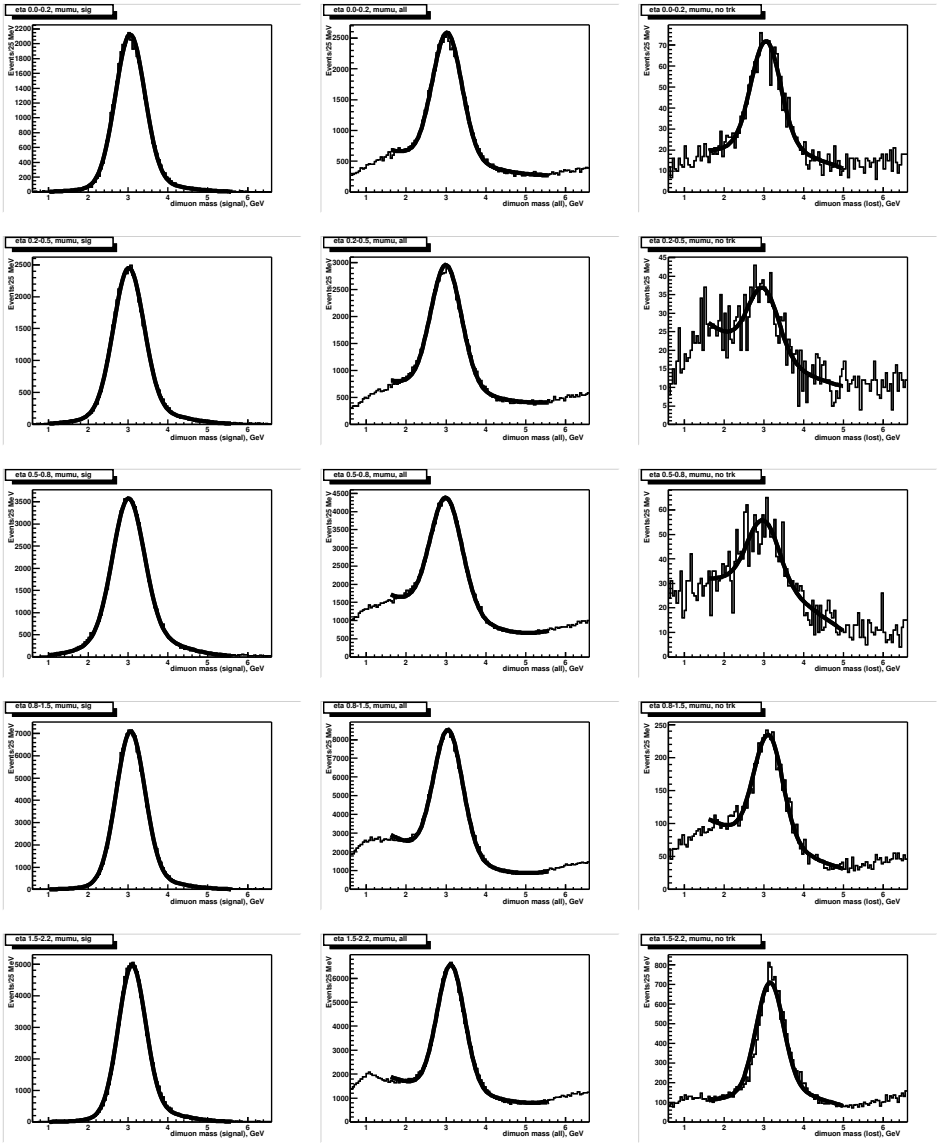

Figure 7.6: Dimuon mass distributions in different η^{μ} regions: First column: "global-local" for signal events, second column: "global-local" for all events and third column: "global-local" for events with one $nseg = -3$ muon.

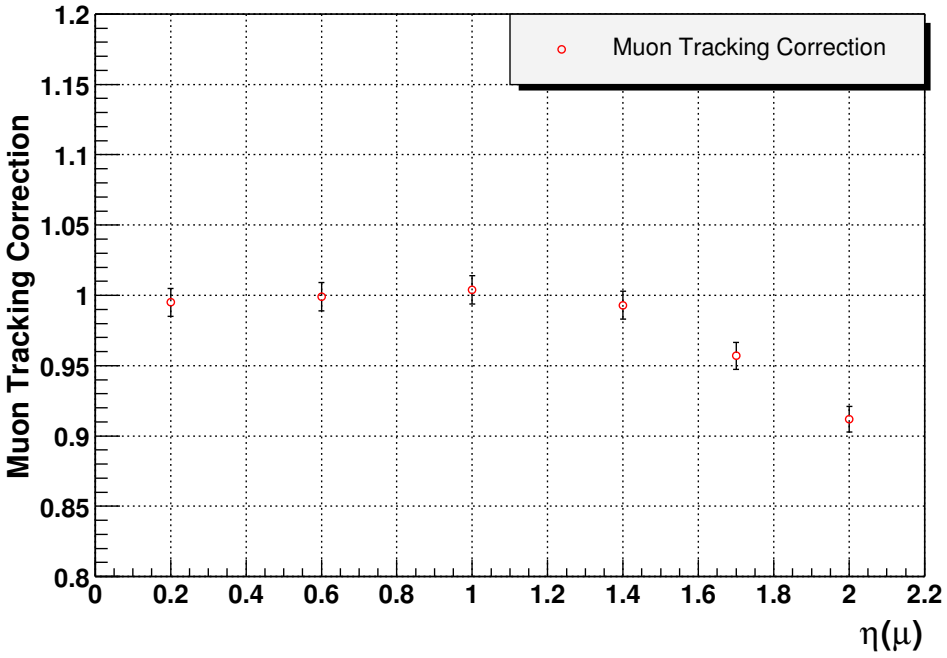

Figure 7.7: Ratio of the combined track and track-muon matching efficiencies derived from data and Monte Carlo as a function of muon pseudo-rapidity for muons with $p_T > 3$ GeV/c.

7.3.5 Muon Quality

The SMT hit requirement improves the dimuon mass resolution by (10–20)% , but removes (10–40)% of the data. Results presented in Table 7.3 were used to derive the correction factor $\varepsilon_{iso-SMT}$. It is defined as a ratio of the numbers of fitted upsilon candidates obtained with and without the data quality cuts (isolation, SMT-hit requirement, cosmic rejection), divided by the corresponding ratio of the Monte Carlo $\varepsilon_{acc} \cdot \varepsilon_{trigg}$ efficiencies for these two cases.

$$\varepsilon_{iso-SMT} = \frac{N(recoed\ events,\ with\ cuts)}{N(recoed\ events, without\ cuts)} \cdot \frac{\varepsilon_{acc} \cdot \varepsilon_{trigg}(without\ cuts)}{\varepsilon_{acc} \cdot \varepsilon_{trigg}(with\ cuts)}. \quad (7.5)$$

This ratio of ratios was calculated for each $\Upsilon(1S)$ p_T and rapidity bin. The correction exhibits very little variation with p_T at all rapidities and its dependence on p_T for a given rapidity range was approximated by a constant, as illustrated in Fig. 7.8. The average values of the correction are consistent with the rough estimates discussed in the next subsection. The fit uncertainties are propagated as systematic uncertainties.

7.3.6 Muon Identification and Trigger

According to the muon ID group [50], the absolute efficiency for the *medium* quality, $nseg = \pm\ 3$ muons is $(65 \pm 5)\%$. The difference between the local muon acceptance/reco efficiency predicted by Monte Carlo and the data is (91.5±7.0)%, independent of the local muon object quality and environment. This number is averaged over the rapidity range $(-2, 2)$. Using the single muon skimmed events [49] for which

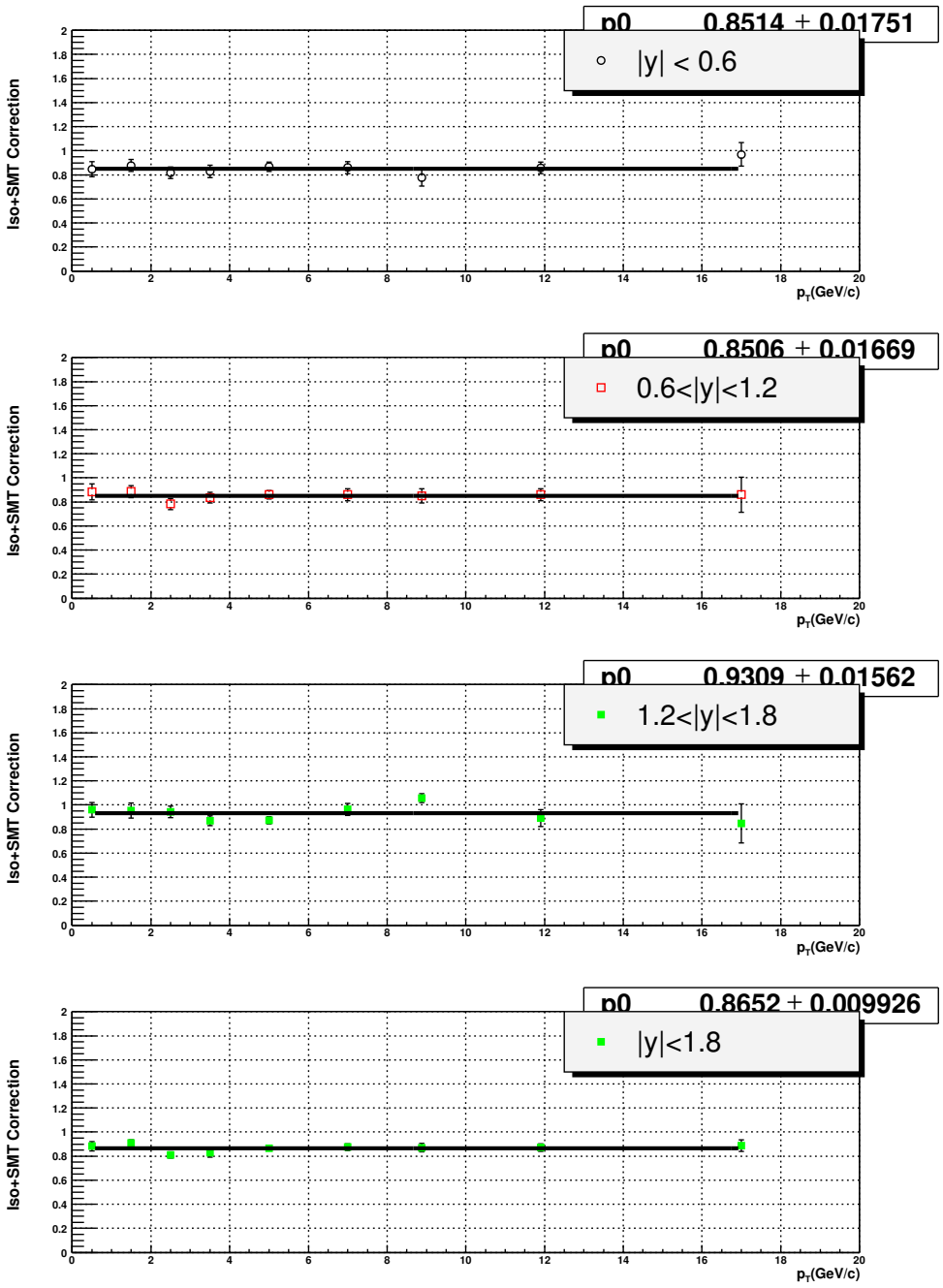

Figure 7.8: Data-derived corrections for the muon isolation and SMT-hit requirements as a function of the upsilon transverse momentum for different rapidity regions.

p_T^{Υ} GeV/c	2MU-A-L2M0 or 2MU-A-L2ETAPHI no SMT, cosmic requirements	2MU-A-L2M0 or 2MU-A-L2ETAPHI SMT+no cosmic+isolation
$\lvert\eta^{\Upsilon}\rvert < 0.6$		
0 – 1	1367 ± 118	932 ± 82 (39)
1 – 2	2907 ± 181	2108 ± 117 (68)
2 – 3	2858 ± 174	1989 ± 116 (54)
3 – 4	2278 ± 151	1553 ± 97 (34)
4 – 6	3035 ± 169	2232 ± 116 (42)
6 – 8	2243 ± 149	1630 ± 101 (43)
8 – 10	1596 ± 137	1042 ± 89 (18)
10 – 15	1681 ± 113	1219 ± 77 (18)
15 – 20	440 ± 58	336 ± 38 (4)
$0.6 < \lvert\eta^{\Upsilon}\rvert < 1.2$		
0 – 1	1499 ± 135	1244 ± 100 (72)
1 – 2	3282 ± 198	2580 ± 143 (107)
2 – 3	3721 ± 211	2708 ± 144 (98)
3 – 4	3527 ± 199	2634 ± 143 (92)
4 – 6	3905 ± 202	3040 ± 154 (75)
6 – 8	2364 ± 155	1842 ± 113 (58)
8 – 10	1686 ± 134	1293 ± 100 (30)
10 – 15	1668 ± 118	1220 ± 86 (27)
15 – 20	421 ± 71	306 ± 42 (10)
$1.2 < \lvert\eta^{\Upsilon}\rvert < 1.8$		
0 – 1	1227 ± 126	1113 ± 100 (51)
1 – 2	3260 ± 245	2902 ± 174 (167)
2 – 3	3792 ± 264	3473 ± 192 (264)
3 – 4	3740 ± 232	3184 ± 182 (176)
4 – 6	4136 ± 200	3500 ± 164 (154)
6 – 8	1755 ± 149	1613 ± 120 (69)
8 – 10	1029 ± 94	1037 ± 80 (48)
10 – 15	1278 ± 113	1050 ± 88 (44)
15 – 20	296 ± 44	248 ± 35 (10)

Table 7.3: Number of fitted $\Upsilon(1S)$ events.

the single muon trigger*MUW-L2M0-2TK3-MM* fired, we did an independent investigation of this correction.

The local muon acceptance/reco efficiency for a given muon p_T^μ and η^μ range was estimated from the data using the following steps:

1. Require the trigger muon to be a "tight" muon with $nseg = 3$, χ^2 for the central track match < 100 and $p_T^\mu > 4.0$ GeV/c. The matched central track is required to have at least 1 SMT hit, more than 13 CFT hits, and $\chi^2 < 10$. The muon Level 2 trigger information was available for the parts of the dataset only. For these events we verified that our selection criteria correctly tagged 98% of the trigger muons.

2. Combine the trigger muon to form a J/ψ

   (a) with other muon candidates in the event, and

   (b) with all tracks in the event.

3. Establish a double Gaussian mass resolution function for the data set (a) and apply (with the shape parameters fixed) to the data set (b)

   We checked the stability of the results by:

   (i) repeating the mass fits with a single Gaussian resolution function,

   (ii)varying the order of the background polynomial, and

   (iii)comparing the fit results for the full data sample (b) and for the data subsamples: (a), and (b) minus (a).

4. Muon acceptance/reco efficiency is calculated as the number of J/ψ candidates from sample (a) divided by the number of J/ψ candidates from sample (b).

5. Apply the same procedure to data and Monte Carlo events, processed through the dimuon trigger simulator (both Level 1 and 2).

   The procedure was used for muons in seven η bins and with transverse momenta in the 3 to 4 GeV/c, 4 to 5 GeV/c, 5 to 7 GeV/c and above 7 GeV/c. Its purpose was twofold: (i) to establish a muon ID efficiency for the second muon ($nseg = 3$, "Loose"), and (ii) to establish a combined muonID and trigger efficiency by adding a requirement that the dimuon trigger be also satisfied for the event.

6. Ratios of data and Monte Carlo efficiencies obtained were plotted as functions of transverse momentum in different rapidity bins to minimize differences in the kinematic distributions between data and Monte Carlo. It has been verified that the average muon transverse momenta for a given muon p_T and η bin are almost identical for both cases.

The stability of the results was verified by varying the p_T of the triggering muon within the (3.5 – 4.5) GeV/c range, imposing an isolation requirement on the tested muon, using only direct J/ψ production Monte Carlo, and dropping the L2 trigger requirement. Our systematic uncertainties are based on these variations. Examples of the mass fits are shown in Fig. 7.9. Muon ID efficiencies for data and Monte Carlo are listed in Tables 7.4 and 7.5.

The ratios of data and Monte Carlo muon-ID efficiencies are plotted as a function of muon p_T in Figs. 7.10 and 7.11. There is little p_T dependence observed for these ratios and the p_T averaged values (results of a constant fit to these distributions) are plotted as a function of muon pseudo-rapidity in Figs. 7.12 and 7.13 and tabulated in Table 7.6.

The data and Monte Carlo ratio for the muon ID efficiency varies significantly

pseudo-rapidity range	data	Monte Carlo	ratio
0.0 – 0.3	0.143 ±0.010	0.153 ±0.010	0.935 ± 0.089
0.3 – 0.6	0.190 ±0.012	0.203 ±0.011	0.936 ± 0.078
0.6 – 0.9	0.366 ±0.015	0.440 ±0.013	0.832 ± 0.042
0.9 – 1.2	0.502 ±0.019	0.471 ±0.014	1.066 ± 0.051
1.2 – 1.5	0.737 ±0.025	0.652 ±0.015	1.130 ± 0.046
1.5 – 1.8	0.841 ±0.049	0.834 ±0.015	1.008 ± 0.061
1.8 – 2.2	0.672 ±0.147	0.430 ±0.024	1.563 ± 0.353

Table 7.4: Combined local muon-ID and trigger efficiency for $3.0 < p_T^{\mu} < 4.0$ GeV/c.

pseudo-rapidity range	data	Monte Carlo	ratio
0.0 – 0.3	0.708 ±0.019	0.733 ±0.011	0.966 ± 0.030
0.3 – 0.6	0.572 ±0.016	0.649 ±0.012	0.881 ± 0.030
0.6 – 0.9	0.572 ±0.016	0.673 ±0.012	0.850 ± 0.028
0.9 – 1.2	0.621 ±0.017	0.676 ±0.012	0.919 ± 0.030
1.2 – 1.5	0.885 ±0.021	0.871 ±0.010	1.016 ± 0.027
1.5 – 1.8	0.798 ±0.037	0.838 ±0.015	0.952 ± 0.047
1.8 – 2.2	0.519 ±0.091	0.578 ±0.032	0.898 ± 0.165

Table 7.5: Combined local muon-ID and trigger efficiency for $p_T^{\mu} > 4.0$ GeV/c.

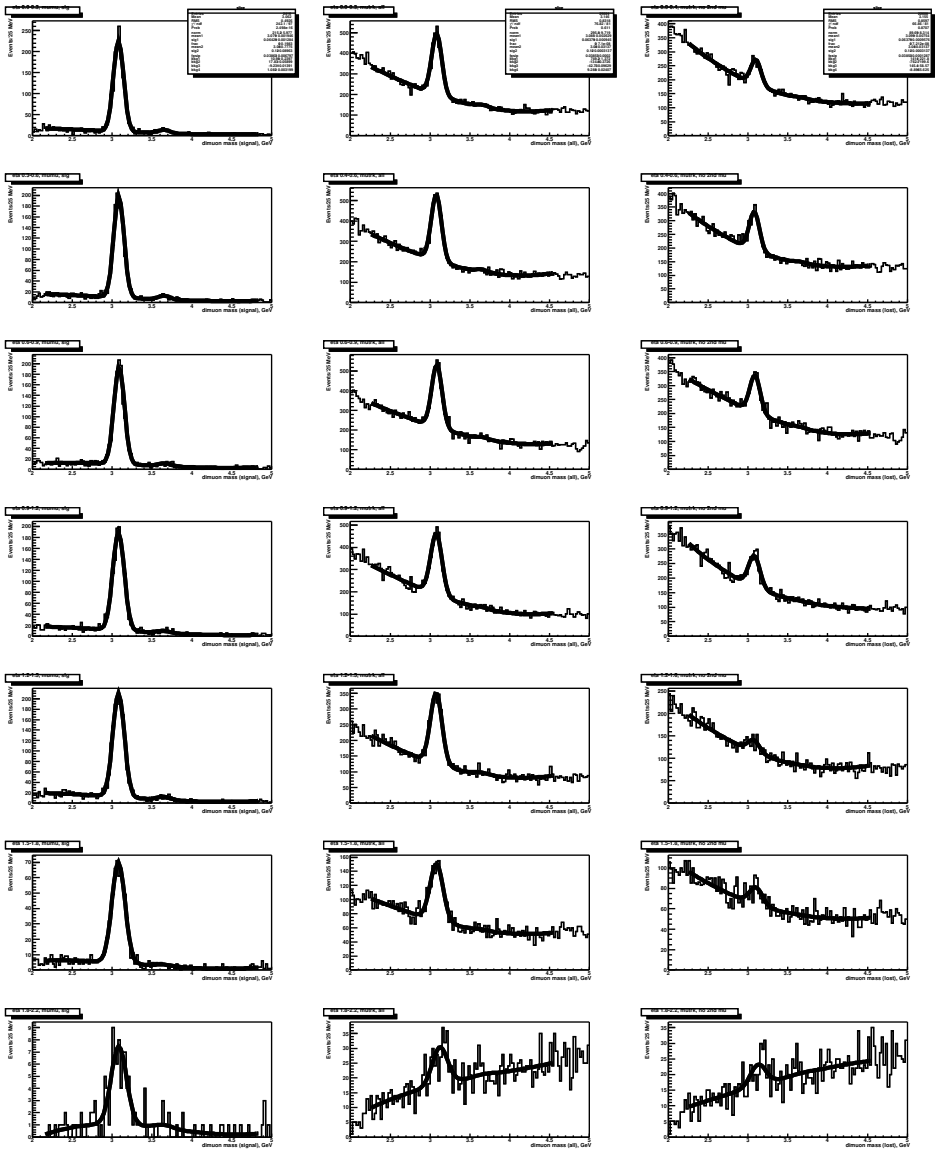

Figure 7.9: Invariant mass distributions in different η^{μ} regions. First column: "muon-muon" events, second column: "muon-track" for all events and third column: "muon-track" for events without a track-muon match. Events were triggered by a single-muon trigger. The first muon used in each pair was the trigger muon.

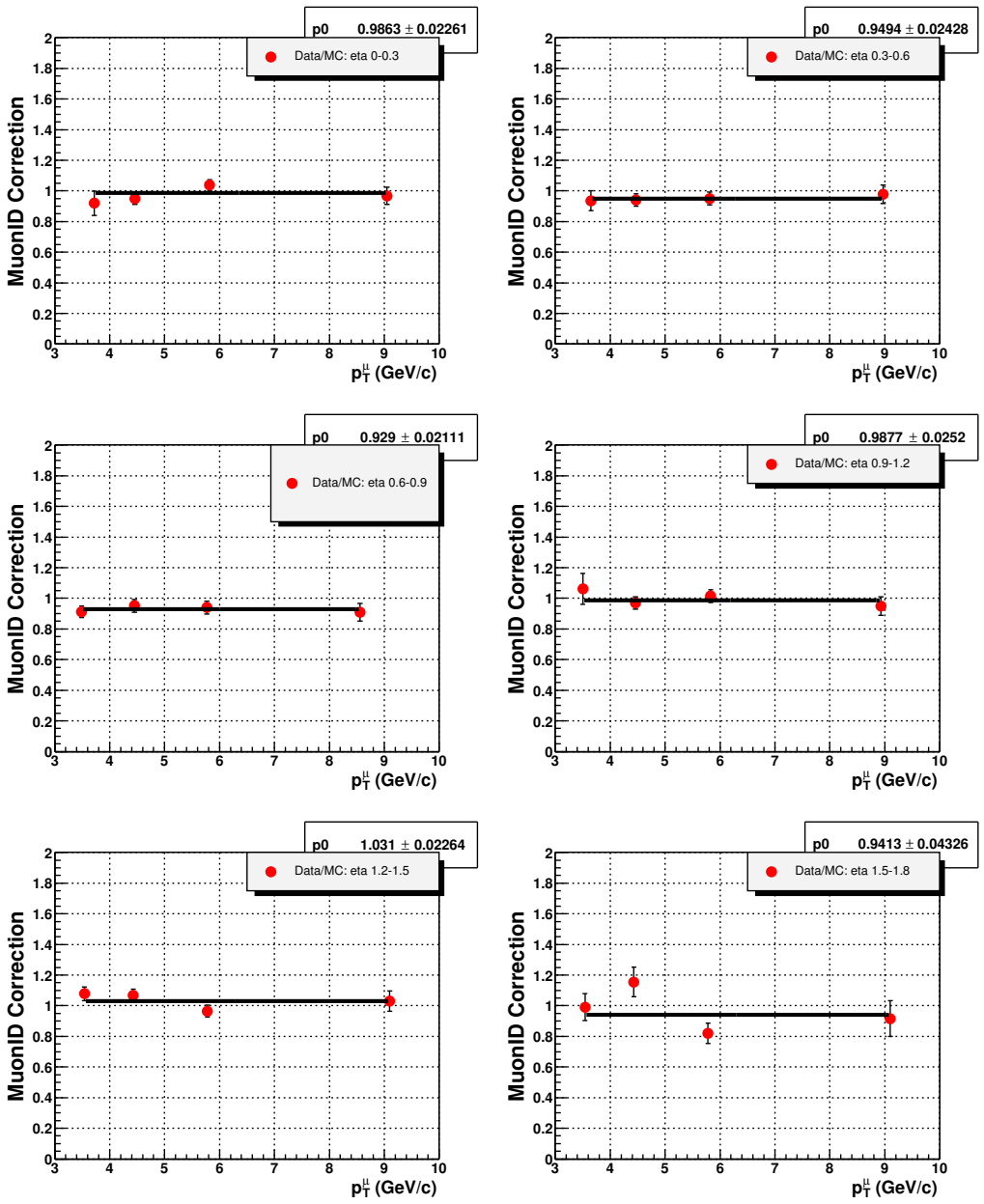

Figure 7.10: Data and Monte Carlo ratio of the local muon-ID efficiency as a function of muon transverse momentum for different muon pseudo-rapidity regions.

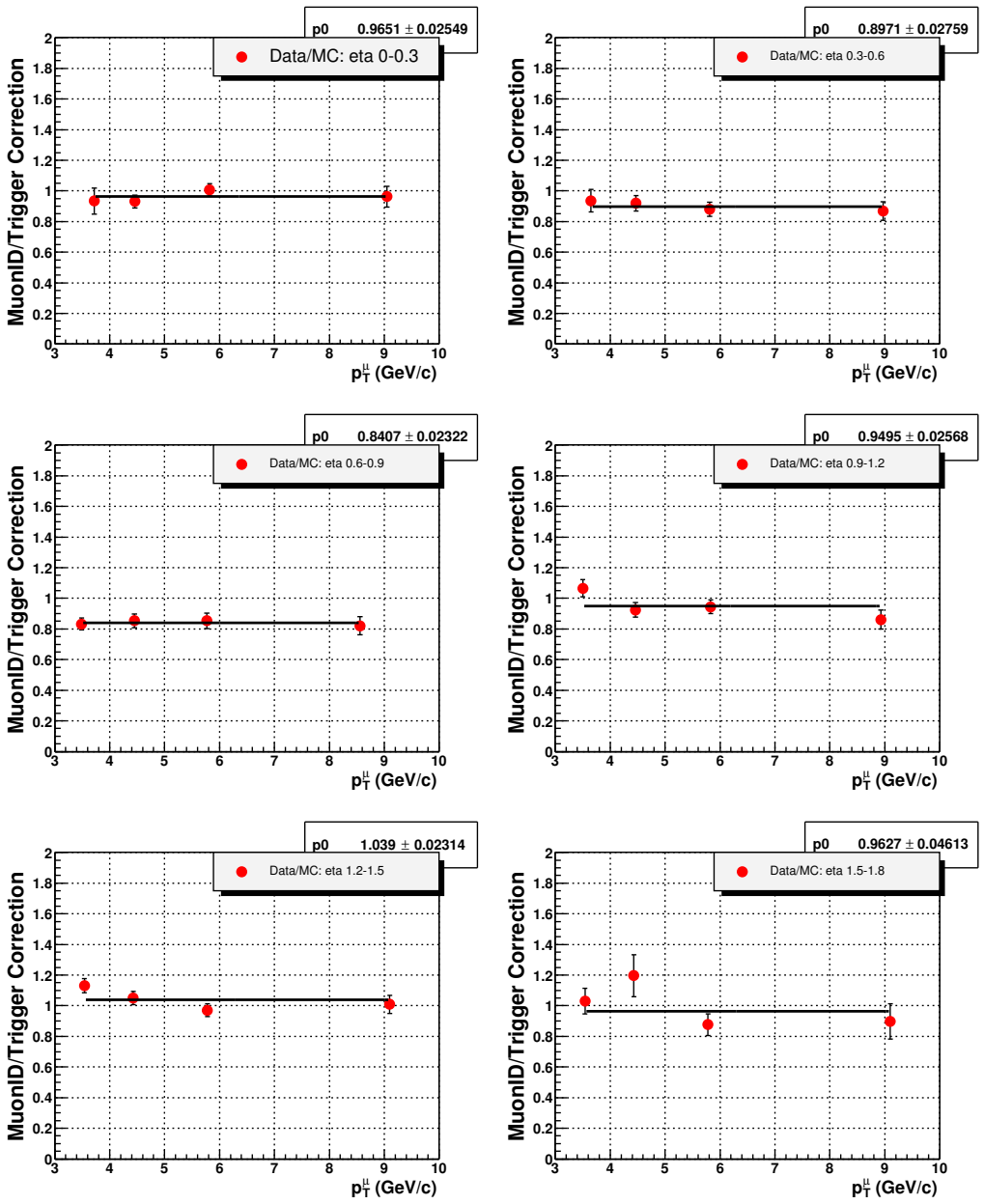

Figure 7.11: Data and Monte Carlo ratio of the local muon-ID and trigger efficiency as a function of muon transverse momentum for different pseudo-rapidity regions.

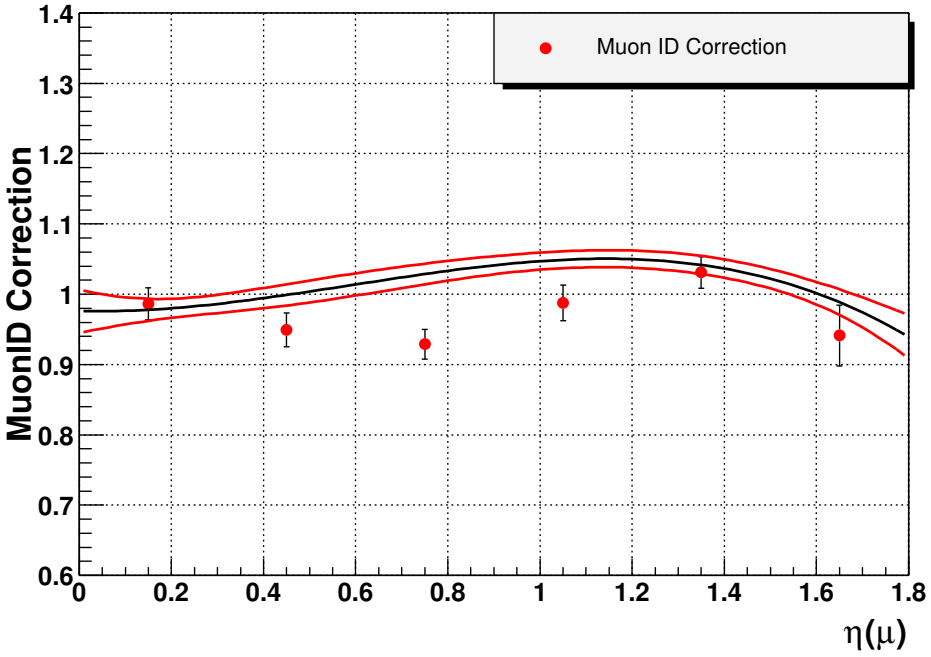

Figure 7.12: Data efficiency divided by Monte Carlo efficiency for the local muon-ID, averaged over p_T as a function of muon pseudo-rapidity. Results of a similar analysis for muons from $Z \rightarrow \mu^+\mu^-$ decays, performed by the top group are shown as lines in the histogram.

with η, with data being less efficient in the central region and Monte Carlo underestimating the efficiency in the forward region. These observations are consistent with the independent top group studies for more energetic muons [64], also shown in Figs. 7.12, in particular for the very central and forward muons.

The combined muon-ID/trigger data Monte Carlo correction exhibits a stronger η dependence, as illustrated in Fig. 7.13. The trigger efficiency factor for this correction is close to unity for the very central and forward muons, but is only 0.91 for muons in the η range (0.6 – 0.9). These corrections are applied to individual muons from $\Upsilon(1S)$ decays using Monte Carlo, assuming these corrections to be:

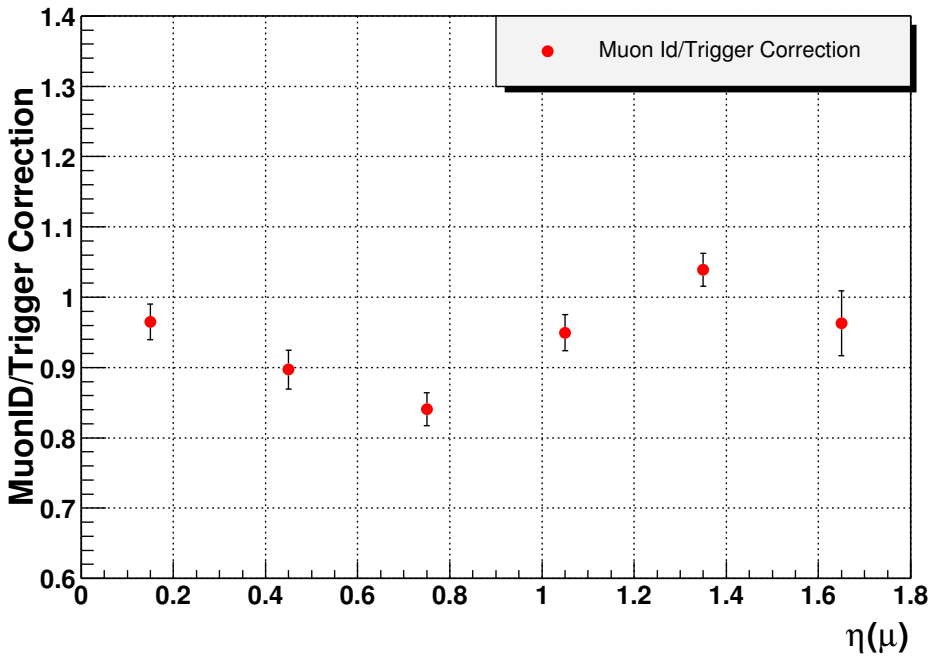

Figure 7.13: Combined data - Monte Carlo corrections for the local muon-ID and trigger efficiency, averaged over p_T as a function of muon pseudo-rapidity.

(i) uncorrelated for muons from different pseudo-rapidity bins in Fig. 7.13;

(ii) 100% correlated otherwise.

The ε_{dimu} correction is calculated as the product of the corrections for individual muons averaged over the muon distributions in a given $\Upsilon(1S)$ kinematic bin. The values of ε_{dimu} vary between 0.85 and 0.93, and therefore increase the measured cross sections by as much as 15%. Approximately half of the ε_{dimu} correction is due to the trigger efficiency alone. This is consistent with the differences in the data - Monte Carlo single muon - dimuon relative trigger efficiencies, discussed in the previous section.

rapidity range	muon ID correction	combined muon ID and trigger correction	estimated trigg. corr.
0.0 – 0.3	0.986 ±0.023	0.965 ±0.025	0.98
0.3 – 0.6	0.949 ±0.024	0.897 ±0.028	0.95
0.6 – 0.9	0.929 ±0.021	0.841 ±0.023	0.91
0.9 – 1.2	0.988 ±0.025	0.950 ±0.026	0.96
1.2 – 1.5	1.03 ±0.023	1.039 ±0.023	1.01
1.5 – 2.2	0.95 ±0.045	0.963 ±0.046	1.01

Table 7.6: Relative data/Monte Carlo correction for local muon ID and combined muon ID trigger efficiencies.

Chapter 8

Results

8.1 Differential Cross Sections

Numerical values of the efficiencies needed for the cross section calculations were discussed in the previous chapter. Typical values of these efficiencies are summarized in Table 8.1 and applied in the three rapidity regions. Figure 8.1 shows the dependence of the overall Monte Carlo derived efficiency on the $\Upsilon(1S)$ transverse momentum. A minimum of the efficiency at intermediate p_T values is understood as a result of changes in topologies for events accepted by the DØ detector. Efficiencies shown in Fig 8.1 do not contain the data derived corrections $\varepsilon_{iso-SMT}, \varepsilon_{dimu}, \varepsilon_{trk}$, and ε_{fit}.

The calculated cross sections are listed in Table 8.2. The cross sections are normalized per unit of rapidity. Cross sections for the $|y^{\Upsilon}| < 1.8$ range were determined in parallel with those for smaller rapidity bins, with every step done separately, including mass fits. Therefore, the fitted number of events for that region is not exactly equal to the sum of signal events fitted in smaller rapidity bins.

The measured cross section $\times$ $BR(\Upsilon(1s) \rightarrow \mu^+\mu^-)$ for the $|y^{\Upsilon}| < 0.6$ region is 749 $\pm$ 20 pb (stat) $\pm$ 75 (syst) $\pm$ 48(*luminosity*) pb and is compatible with the CDF Run I result of 680 $\pm$ 15 (stat) $\pm$ 18 (syst) $\pm$ 26 (luminosity) pb for the $\sqrt{s} = 1.8$ TeV (this value was derived from the information provided in Ref. [14]). The cross sections

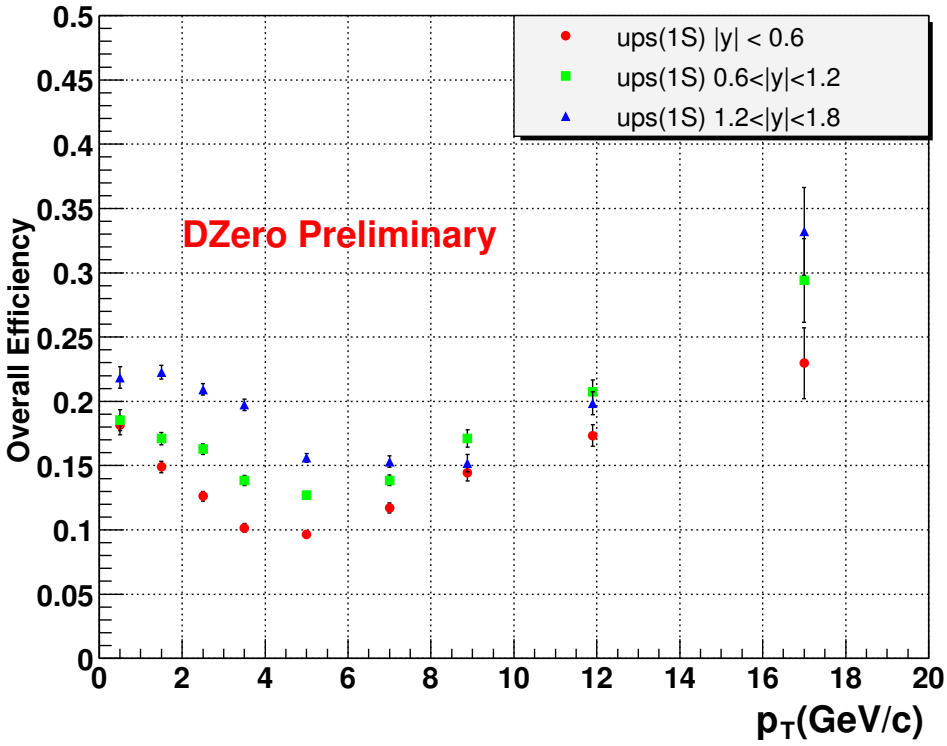

Figure 8.1: Overall efficiency dependence on the upsilon transverse momentum, derived from Monte Carlo and trigger simulator, in three rapidity ranges. Data - Monte Carlo corrections are not included. Minima observed at medium p_T values are associated with the change in event topology. Momenta of accepted decay muons are less symmetric at this $\Upsilon(1S)$ p_T range.

$\lvert\eta^{\Upsilon}\rvert$	ε_{kinem}	ε_{acc}	ε_{trig_reco}	ε_{trk}	ε_{dimu}	ε_{fit}	$\varepsilon_{iso-SMT}$
0.0 – 0.6	0.5 – 0.7	0.3 – 0.4	0.70	0.99	0.85	1.0	0.85
0.6 – 1.2	0.5 – 0.7	0.4 – 0.5	0.73	0.99	0.87	1.0	0.85
1.2 – 1.8	0.4 – 0.6	0.5 – 0.6	0.82	0.95	0.95	1.0	0.93

Table 8.1: Typical efficiencies used for the cross section calculations.

are expected to increase by 11% (PYTHIA Monte Carlo) when the $p\bar{p}$ center-of-mass energy increases from 1.8 TeV to 1.96 TeV.

$\lvert\eta^{\Upsilon}\rvert$	Number of $\Upsilon(1S)$ candidates (SMT+Isolation requirements)	Total cross section (pb)
0.0 – 0.6	13,040	749 ± 20 (stat) ± 75 (syst)
0.6 – 1.2	16,867	781 ± 21 (stat) ± 78 (syst)
1.2 – 1.8	18,122	598 ± 19 (stat) ± 56 (syst)
0.0 – 1.8	46,331	695 ± 12 (stat) ± 65 (syst)

Table 8.2: Fitted number of events for the 2MU-A-L2M0 and 2MU-A-L2ETAPHI triggers.

Differential cross sections as a function of $\Upsilon(1S)(p_T)$, normalized to unity, are summarized in Table 8.3 and plotted in Fig 8.2. There is little variation in the shape of the distributions with rapidity.

p_T^{Υ}	$0.0 < \lvert\eta^{\Upsilon}\rvert < 0.6$	$0.6 < \lvert\eta^{\Upsilon}\rvert < 1.2$	$1.2 < \lvert\eta^{\Upsilon}\rvert < 1.8$	$0.0 < \lvert\eta^{\Upsilon}\rvert < 1.8$
0 – 1	0.050 ± 0.005	0.061 ± 0.006	0.053 ± 0.005	0.057 ± 0.004
1 – 2	0.137 ± 0.009	0.138 ± 0.010	0.135 ± 0.011	0.125 ±0.006
2 – 3	0.153 ± 0.010	0.153 ± 0.010	0.172 ± 0.015	0.160 ± 0.008
3 – 4	0.148 ± 0.011	0.175 ± 0.012	0.166 ± 0.013	0.163 ± 0.008
4 – 6	0.112 ± 0.007	0.110 ± 0.007	0.115 ± 0.007	0.115 ± 0.005
6 – 8	0.067 ± 0.005	0.061 ± 0.004	0.054 ± 0.005	0.063 ± 0.003
8 – 10	0.035 ± 0.003	0.034 ± 0.003	0.035 ± 0.003	0.036 ± 0.002
10 – 15	0.0137 ± 0.001	0.0107 ± 0.0009	0.0110 ± 0.001	0.0118 ± 0.0006
15 – 20	0.0029 ± 0.0005	0.0019 ± 0.0003	0.0016 ± 0.0003	0.00215 ± 0.0002

Table 8.3: Normalized differential cross sections for $\Upsilon(1S)$ in different rapidity regions.

The cross sections integrated over p_T are shown in Fig 8.3 as a function of $|y^{\Upsilon}|$. The ratios of the cross sections in the $0.6 < |y^{\Upsilon}| < 1.2$ and $1.2 < |y^{\Upsilon}| < 1.8$ ranges

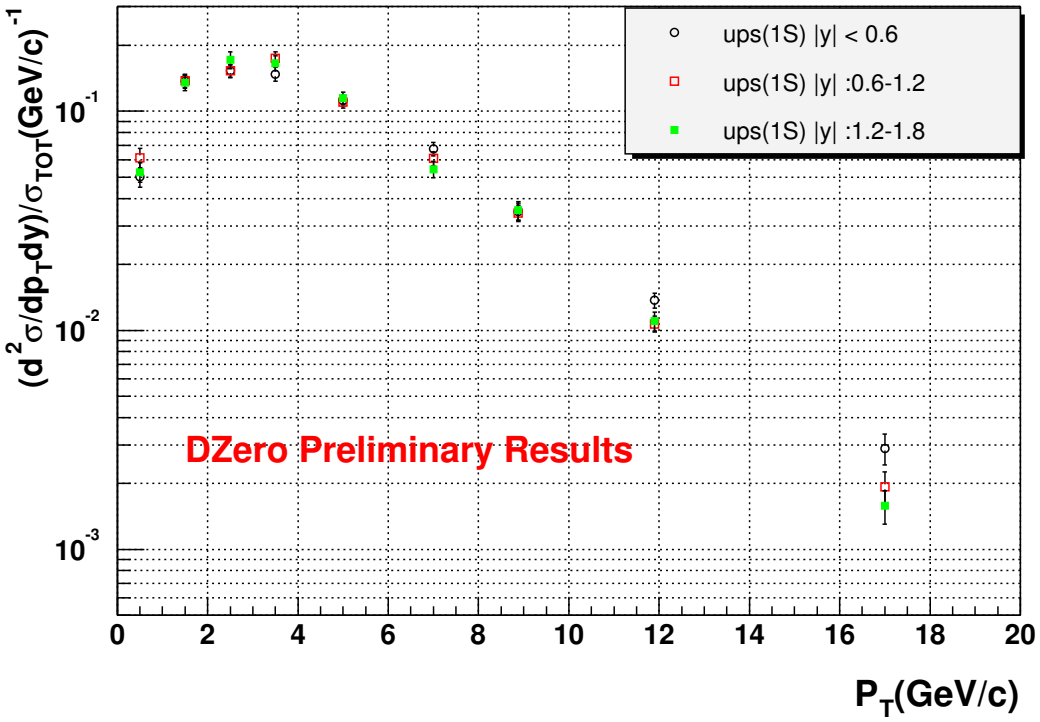

Figure 8.2: Normalized differential cross sections for $\Upsilon(1S)$ in different rapidity regions.

to the one in the $|y^{\Upsilon}| < 0.6$ bin to be: 1.04 $\pm$0.11 and 0.80 $\pm$ 0.09. These values are consistent with the PYTHIA Monte Carlo predictions of 0.94 and 0.83.

Finally, the ratios of differential cross section for different pairs of rapidity bins are shown in Fig 8.4. The systematic uncertainties in the relative normalizations are also indicated.

The overall systematic uncertainties, as discussed in the next section, are approximately 10%.

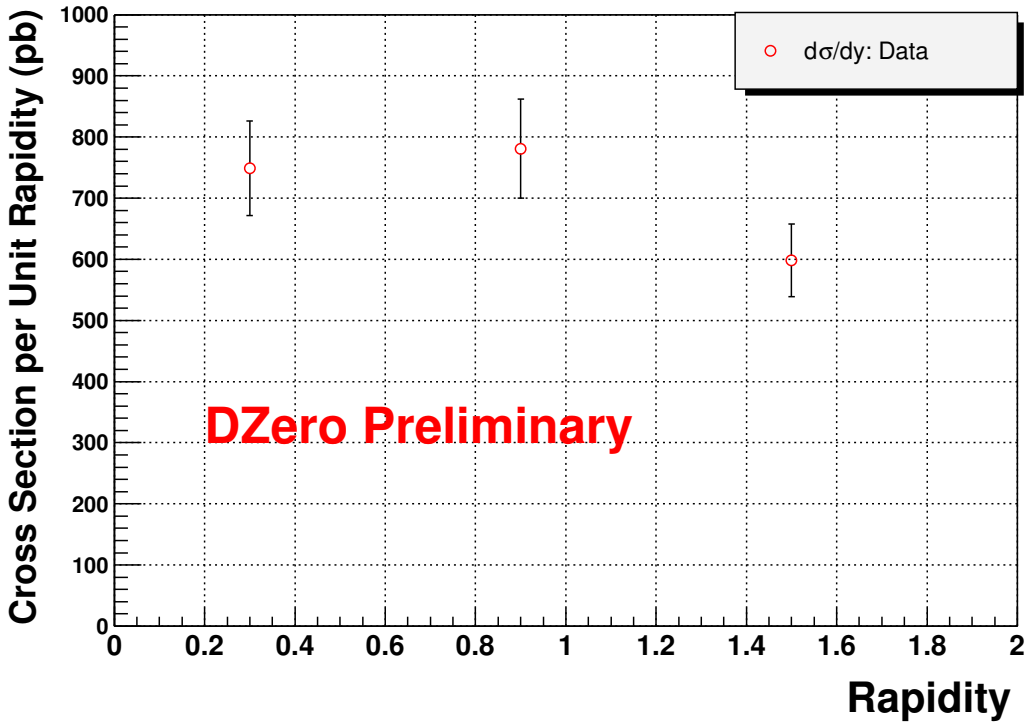

Figure 8.3: $\Upsilon(1S)$ production cross section per unit of rapidity.

8.2 Systematic Uncertainties

In this analysis we are concerned with systematic uncertainties that are p_T dependent and with those that are common and affect the absolute normalization of the cross sections. We estimated the effects of the mass resolution function uncertainty on the fit bin-to-bin variations by doubling the contribution of the second Gaussian term. The difference in the number of fitted $\Upsilon(1S)$ candidates was added in quadrature to the regular fit uncertainties. The net effect is an increase in the overall fit uncertainty by less than 4% of its original value.

The remaining systematic uncertainties have a minimal effect on the $\Upsilon(1S)$ p_T. All of the systematic uncertainties have been identified and listed in Table 8.4:

(i) The nominal uncertainty for the luminosity is 6.5%.

(ii) The uncertainty on the kinematic (pre-Geant) efficiency, ε_{kinem}, was obtained by varying the hard scatter *PTLOW* parameter in PYTHIA and is found to be negligible.

(iii) Common systematic uncertainties of ε_{fit} were estimated from: (a) a comparison of numbers of fitted events with the resolution function width either treated as a fit parameter or fixed and from variations in the mass fit range, (b) number of events obtained using either single- or double-Gaussian resolution functions and (c) varying the mass fit range by $\pm$ 0.2 GeV.

(iv) Systematic uncertainties of $\varepsilon_{iso-SMT}$ were estimated from the mass fits for the combined $\Upsilon(nS)$ signal, with and without muon quality requirements.

(v) The uncertainty of the ε_{acc} efficiency was obtained by re-weighting Monte Carlo events so that they match $\Upsilon(1S)$ differential cross sections determined in the first pass. The p_T dependence for this weight is shown in Fig 8.5. The only significant

change of efficiency was observed for the last two, 5 GeV/c wide, p_T bins, and it was less than 3%.

(vi) The largest contribution to the systematic uncertainty is due to ε_{dimu}, representing the differences between the local muon ID and trigger efficiencies obtained from data and Monte Carlo. This systematic uncertainty reflects: (a) limited statistics of the control data and Monte Carlo samples, (b) variations in the conditions under which these corrections were studied, such as: selection cuts for the trigger and test muons, J/ψ signal fits, composition of the J/ψ Monte Carlo, detector symmetries etc. Statistical and systematic uncertainties, determined as functions of kinematic variables for individual muons were added in quadrature and propagated into the uncertainty for ε_{dimu} using Monte Carlo. Our very conservative estimates for these uncertainties are 8.7, 8.2, and 7.2% for the three rapidity bins, respectively.

Source	$0.0 < \lvert\eta^{\Upsilon}\rvert < 0.6$	$0.6 < \lvert\eta^{\Upsilon}\rvert < 1.2$	$1.2 < \lvert\eta^{\Upsilon}\rvert < 1.8$
Luminosity	6.5%	6.5%	6.5%
fitting procedure	3.0%	4.0%	4.0%
isolation, SMT hit requir.	2.0%	2.0%	1.7%
MC kinematic properties	<2.0%	<2.0%	<2.0%
momentum resolution	<1%	<1%	<1%
central track matching	2.0%	2.0%	3.0%
local μ ID and trigger	8.7%	8.2%	7.2%
detector performance vs time	2.0%	2.0%	2.0%
TOTAL (no lum, polarization)	10.0%	10.0%	9.4%

Table 8.4: Dominant systematic uncertainties.

Statistical uncertainties from the fits shown in Fig 7.11 and quoted in Table 7.6 contribute 3.7%, 3.8% and 5.4%, respectively. However, if one makes corrections independently for the $3 < p_T < 4$ GeV/c and $p_T > 4$ GeV/c muons, using numbers

listed in Tables 7.4 and 7.5, the systematic uncertainties increase to 5.0, 5.1, and 6.0%. The values of the cross sections change by less than 1%.

(vii) The uncertainty of ε_{trk}, the tracking data-Monte Carlo correction, contributes less than 2%.

(viii) The uncertainty due to the finite momentum resolution was estimated by comparing the numbers of reconstructed Monte Carlo events, assigned to a given $\Upsilon(1S)$ kinematic bin, with either original or smeared muon momenta used.

(ix) Uncertainties due to variations in the detector performance were studied by plotting the number of signal events per luminosity versus time. We discovered that the data taken with the Level 1 trigger *mu2ptxatxx-fz* rather than *mu2ptxatxx* (runs before 173516 , first 52 pb^{-1} of data) have 12% lower event rate. After correcting for this loss and removing double events the yield of observed $\Upsilon(nS)$ candidates per pb^{-1} is fairly constant, as illustrated in Fig. 8.6.

(x) This analysis was done assuming that $\Upsilon(1S)$ are produced unpolarized. The acceptance variation due to the $\Upsilon(1S)$ polarization is asymmetric, and depends on the $\Upsilon(1S)$ p_T and rapidity. It varies from -15% to $+40\%$ for the extreme cases of either pure transverse or longitudinal polarization (see Fig. 8.7). Although we do not include a contribution to the systematic uncertainties due to this assumption, we estimate the sensitivity of our results to the $\Upsilon(1S)$ polarization by varying the polarization parameter α within ± 0.15 (± 0.30). This changes our results by less than 4% (15%) over the whole p_T range as shown in Fig. 8.8.

In our earlier studies of $\Upsilon(1S)$ polarization, we fitted the α parameter to be -0.11 ± 0.16 (stat) for $p_T^{\Upsilon} > 8$ GeV/c. The method and result are discussed in next appendix B.

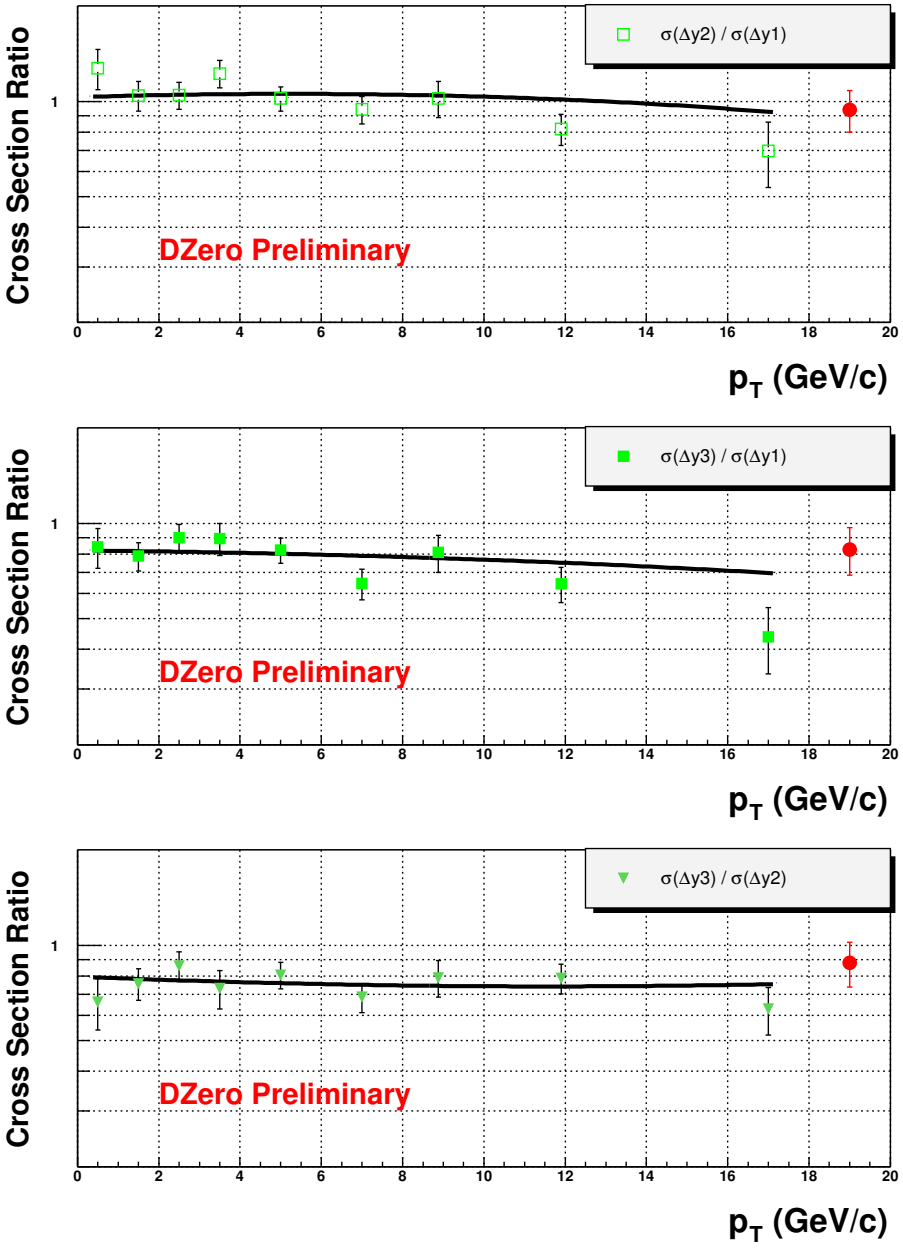

Figure 8.4: Ratios of $\Upsilon(1S)$ cross sections for different rapidities as a function of $\Upsilon(1S)$ transverse momentum.

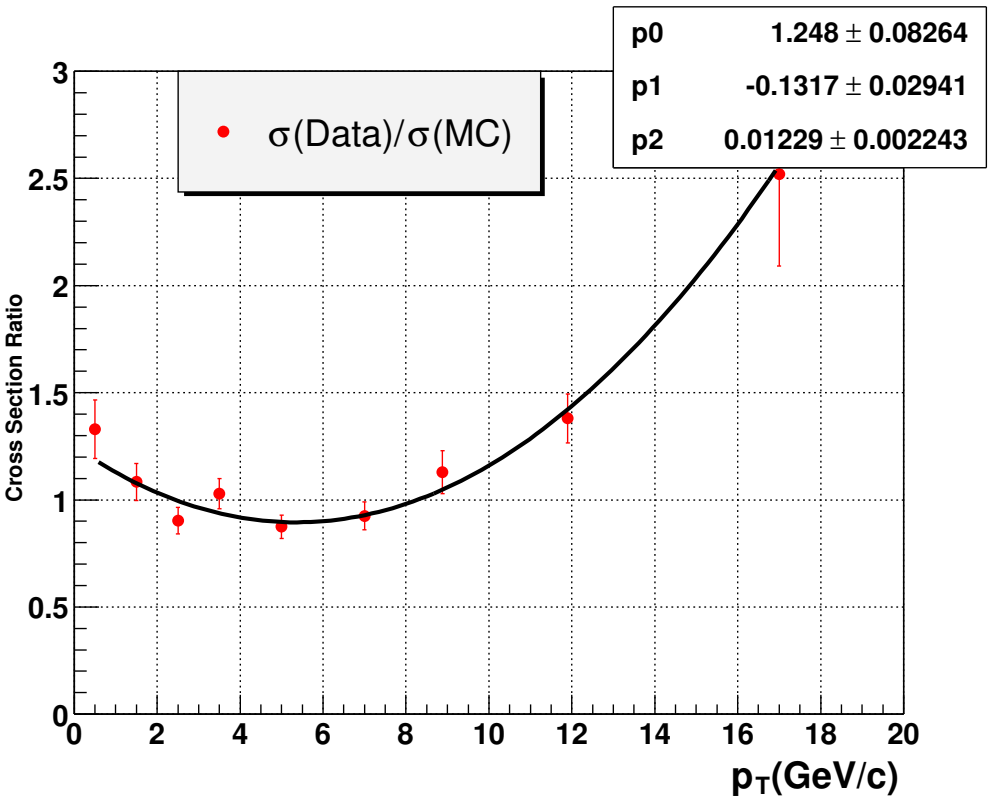

Figure 8.5: Ratio of normalized $\Upsilon(1S)$ differential cross sections, data over PYTHIA Monte Carlo.

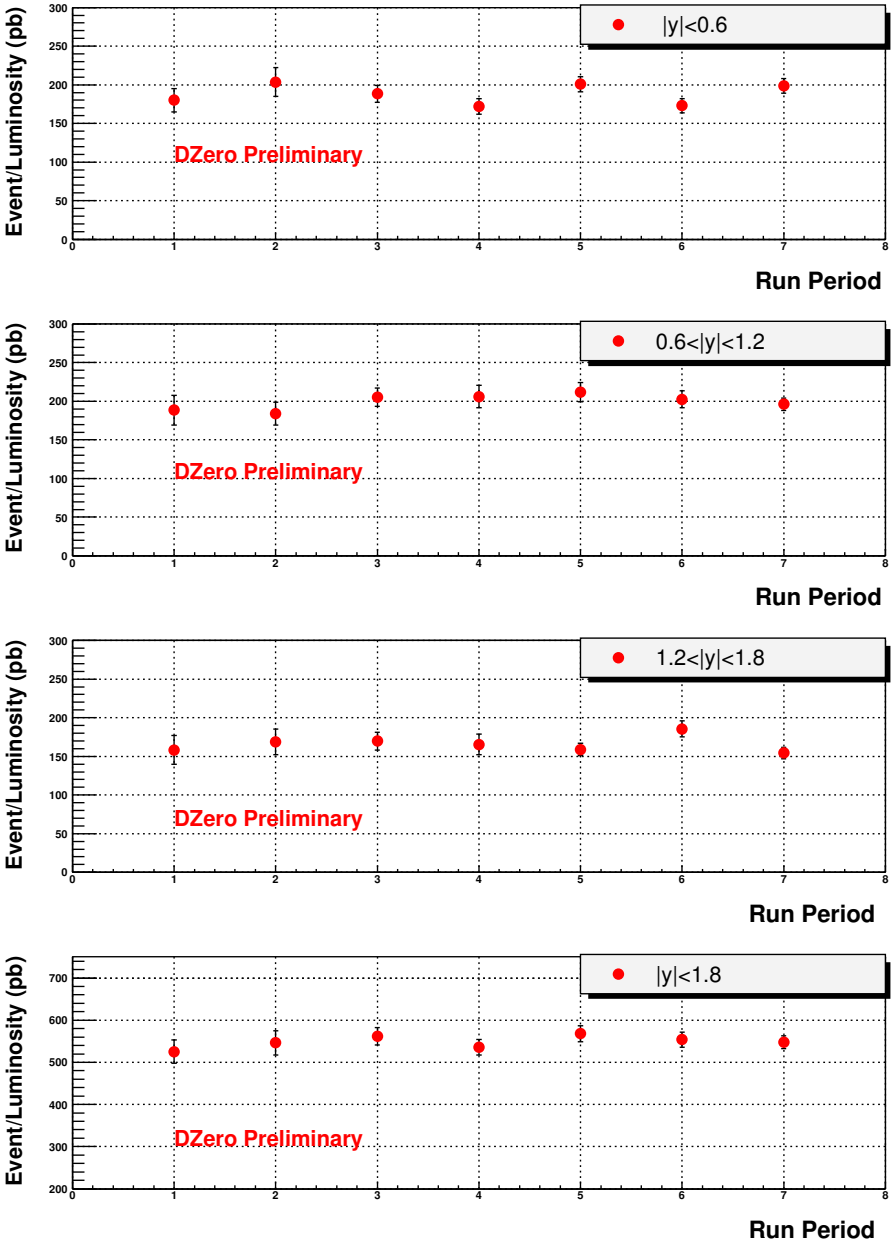

Figure 8.6: Number of fitted $\Upsilon(nS)$ events per luminosity for 7 data taking periods.

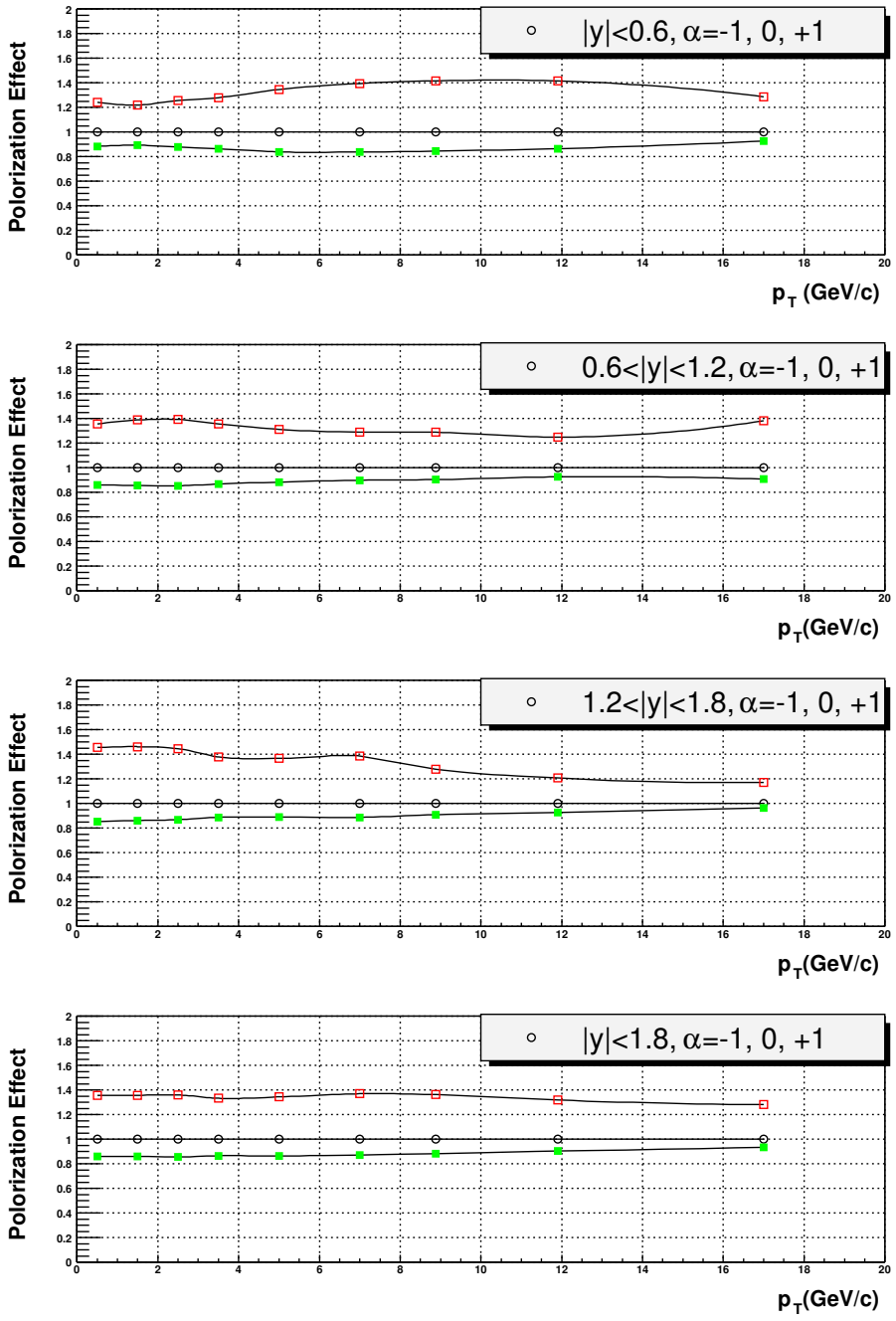

Figure 8.7: Expected variations of $\varepsilon_{kinem} \cdot \varepsilon_{acc} \cdot \varepsilon_{trig-reco}$ corresponding to cases of pure of $\Upsilon(1S)$ polarization.

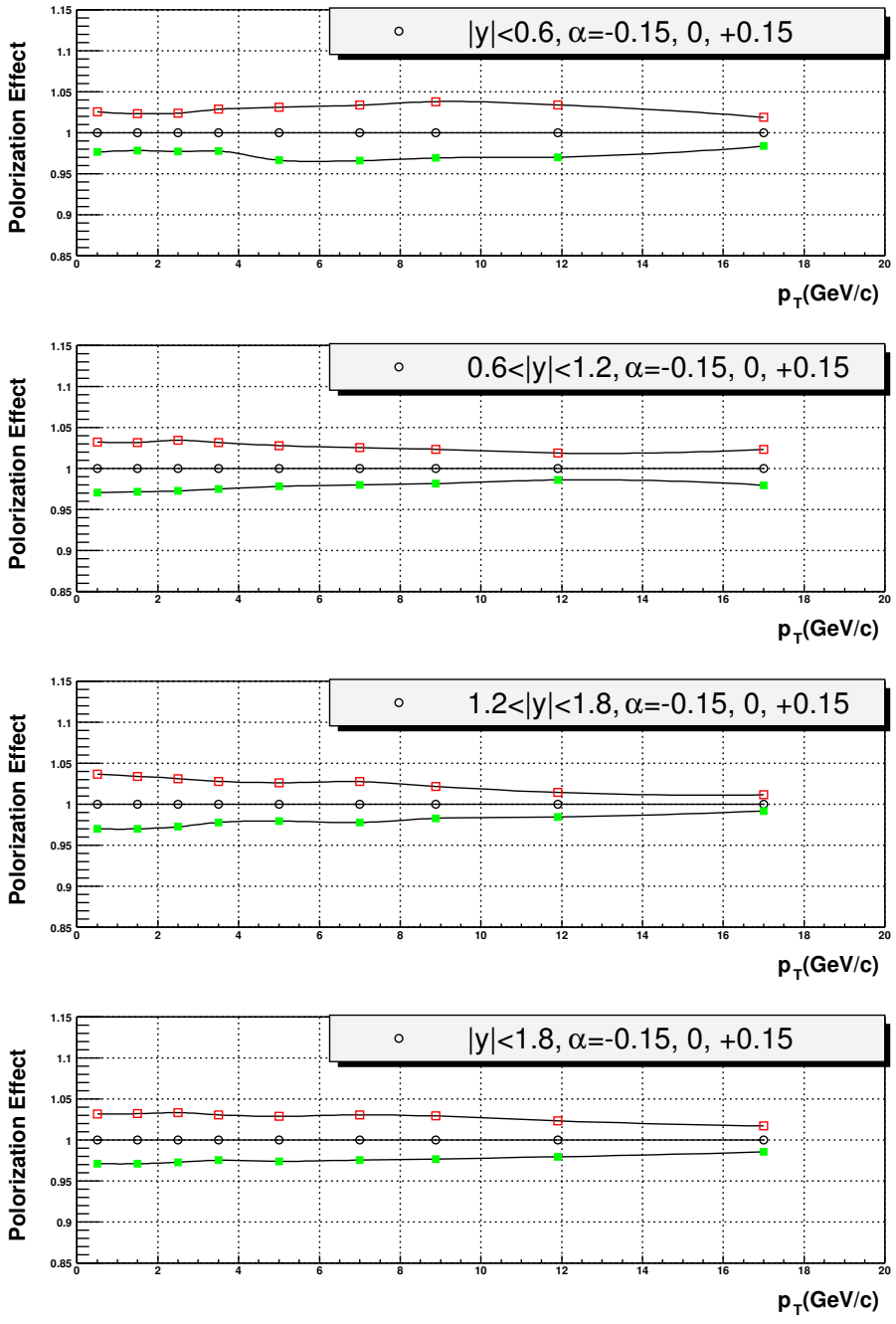

Figure 8.8: Expected variations of $\varepsilon_{kinem} \cdot \varepsilon_{acc} \cdot \varepsilon_{trig-reco}$ corresponding to variations of the polarization parameter α within ± 0.15 plotted as a function of $\Upsilon(1S)$ transverse momentum for three rapidity regions. The plotted ratios are calculated with respect to the unpolarized $\Upsilon(1S)$ production.

Chapter 9

Conclusions

In this thesis, the author describes the service work he has done for the DØ experiment and the physics analysis of the inclusive production cross section of the $\Upsilon(1S)$ bottomonium state using the $\Upsilon(1S) \rightarrow \mu^+\mu^-$ decay mode.

The service work includes: (i) being a DAQ shifter, (ii) the alignment of the muon subsystems, and (iii) the design and implementation of the muon online and offline calibration databases.

The data sample used in the physics analysis corresponds to an integrated luminosity of 159.1 $\pm$ 10.3 pb^{-1}. The differential cross sections are determined as functions of the $\Upsilon(1S)$ transverse momentum, p_T^{Υ}, for three ranges of the $\Upsilon(1S)$ rapidity: $0 < |y^{\Upsilon}| < 0.6, 0.6 < |y^{\Upsilon}| < 1.2$ and $1.2 < |y^{\Upsilon}| < 1.8$. The shapes of $d\sigma/dp_T$ cross sections show little variation with rapidity. As shown in Fig. 9.1, our combined differential cross section for $|y^{\Upsilon}| < 1.8$ is consistent with the published CDF Run I measurement in the limited rapidity range of $|y^{\Upsilon}| < 0.4$. The theoretical curves [67] of $\Upsilon(1S)$ normalized differential cross sections produced by E. Berger at Argonne National Lab for $|y^{\Upsilon}| < 0.6$, $0.6 < |y^{\Upsilon}| < 1.2$ and $1.2 < |y^{\Upsilon}| < 1.8$ are shown in Fig. 9.2. In the future, with more and more data available, it will be possible to extend this analysis to measure the polarization of the $\Upsilon(1S)$ accurately.

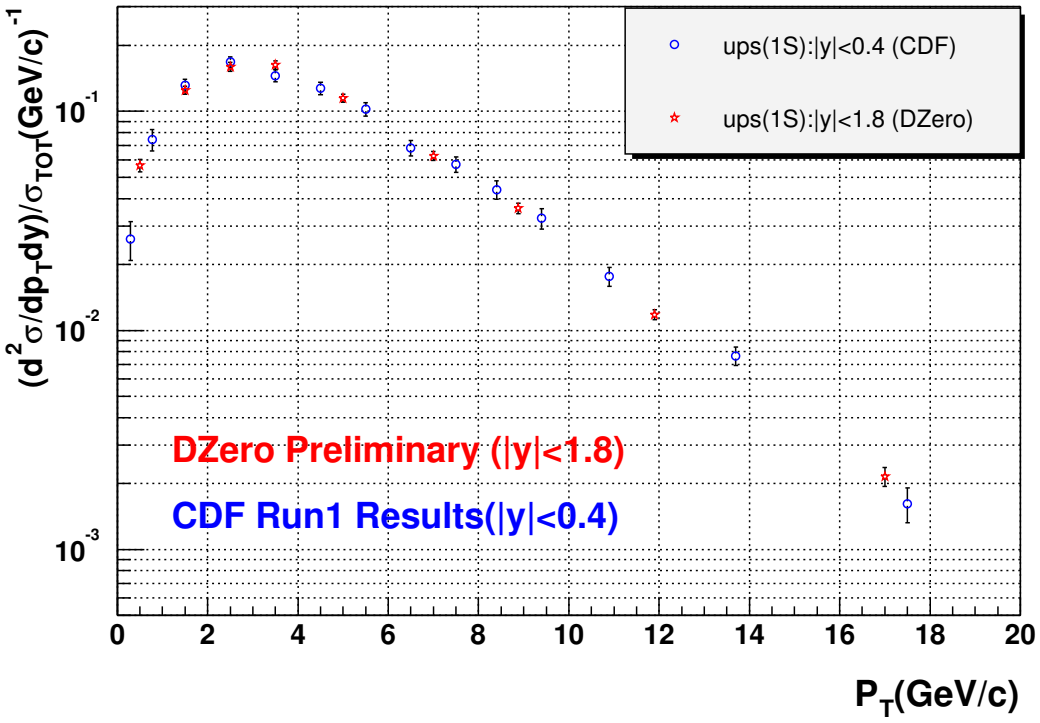

Figure 9.1: Normalized differential cross sections for $\Upsilon(1S)$ compared with the published CDF Run I results.

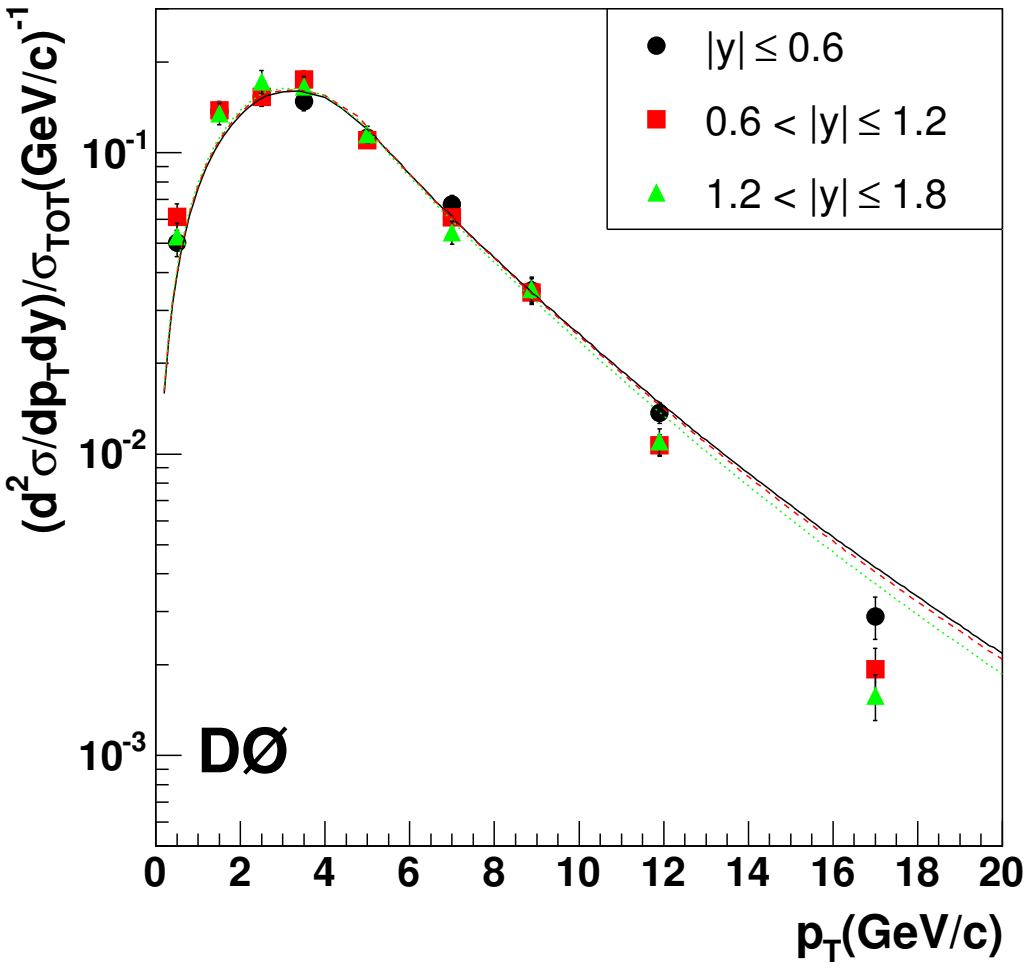

Figure 9.2: Normalized differential cross sections for $\Upsilon(1S)$ compared with theory predictions [21, 67]. The theory curves correspond to $|y^{\Upsilon}| < 0.6$ (solid line), $0.6 < |y^{\Upsilon}| < 1.2$ (dashed line) and $1.2 < |y^{\Upsilon}| < 1.8$ (dotted line).

Appendix A

Early Run II J/ψ Production Results

During summer of 2002, we studied [1] the J/ψ production cross section using data collected by DØ from February to May 2002. The integrated luminosity of the data sample used is $\sim$4.74 pb^{-1}. The results of this analysis are summarized in this section. The details of this analysis are described in Ref [15].

In this study, we determine the J/ψ production cross section for two transverse momentum ranges, $p_T^{J/\psi} > 5$ GeV/c and $p_T^{J/\psi} > 8$ GeV/c, each in five different rapidity regions within the $|y^{J/\psi}| < 1.8$ range.

The cross sections for a given kinematic range is given by:

$$\sigma(J/\psi) = \frac{N(J/\psi)}{\mathcal{L} \cdot \varepsilon_{pre-geant} \cdot \varepsilon_{acceptance} \cdot \varepsilon_{trigger} \cdot \varepsilon_{dimureco} \cdot \varepsilon_{trkmatch}}, \tag{A.1}$$

where $\mathcal{L}$ is the integrated luminosity of the data sample; $N(J/\psi)$ is the number of fitted J/ψ events; ε_i represent various efficiency and acceptance factors. The muon acceptance and reconstruction efficiency is based on the Monte Carlo analysis and has been factorized into two parts: losses due to kinematic cuts on muon momenta before the Monte Carlo events were processed through the simulation/reconstruction packages ($\varepsilon_{pre-geant}$), and an acceptance/reconstruction efficiency for muons that had a chance to be reconstructed ($\varepsilon_{acceptance}$). The factor ($\varepsilon_{dimureco}$) accounts for the

[1] The analysis was a joint work of Prof. Andrzej Zieminski, Dr. Chunhui Luo and the author; The author contributed in the signal events fits, efficiency studies of $\varepsilon_{pre-geant}$,$\varepsilon_{acceptance}$ and $\varepsilon_{trkmatch}$.

differences in the muon reconstruction efficiency between the Monte Carlo and the data. The dimuon trigger efficiency ($\varepsilon_{trigger}$) for reconstructed dimuons was estimated by running a trigger simulator, and, independently,directly from the data using single muon triggers with known prescale factors. The central track matching efficiency ($\varepsilon_{trkmatch}$) was derived from the data. The values of the efficiencies and cross sections are collected in Table A.1.

Kinem. Region	Nevents	$\varepsilon_{pre-geant}$	$\varepsilon_{acceptance}$	$\varepsilon_{trkmatch}$	$\varepsilon_{dimureco}$	$\varepsilon_{trigger}$	σ(nb)
$p_T^{J/\psi} > 5$ GeV							
$\|y\| < 0.6$	163 ± 21	0.10 ± 0.02	0.13 ± 0.01	0.75 ± 0.03	0.51 ± 0.10	0.49 ± 0.07	11.7 ± 4.0
$0.6 < \|y\| < 0.9$	177 ± 21	0.17 ± 0.02	0.11 ± 0.01	0.73 ± 0.03	0.62 ± 0.08	0.57 ± 0.06	13.0 ± 3.5
$0.9 < \|y\| < 1.2$	643 ± 40	0.25 ± 0.02	0.17 ± 0.01	0.71 ± 0.03	0.70 ± 0.06	0.71 ± 0.04	15.0 ± 2.1
$1.2 < \|y\| < 1.5$	1121 ± 48	0.33 ± 0.03	0.22 ± 0.01	0.55 ± 0.02	0.86 ± 0.07	0.76 ± 0.03	15.3 ± 2.1
$1.5 < \|y\| < 1.8$	518 ± 31	0.20 ± 0.03	0.33 ± 0.02	0.25 ± 0.01	0.92 ± 0.07	0.84 ± 0.03	14.4 ± 2.9
$p_T^{J/\psi} > 8$ GeV							
$\|y\| < 0.6$	139 ± 23	0.36 ± 0.03	0.16 ± 0.02	0.77 ± 0.03	0.51 ± 0.10	0.53 ± 0.06	2.11 ± 0.66
$0.6 < \|y\| < 0.9$	99 ± 16	0.39 ± 0.03	0.18 ± 0.02	0.75 ± 0.03	0.62 ± 0.08	0.59 ± 0.07	1.86 ± 0.54
$0.9 < \|y\| < 1.2$	309 ± 28	0.51 ± 0.04	0.24 ± 0.03	0.75 ± 0.03	0.72 ± 0.06	0.77 ± 0.05	2.11 ± 0.42
$1.2 < \|y\| < 1.5$	417 ± 28	0.53 ± 0.06	0.25 ± 0.03	0.56 ± 0.02	0.88 ± 0.07	0.85 ± 0.04	2.66 ± 0.48
$1.5 < \|y\| < 1.8$	138 ± 17	0.38 ± 0.04	0.25 ± 0.04	0.26 ± 0.01	0.92 ± 0.07	0.91 ± 0.04	2.35 ± 0.55

Table A.1: Summary of J/ψ cross-section calculations

The cross sections are shown in Fig. A.1. Quoted cross sections are normalized per unit of rapidity. The overall systematic uncertainty is $\sim$30%, and is not shown in the plot. The CDF Run I measurement in the limited rapidity range of $|y^{J/\psi}| < 0.6$ [65] is also plotted for comparison. Our results are consistent with CDF Run I measurement. The measured cross sections do not exhibit a significant rapidity dependence, which is in agreement with theoretical predictions [66].

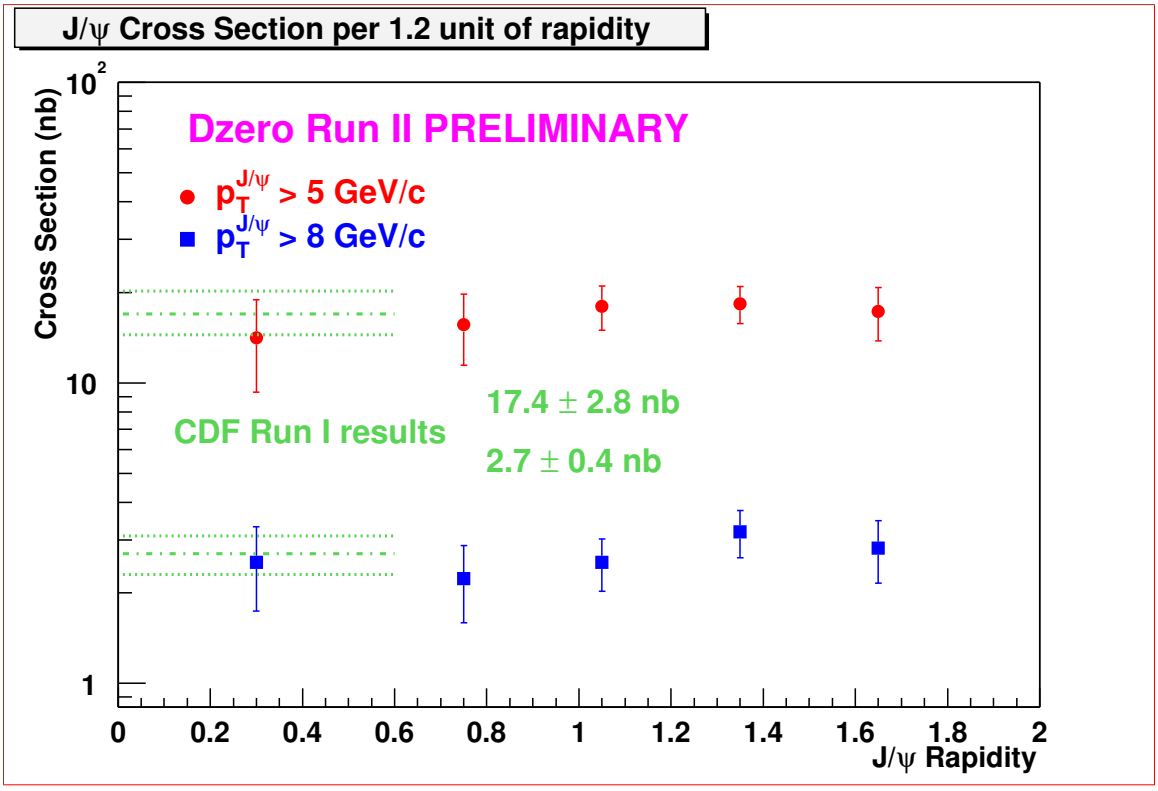

Figure A.1: J/ψ production cross section per 1.2 unit of rapidity.

Appendix B

Polarization Study (Summer 2003)

The non-relativistic QCD (NRQCD) [20] leads to the prediction that $\Upsilon(1S)$ produced will be increasingly transversely polarized at high p_T (see Fig. 2.2). On the other hand, the color evaporation model (CEM) predicts an absence of polarization. Using data and Monte Carlo reconstructed in early 2003, i.e., before the major improvements in tracking mentioned in Section 7.3.4, we studied the polarization of $\Upsilon(1S)$. The results are presented in this section.

Since the $\Upsilon(nS)$ is a spin-1 particle, the projection λ of its spin along any quantization axis should be $-1, 0, +1$. The polarization of the $\Upsilon(nS)$ can be measured from the angular distribution of the leptons from its leptonic decays. The angular distribution for $\Upsilon(1S) \to \mu^+\mu^-$ is defined as

$$I(\theta) = \frac{3}{2(\alpha+3)}(1 + \alpha\cos^2\theta),$$

where θ is the angle between the μ^+ from $\Upsilon(1S)$ decay in the $\Upsilon(1S)$ rest frame with respect to the direction of $\Upsilon(1S)$ in the lab frame. We take the $\Upsilon(1S)$ momentum in this frame to be the spin quantization axis and the longitudinally polarized $\Upsilon(1S)$ to be the $\lambda = 0$ state. The parameter α describes the $\Upsilon(1S)$ polarization: $\alpha = +1$ corresponds to transverse polarization and $\alpha = -1$ to longitudinal polarization.

The polarization parameter α can be defined as:

$$\alpha = \frac{\sigma_T - 2\sigma_L}{\sigma_T + 2\sigma_L}, \tag{B.1}$$

where σ_T is the inclusive cross section for transversely polarized $\Upsilon(1S)$ and σ_L is the

inclusive cross section for longitudinally polarized $\Upsilon(1S)$.

B.1 The Method

The method used is as follows:

- Find the $\cos\theta$ distribution from Monte Carlo;
- Adjust MC to reproduce the observed $\Upsilon(1S)$ p_T and η spectra;
- Produce templates by weighting the MC events with $\alpha = +1$ and $\alpha = -1$;
- Choose eight $\cos\theta$ bins:
  $\cos\theta$: $< 0.1, 0.1-0.2, 0.2-0.3, 0.3-0.4, 0.4-0.5, 0.5-0.6, 0.6-0.8, 0.8-1.0$;
- Determine the number of $\Upsilon(nS)$ events in the each $\cos\theta$ bin;
- Fit the data to the combinations of longitudinally and transversely polarized MC templates: data = f * MC($\alpha = +1$) + (1-f) * MC($\alpha = -1$), where the free parameter f is the fraction of the transversely polarized $\Upsilon(1S)$. The relation between f and α derived from Eq. B.1 is

$$\alpha = \frac{3f-2}{2-f}.$$

B.2 The Result

The $\cos\theta$ disttribution for data and longitudially and transversely polarized $\Upsilon(1S)$ is shown in Fig. B.1. Our measurements are consistent with unpolarized $\Upsilon(1S)$ production. In the transverse momentum region $8 \leq p_T \leq 16$ GeV/c, the longitudinal

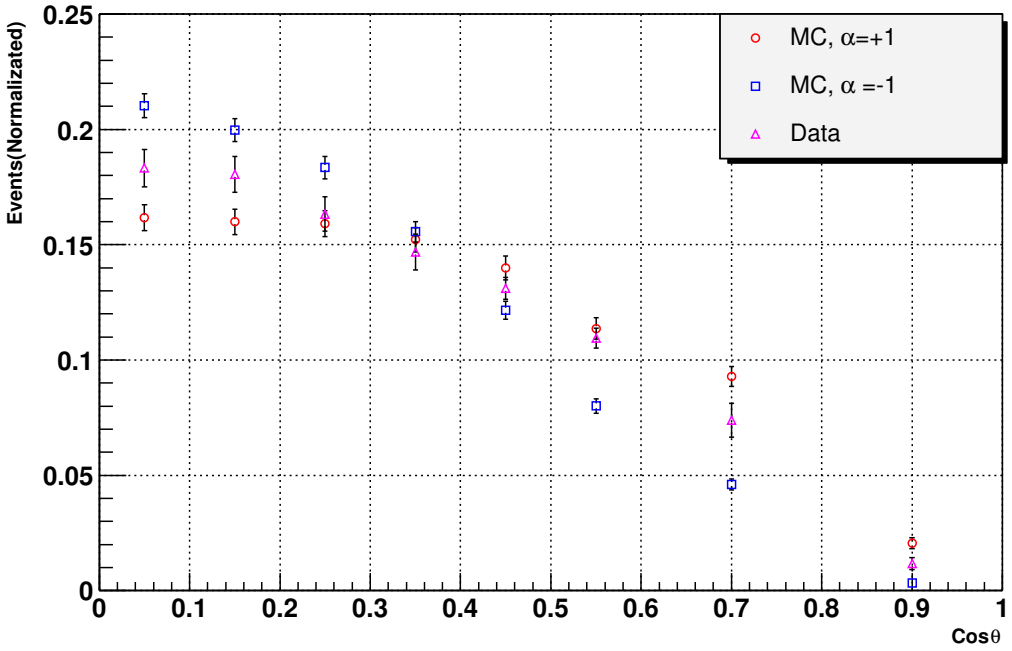

Figure B.1: The $\mu^+ \cos\theta$ distribution for $|y^\Upsilon| < 1.8$ and $8.0 < p_T^\Upsilon < 16.0$ GeV/c with longitudinally and transversely polarized Monte Carlo templates.

fraction is measured to be $f = 0.62 \pm 0.09$, which yields $\alpha = -0.11 \pm 0.16$. This result is in agreement with the the CDF Run I measurement of $\alpha = -0.12 \pm 0.22$ and the polarization calculated using the NRQCD factorization framework ($\alpha = 0.13 \pm 0.18$) which predicts transverse polarization only for an average $p_T(\Upsilon) \gg M(\Upsilon)$.

Appendix C

Dimuon Mass fit plots

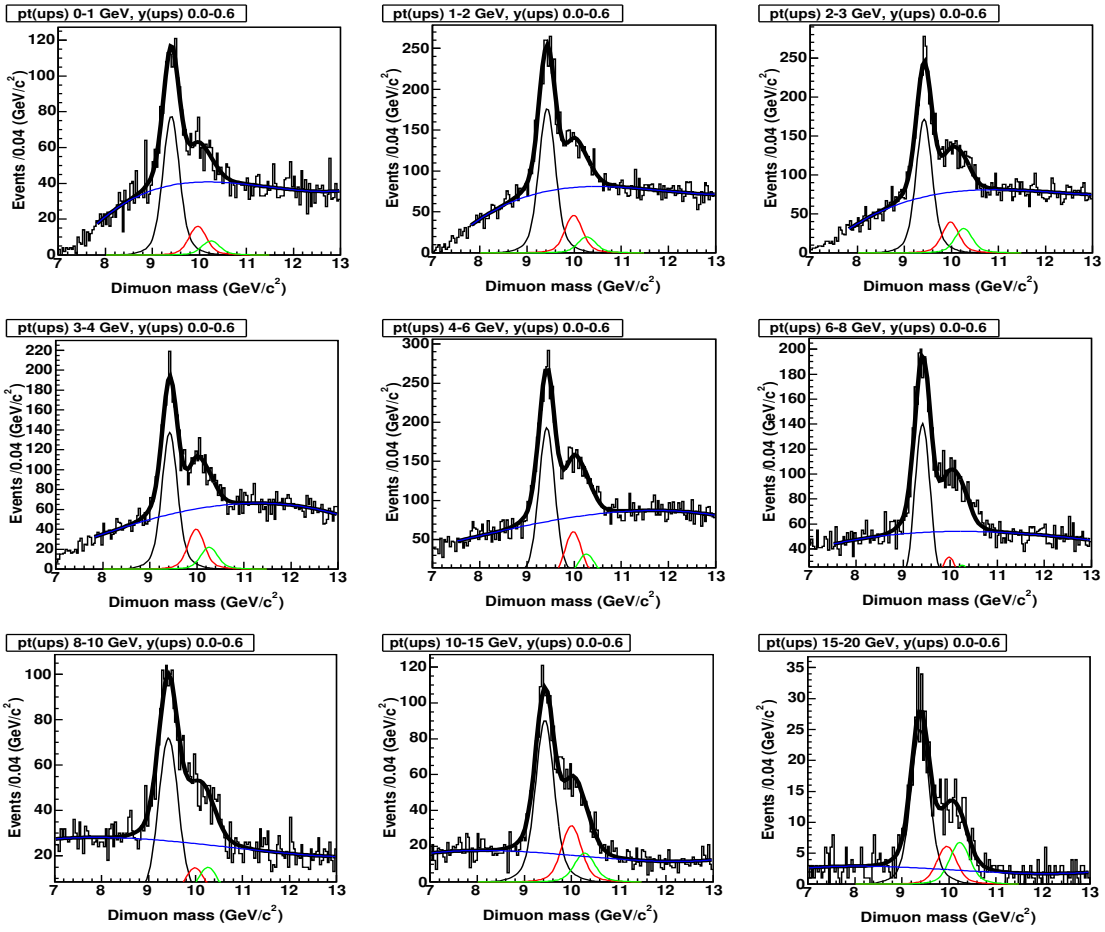

Figure C.1: Fits for the dimuon spectra in different bins of transverse momentum for $\Upsilon(1S)$ rapidity range 0.0 – 0.6.

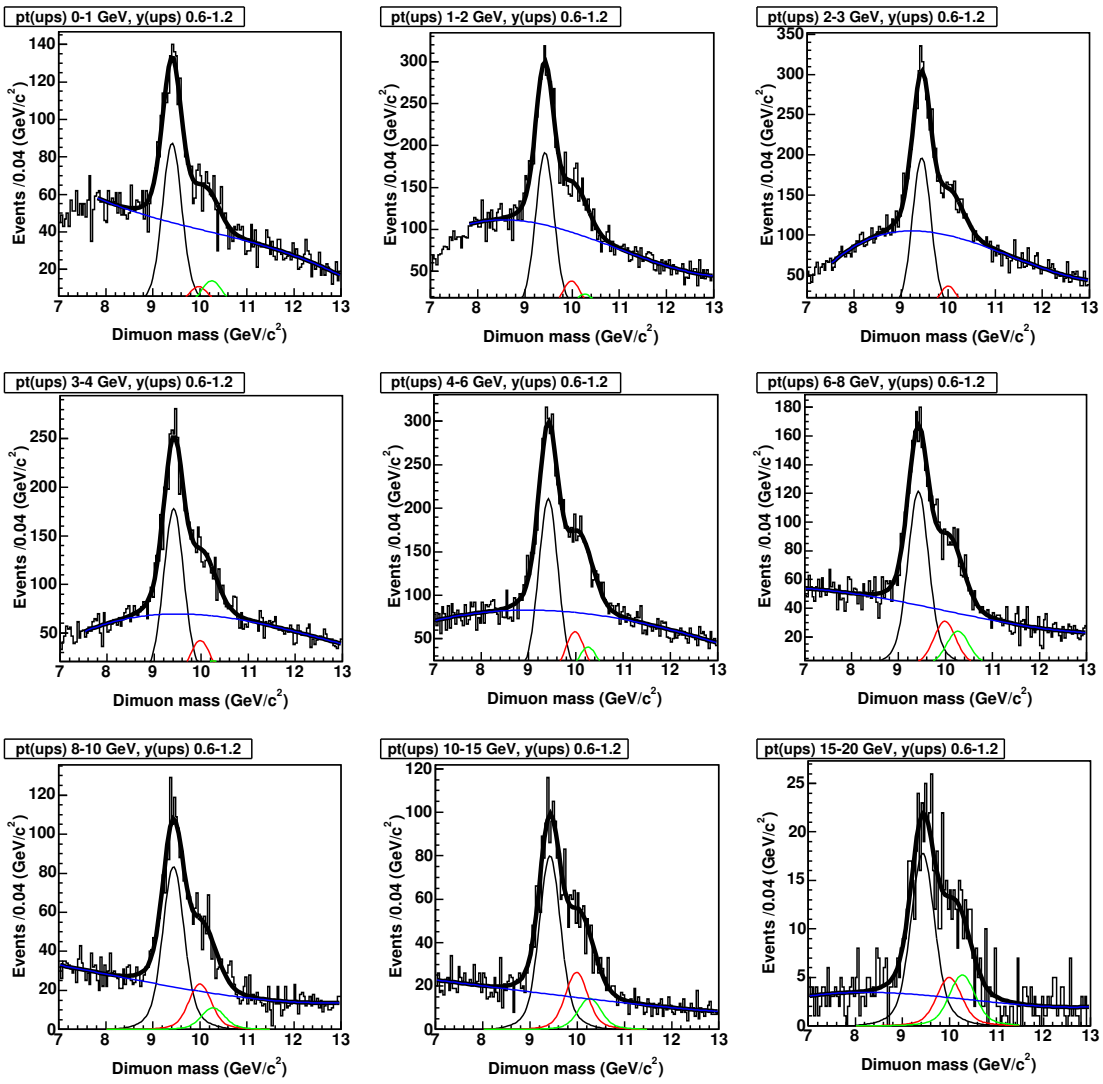

Figure C.2: Fits for the dimuon spectra in different bins of transverse momentum for $\Upsilon(1S)$ rapidity range 0.6 – 1.2.

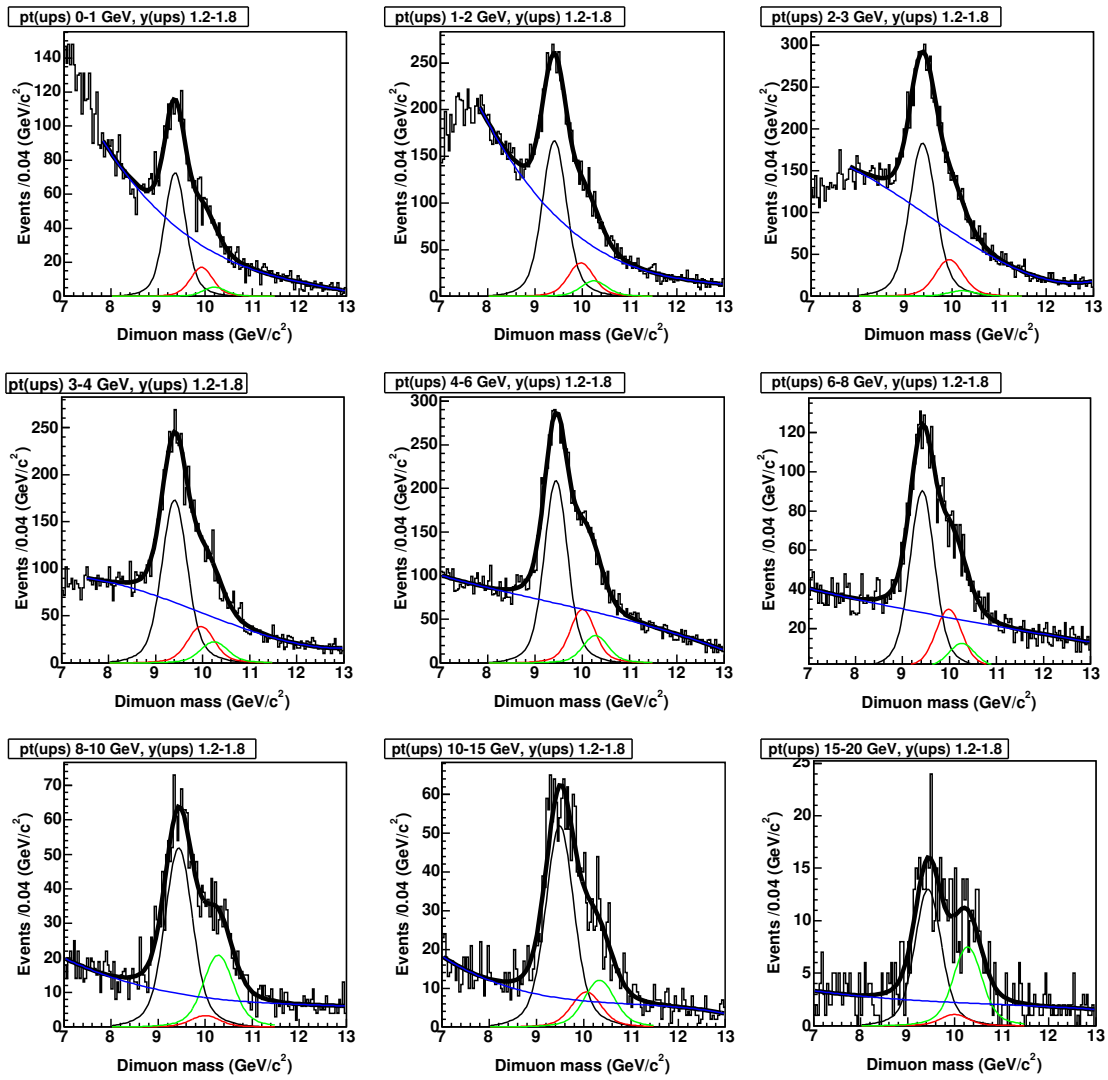

Figure C.3: Fits for the dimuon spectra in different bins of transverse momentum for $\Upsilon(1S)$ rapidity range 1.2 – 1.8.

Appendix D

Database designs for MDT and MSC

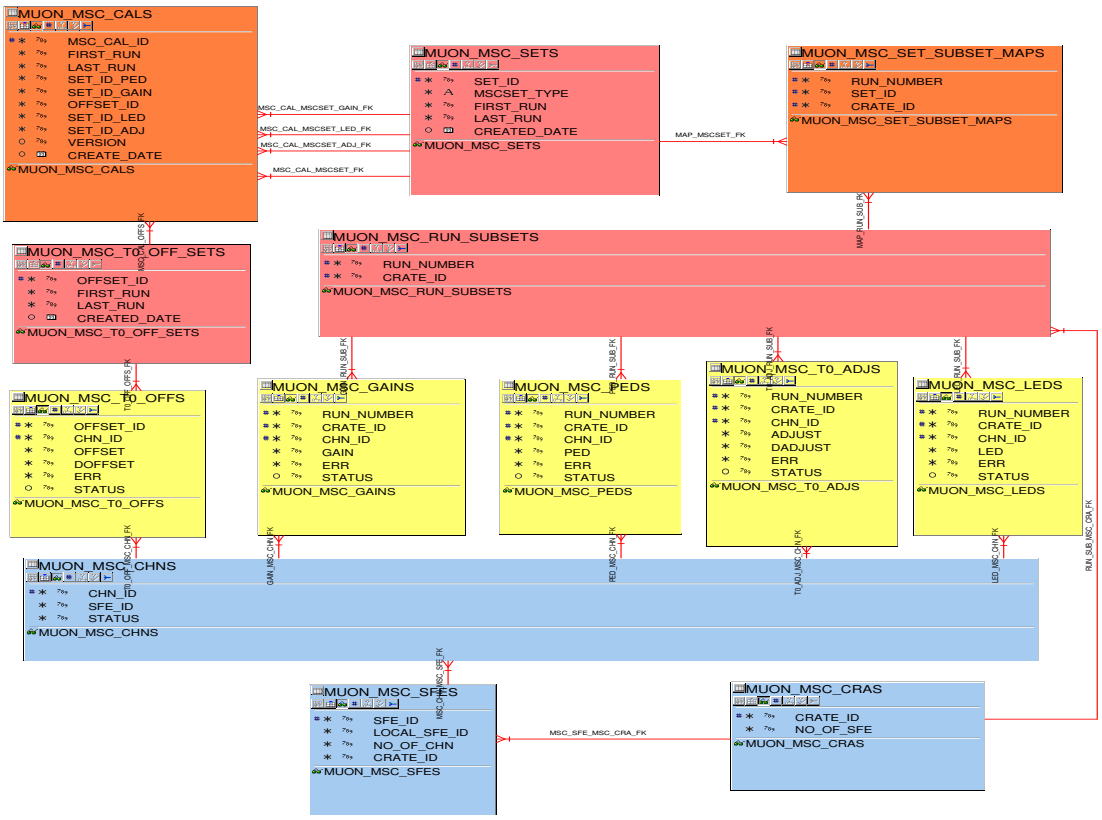

Figure D.1: MSC Offline Database Design.

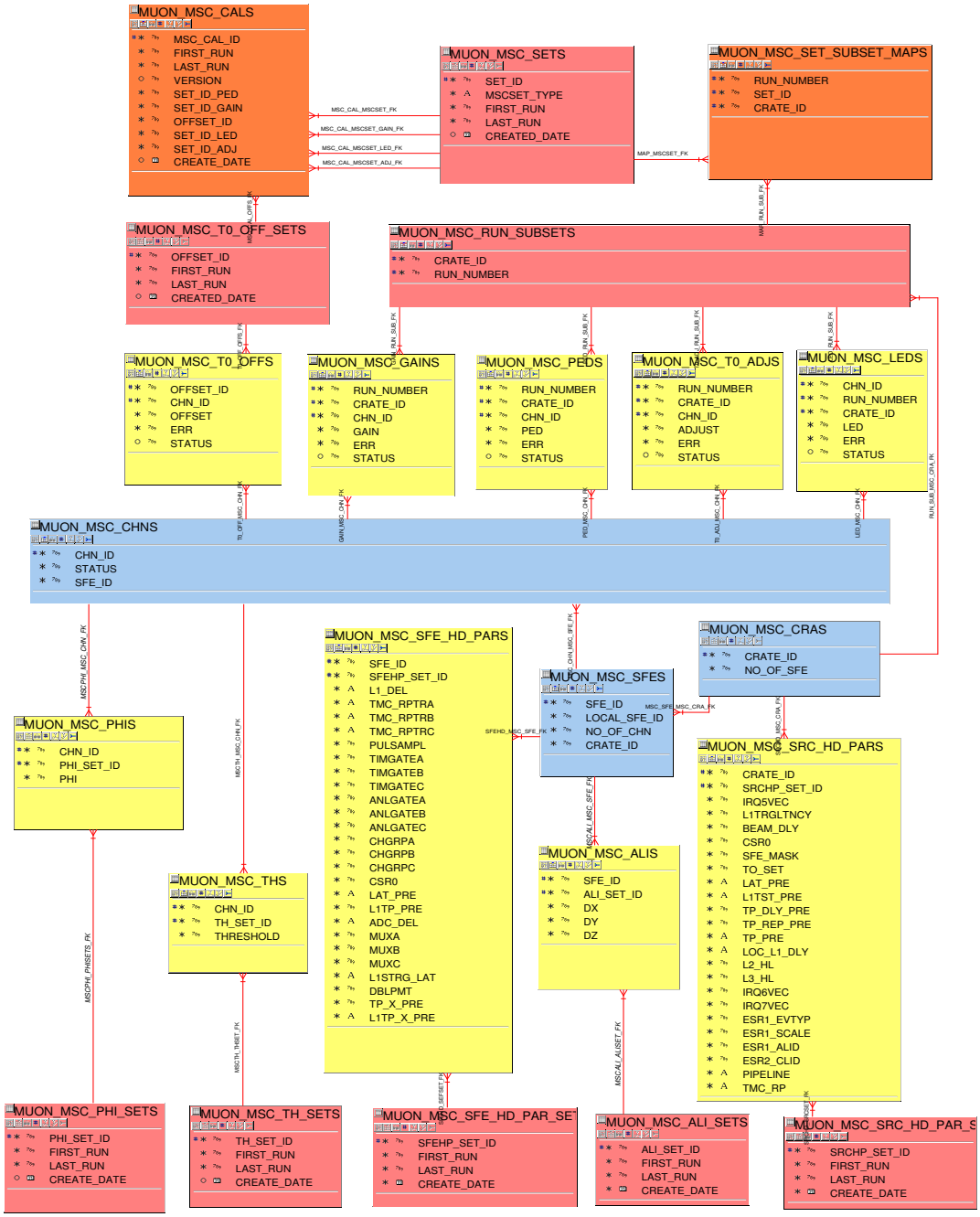

Figure D.2: MSC Online Database Design.

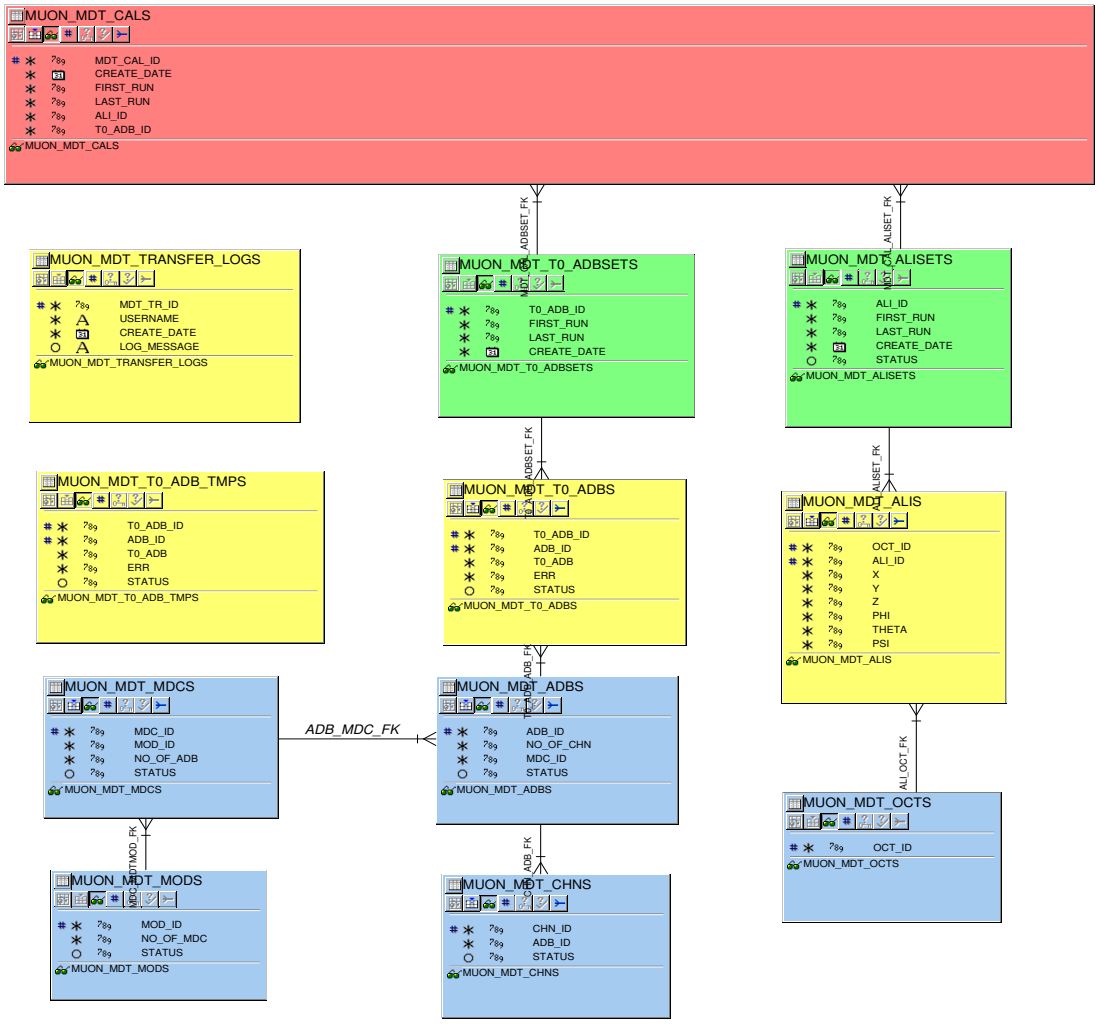

Figure D.3: MDT Offline Database Design.

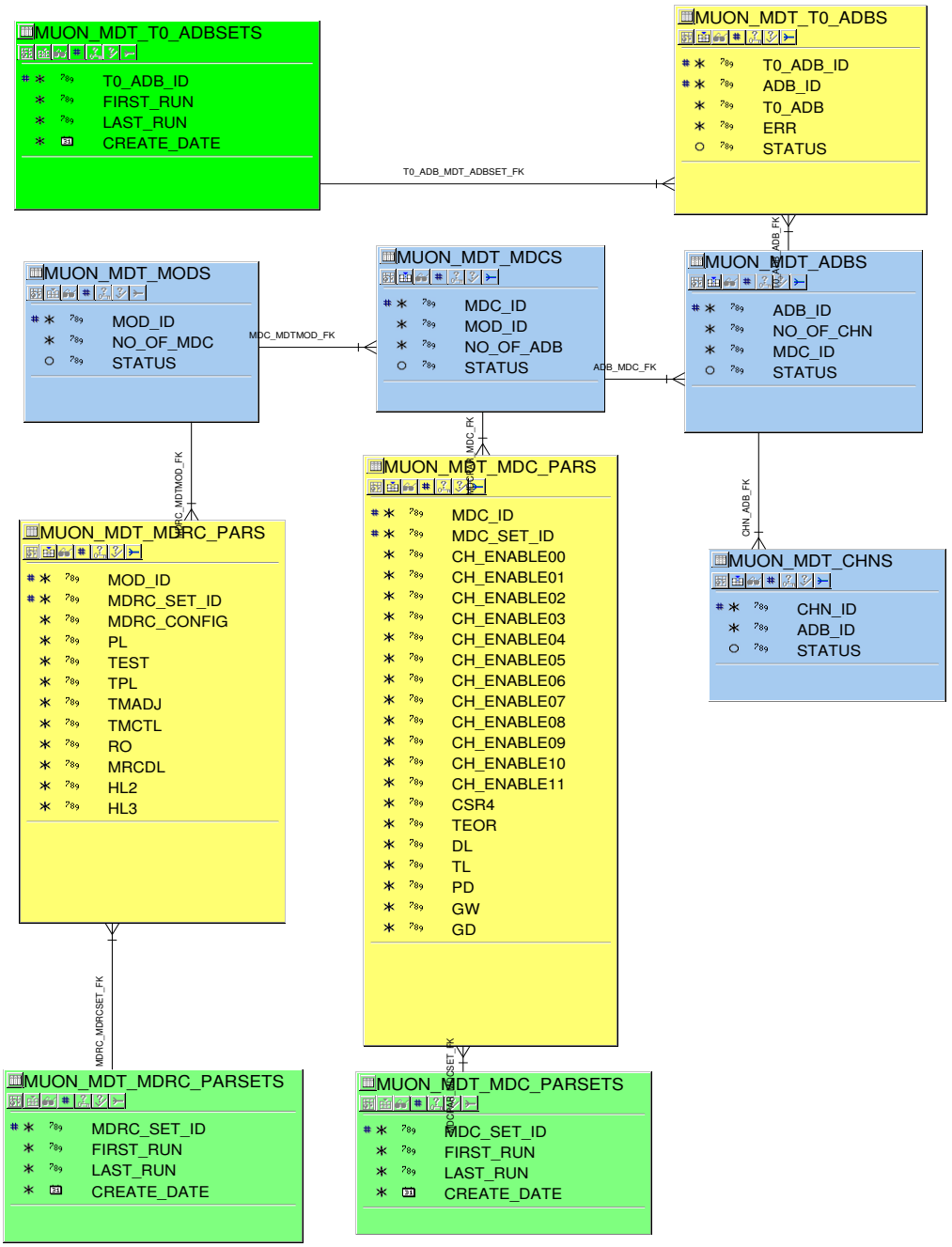

Figure D.4: MDT Online Database Design

References

[1] Donald H. Perkins, *Introduction to High Energy Physics (4th edition),* Cambridge University Press 2000.

[2] Particle Data Group, S. Eidelman *et al.*, Phys. Lett. B**592**, 1 (2004).

[3] W. Marciano and H. Pagels, Phys. Rep. C**36**, 137 (1954).

[4] P. W. Higgs, Phys. Lett. **12**, 132 (1964); Phys. Rev. Lett. **13**, 508 (1964).

[5] J. Goldstone and S. Weinberg, Phys. Rev. **127**, 965 (1962).

[6] CDF Collaboration, F. Abe *et al.*, Phys. Rev. Lett. **69**, 3704 (1992); **79**, 572 (1997); **79**, 578 (1997).

[7] R. Baier, R. Ruckl, Z. Phys., C**19**, 251 (1983);
M. Vanttinen *et al.,* Phys. Rev. D**51**, 3332 (1995); G. Schuler CERN-TH.7170/94.

[8] H. Fritzsch Phys. Lett. **67B**, 217 (1977);
R. Gavai *et al.*, IJ of MP A**10**, 3043 (1995);
J. Amundson *et al.* Phys. Lett. B**390**, 323 (1997);
O. J. P. Eboli *et al.* Phys. Rev. D**60**, 117501 (1999);
C. B. Mariott, M. B. Ducati, G. Ingelman, hep-ph/0111379 (2001).

[9] A. Edin, G. Ingelman, J. Rathsman, Phys. Rev. D**56**, 7317 (1197).

[10] G. Bodwin, E. Braaten and G. Lepage, Phys. Rev. D**51**, 1125 (1995); Phys. Rev. D**55**, 5853 (1997);
E. Braaten and S. Fleming Phys. Rev. Lett. **74**, 3327 (1995);
M. Cacciari *et al.* Phys. Lett. B**356**, 553 (1995);
P. Cho, A. Leibovitch Phys. Rev. D**53**, 150 (1996); 6203 (1996).

[11] CDF Collaboration, B-Physics group, http://www-cdf.fnal.gov/bphysics/

[12] CDF Collaboration, Phys. Rev. Lett. **75**, 4358 (1995).

[13] CDF Collaboration, Phys. Rev. Lett. **84**, 2094 (2000).

[14] CDF Collaboration, Phys. Rev. Lett. **88**, 161802 (2002).

[15] C. Luo, Indiana University, Ph.D. dissertation, *Muon identification and B physics studies at the Tevatron Collider Experiment DØ* (2003).

[16] E. Braaten, S. Fleming, and T.C. Yuan, Annu. Rev. Nucl. Part. Sci. **46**, 197 (1996).

[17] R.Baier, R. Ruckl, Z. Phys. C**19**, 251 (1983).

[18] P. Cho, A. Leibovich, Phys. Rev. D**53** 150 (1996).

[19] E. Braaten, S. Fleming and A. K. Leibovitch, Phys. Rev. D**63**, 094006 (2001).

[20] E. Braaten, J. Lee, Phys. Rev. D**63**, 071501(R) (2001).

[21] E. L. Berger, J. Qiu and Y. Wang, hep-ph/0404158, May 2004.

[22] V.A. Khoze *et al.*, hep-ph/0410020 v1, Oct 2004.

[23] C. N. Brown *et al.*, Phys. Rev. Lett. **86**, 2529 (2001).

[24] A. Zieminski, invited talk at the Charm Workshop, Trento, June 17-22, 2002; `http://hep.physics.indiana.edu/~zieminsk/talks/trento_onia.ps`
Also invited talk in the "Proceedings of the 1999 Conference on Physics in Collision", Ann Arbor, Michigan.

[25] H. Evans, invited talk in "XXIV Physics in Collision", Boston, MA June 28, 2004.

[26] J. Thompson, *Introduction to Colliding Beams at Fermilab*, FERMILAB-TM-1909, 1994.

[27] Fermilab, *Tevatron Run II Handbook*, Internal FNAL note (unpublished).

[28] D. E. Johnson, *Instrumentation Requirements for the Fermilab Main Injector*, Internal Main Injector Note 76, 1992 (unpublished).

[29] DØ Collaboration, *DØ Upgrade: the Detector and its Physics*, Fermilab Pub-96/357-E.

[30] DØ Collaboration, *DØ Silicon Tracker Technical Design Report*, DØ Note 2169.

[31] DØ Collaboration, *DØ Upgrade: Central Fiber Tracker*, http://d0server1.fnal.gov/users/stefan/www/CFT_TDR/CFT_TDR.ps.

[32] *A Little Tour of VLPC's*, http://d0server1.fnal.gov/users/stefan/www/vlpc/index.html.

[33] *Conceptual Design of a 2 Tesla Superconducting Solenoid for the Fermilab DØ Detector Upgrade*, Fermilab TM-1886/DØ Note 2167.

[34] D. Adams *et al.*, Nucl. Phys. B**44**, 332 (1995);
IEEE Trans. Nucl. Sci., Vol. **43**, No. 3, 1146 (1996).

[35] DØ Collaboration, Nucl. Instr. Meth. A**338**, 185 (1994).

[36] *Technical Design Report for the Upgrade of the ICD for DØ Run II*, DØ Note 2686.

[37] B.Baldin *et al.*, *Technical Design of the Central Muon System*, DØ Note 3365; G. Alexeev *et al.*, *Technical Design of the Forward Muon Tracking Detector Based on Mini-Drift Tubes*, DØ Note 3366.

[38] V. Abramov *et al.*, *Forward muon system for the DØ Upgrade*, Nucl. Instr. Meth. A**419**, 660 (1998).

[39] B. S. Acharya *et al.*, *Scintillation Counters for the DØ Upgrade*, Nucl. Instr. Meth. A**401**, 45 (1997).

[40] G. Blazey, *The DØ Run II Trigger*, "10th IEEE Real-Time Comp. App. in Nuclear, Particle, and Plasma Physics", Beaune, France, Conf. Proc. (1997).

[41] W. Smart, *Alignment of the DØ detector*, DØ Note 2909.

[42] MINUIT Reference Manual (Version 94.1).

[43] G. Hesketh, private communication.

[44] J. Butler, private communication.

[45] A. Zieminski, *Muon alignment and Calibration and their implementation*, Beaune, June 17th, 2003

[46] A. Zieminski, *Local Muon Reconstruction*, Muon-ID meeting, Nov. 18th, 2003

[47] O. Bardon, D. Wood, *Muon Online and Offline Constant Specifications for Run II*, DØ Note 3497.

[48] T. Yasuda, http://d0server1.fnal.gov/projects/OfflineCalibAlign/Calibration.

[49] http://www-d0.fnal.gov/Run2Physics/ckm/.

[50] MuonID group, *MuonID Certification for p14*, DØ Note 4350.

[51] F. Paige and S. Protopopescu, Brookhaven National Laboratory Report No. 38304 (1986).

[52] T. Sjöstrand, L. Lönnblad, S. Mrenna and P. Skands, *PYTHIA 6.206*, hep-ph/0108264.

[53] G. Marchesini, B. Webber, G. Abbiendi, I. Knowels, M. Seymour, Computer Physics Communications **67**, 465 (1992).

[54] http://www-d0.fnal.gov/d0dist/dist/packages/cardfiles.

[55] http://www-d0.fnal.gov/d0dist/dist/releases/test/d0gstar/docs/html /d0gstar.html.

[56] http://www-d0.fnal.gov/computing/MonteCarlo/simulation/d0sim.html.

[57] F. Carminati sl et al., *GEANT Users Guide*, CERN Program Library, 1991.

[58] http://www-clued0.fnal.gov/runjob.

[59] http://hep.physics.indiana.edu/ juhuang/b-physics/bphysics.html.

[60] http://hep.physics.indiana.edu/ zieminsk/results/trkeff.

[61] E. Nurse, *Measurement of cross section times branching ratio for* $Z \rightarrow mu^{+}mu^{-}$ *in ppbar collisions at 1.96 TeV*, DØ Note 4284.

[62] E. Varnes, *Track reconstruction efficiency measurement with single muons*, DØ Note 4317.

[63] Rob McCroskey, http://www-clued0.fnal.gov/ robmcc/simulator/single-muon-p14.html

[64] DØ top group internal status report, March 2004.

[65] CDF Collaboration, F. Abe *et al.*, Phys. Rev. D**65**, 052005 (2002).

[66] DØ Collaboration, S.Abachi *et al.*, Phys. Lett. B**370**, 239 (1996); Phys. Rev. Lett. **82**, 35 (1999).

[67] E. L. Berger, J. Qiu and Y. Wang, in preparation for submission to the DPF proceedings, Oct. 2004.

Curriculum [redacted]

Personal

Name: Jundong Huang

[redacted]

Education

1999-2004	**Ph.D.**, Indiana University, Bloomington, IN
1994-1997	**M.Sc.** Institute of High Energy Physics, Beijing, China
1988-1992	**B.Sc.** Peking University, Beijing, China

Research Experience

FNAL DØ	Studies of $\Upsilon(1S)$ bottomonium state production
BEPC BES	The upgrade and cosmic ray test of MDC detector

Work Experience

1999-2004	Research Assistant
	Department of Physics, Indiana University
1992-1994	Research Associate
	China Institute for Radiation Protection
	Taiyuan, China